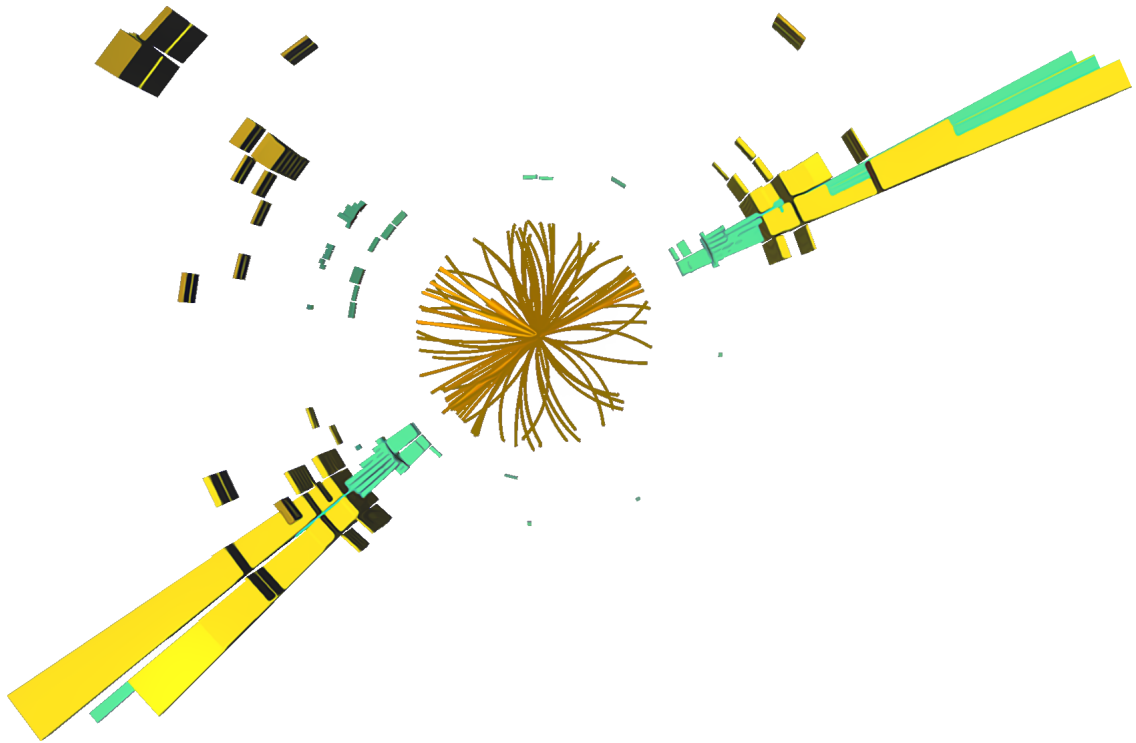


TRACK RECONSTRUCTION IN DENSE ENVIRONMENTS AND THE
SEARCH FOR NEW PHYSICS IN THE FULLY HADRONIC DIBOSON
CHANNELS WITH THE ATLAS DETECTOR



Dissertation

ROLAND JANSKY

November 2016

Faculty for Mathematics, Computer Science and Physics
University of Innsbruck

Roland Jansky:

Track reconstruction in dense environments and the search for new physics in the fully hadronic diboson channels with the ATLAS detector,

November 2016

SUPERVISORS:

Emmerich Kneringer

Andreas Salzburger

ABSTRACT

With the increase in center-of-mass energy of the LHC to $\sqrt{s} = 13$ TeV for Run 2, events with dense environments are produced much more abundantly. In the core of highly energetic hadronic jets, the average separation of charged particles is comparable to the size of individual ATLAS inner detector elements. These dense environments may be produced by new physics processes or objects, including massive particles that decay to highly boosted bosons. However, this density can create confusion within the algorithms reconstructing charged particle trajectories (tracks), so careful optimization must be carried out to ensure that the track reconstruction performance in dense environments is not adversely affected. Such optimization will increase the possibility of discovery of new phenomena and allow higher precision measurements of the newly opened kinematic regime.

This work describes a series of improvements to the ATLAS offline track reconstruction to enhance its performance in dense environments. The effects of these improvements are demonstrated using both Monte Carlo simulation and data. Using data alone, residual inefficiencies of the track reconstruction in the core of jets are quantified as a function of the transverse momentum of the jet. The fraction of lost tracks is presented using the energy loss in silicon. It varies from $0.061 \pm 0.006(\text{stat.}) \pm 0.014(\text{syst.})$ to $0.093 \pm 0.017(\text{stat.}) \pm 0.021(\text{syst.})$ between a transverse jet momentum of 200 to 400 GeV and 1400 to 1600 GeV, respectively.

With this improved track reconstruction performance, and vastly smaller uncertainties through the data-driven measurement of the track reconstruction inefficiency, ways to reconstruct the masses of jets with higher precision become possible. It is demonstrated that combining the strengths of both the calorimeter and the tracker into a combined jet mass provides the most performant method currently available in ATLAS, reducing both the resolution of the reconstructed mass of the jet and its uncertainty.

Employing these novel reconstruction methods, a search for resonances with masses in the range $1.2 < m < 3.5$ TeV in the hadronically decaying WZ , WW , or ZZ final state, is performed in 15.5 fb^{-1} of $\sqrt{s} = 13$ TeV proton-proton collision data. No significant deviations from the background expectations are observed. An additional charged or neutral heavy vector boson, as predicted by the Heavy Vector Triplet phenomenological Lagrangian (assuming $g_V = 1$), decaying through $W' \rightarrow WZ$ (or $Z' \rightarrow WW$), is excluded in the mass range 1.2–2.0 (1.2–1.7) TeV at the 95% confidence level.

ZUSAMMENFASSUNG

Mit dem Anstieg der Kollisionsenergie des LHC auf 13 TeV in Run 2 werden Ereignisse mit hohen Teilchendichten um ein Vielfaches häufiger. Im Zentrum hochenergetischer hadronischer Jets ist die durchschnittliche Entfernung zwischen geladenen Teilchen vergleichbar mit den Dimensionen der einzelnen Sensoren des ATLAS Inner Detector. Diese hohen Teilchendichten werden häufig durch Signaturen möglicher neuer Physik erzeugt, zum Beispiel massive Teilchen welche in stark geboostete Bosonen zerfallen. Diese hohe Dichte kann jedoch zu Problemen in der Spurenrekonstruktion geladener Teilchen führen. Diese Probleme können durch gezielte Veränderungen der Spurenrekonstruktion umgangen und deren Leistung verbessert werden. Solche Verbesserungen erhöhen sowohl die Chance neue Phänomene zu entdecken, als auch schaffen sie die Grundlage für detaillierte Messungen des neu erschlossenen kinematischen Regimes.

Optimierungen der ATLAS Offline-Spurenrekonstruktion werden in dieser Arbeit erläutert und die daraus resultierende, verbesserte Leistung anhand von sowohl Monte-Carlo Simulation als auch von Daten präsentiert. Mit einer vollständig datenbasierte Methode wird jegliche verbleibende Ineffizienz der Spurenrekonstruktion im Zentrum von Jets als eine Funktion des Transversal-Impulses der Jets bestimmt. Der Bruchteil der Spuren welche einen Pixel-Cluster in der zweiten Pixel-Lage, erzeugt von zwei Teilchen, enthalten sollte und die bei der Rekonstruktion verloren gehen, wird mit Hilfe des Energieverlustes der Teilchen im Silizium bestimmt. Er variiert zwischen $0.061 \pm 0.006(\text{stat.}) \pm 0.014(\text{syst.})$ bei einem transversalen Impuls im Bereich von 200 bis 400 GeV und $0.093 \pm 0.017(\text{stat.}) \pm 0.021(\text{syst.})$ bei einem transversalen Impuls zwischen 1400 bis 1600 GeV.

Durch die verbesserte Leistung der Spurenrekonstruktion und die damit verbundenen erheblich reduzierten Unsicherheiten, durch die beschriebene datenbasierte Messung der Ineffizienz, werden neue Methoden zur Bestimmung der Masse eines Jets möglich. Es wird gezeigt, dass eine Kombination der Stärken von Kalorimeter und Tracker zu der derzeit leistungsfähigsten Methode zur Bestimmung der Jet-Masse in ATLAS führt.

Mit diesen neuartigen Rekonstruktionsmethoden wird in 15.5 fb^{-1} an $\sqrt{s} = 13 \text{ TeV}$ Proton-Proton Kollisionsdaten nach Resonanzen mit Massen im Bereich von $1.2 < m < 3.5 \text{ TeV}$ gesucht, welche in WW , WZ oder ZZ Bosonen-Paare zerfallen, die als geboostete Boson-Jets rekonstruiert werden. Es wird kein signifikanter Überschuss an Ereignissen über dem zu erwartenden Untergrund Zählraten beobachtet. Zusätzliche Vektorbosonen W' (Z') mit einem Zerfall zu WZ (WW), vorhergesagt durch ein Modell des phänomenologischen Lagrangian des Heavy Vector Triplet, werden im Massenbereich zwischen 1.2–2.0 (1.2–1.7) TeV mit einer statistischen Sicherheit von 95% ausgeschlossen.

ACKNOWLEDGMENTS

First, I would like to express my sincerest gratitude to Emmerich Kneringer. Without him, I would have never entered the field of high energy physics and without his unconditional support this thesis would not exist. Dietmar Kuhn deserves a special mention for being the soul of the Innsbruck ATLAS group and allowing me to flourish within it.

Andreas Salzburger and Markus Elsing provided the best guidance possible, provided expert technical advice, while all the same giving me the free space I needed. Especially, I want to thank them for pushing me in order for this work to reach its full potential.

Anthony Morley and Gabriel Facini deserve my greatest gratitude. Both are shining examples of not just brilliant physicists, but also fantastic colleagues. Anthony endured an innumerable amount of questions over the years, but still keeps providing both the most critical and useful answers imaginable. Gabriel enabled me to see the big picture in today's particle physics. His passion and positivity are an inexhaustible source of motivation. Many more colleagues will remain unnamed, but I want to thank the whole TIDE group, which I was very proud to work in and convene.

Let me thank Heather Gray, for always having advice when needed. James Catmore, apart from being a great friend, his unrivaled knowledge of the English language profited this thesis immensely. Yanyan Gao, has my deepest appreciation for welcoming me into her analysis team and putting up with my occasionally effervescent nature.

My family, including Alexandra Feistmantl, can not be thanked enough. Thank you.

CONTENTS

1	INTRODUCTION	1
I	THEORY & ATLAS EXPERIMENT	3
2	THEORY	5
2.1	The Standard Model of Particle Physics	5
3	THE LHC AND THE ATLAS EXPERIMENT	7
3.1	Large Hadron Collider at CERN	7
3.2	Coordinate System	8
3.3	The Magnet System	8
3.4	The Inner Detector	9
3.5	The Calorimeter	12
3.6	The Muon Spectrometer	13
3.7	The Trigger System	13
3.8	The ATLAS Computing Network	13
3.9	The ATLAS Offline Software - Athena	13
II	TRACK RECONSTRUCTION IN DENSE ENVIRONMENTS	15
4	TRACK RECONSTRUCTION	17
4.1	Pixel and SCT Clusterization	17
4.2	Iterative Combinatorial Track Finding	17
4.3	Track Candidates and Ambiguity Solving	18
4.4	Truth-Based Reconstruction	20
4.5	Truth-Based Track Quality	20
5	ALGORITHMIC IMPROVEMENTS TO THE TRACK RECONSTRUCTION	21
5.1	Samples	21
5.2	Merged Clusters on Reconstructed Tracks	21
5.3	Limitations on Shared Clusters	26
6	RUN 2 PERFORMANCE AND STUDIES WITH THE ITK LAYOUT	31
6.1	Jet Reconstruction	31
6.2	Track Reconstruction Performance in the Core of Jets	32
6.3	Implications for Flavor Tagging	34
6.4	Performance of Track Reconstruction in Dense Environments with the ITk	36
6.5	Conclusion	36
III	MEASURING TRACK RECONSTRUCTION PERFORMANCE IN DATA	41
7	PROPERTIES OF RECONSTRUCTED TRACKS IN DENSE ENVIRONMENTS IN RUN 2 DATA	43
8	MEASURING THE PERFORMANCE OF THE PIXEL CLUSTER NEURAL NET- WORK IN DATA	47
8.1	Methods	47
8.2	Results	51

8.3	Conclusion	55
9	MEASURING TRACK LOSS IN DENSE ENVIRONMENTS WITH THE DE/DX METHOD	57
9.1	Method	57
9.2	Systematic Uncertainties	61
9.3	Results	63
IV	JET MASS RECONSTRUCTION	67
10	JET MASS RECONSTRUCTION	69
10.1	Jet Mass Definitions	69
10.2	Jet Mass Calibration	71
10.3	Jet Mass Performance in Simulation	73
10.4	Jet Mass Systematic Uncertainties	75
10.5	Combination of m^{TA} and m^{calo}	76
10.6	Conclusion	77
V	SEARCH FOR RESONANCES WITH BOSON-TAGGED JETS	79
11	SEARCH FOR RESONANCES WITH BOSON-TAGGED JETS	81
11.1	Data Sample and Simulated Samples	82
11.2	Preselection	84
11.3	Event Selection	85
11.4	Control Regions	95
11.5	Background Parametrization	98
11.6	Systematic Uncertainties	101
11.7	Results	102
12	CONCLUSION	107
	BIBLIOGRAPHY	109

INTRODUCTION

The Large Hadron Collider (LHC) entered a new energy regime at Run 2 with proton-proton collisions at $\sqrt{s} = 13$ TeV¹. Events with multi-TeV jets showering in the detectors, or tau-leptons and b -hadrons surviving passage through multiple active layers of material, are now common place. These objects are also signatures for new physics, including massive particles that decay to highly boosted bosons, whose own subsequent decay products are often reconstructed into one large-radius jet.

In the core of highly energetic hadronic jets, the average separation of charged particles is comparable to the size of individual inner detector (ID) elements. This can create confusion within the algorithms reconstructing charged particle trajectories (tracks). Without careful consideration, the track reconstruction efficiency in these dense environments will be limited, resulting in difficulties in identifying long-lived b -hadrons and hadronic tau lepton decays, or in the calibration of energy and jet mass measurements. Mitigating such losses will increase the possibility of discovery of new phenomena and allow more detailed measurements of the newly opened kinematic regime. A dedicated optimization for dense environments was deployed in the ATLAS reconstruction for the start of Run 2.

This thesis is structured in five major parts, where Part I introduces the Standard Model of Particle Physics, the LHC and the ATLAS experiment.

Part II gives a general overview of the track reconstruction algorithms describing the performance of charged particle reconstruction in dense environments by the ATLAS detector at the start of Run 2. Crucial components for dense environments are noted. The quality of the expected performance is demonstrated in dedicated simulated samples of single particles and dijet events, and comparisons between simulation and data are performed in energetic jet events. Extending these Monte Carlo (MC) based studies, methods are introduced in Part III to probe the performance in data. One of these measures the inefficiency of the reconstruction in high p_T jets, an environment of high charged particle multiplicity and collimation, by using the ionization energy loss (dE/dx) in the pixel detector.

Part IV explains how the mass of jets is reconstructed. It especially focuses on recent developments extending the classical concept of a calorimeter-based mass to use information from the tracker - a concept which becomes feasible due to the improvements in performance and uncertainties described in Part II. High jet mass resolution as well as small related uncertainties are crucial for a plethora of physics analyses. Since the mass can be used to identify jets originating from bosons, it is especially relevant for the last part of the thesis.

Finally, a search for narrow resonances decaying hadronically into boosted boson pairs is presented in Part V, exploiting the previously described developments in the ATLAS track reconstruction as well as the novel jet mass definitions.

¹ As common in particle physics, this thesis adopts “natural units” where the reduced Planck constant, the speed of light in vacuum and the Boltzmann constant are set to unity ($\hbar = c = k_B = 1$) and the unit of energy is electron-volts ($1 \text{ eV} = 1.6 \times 10^{-19} \text{ J}$).

Part I

THEORY & ATLAS EXPERIMENT

Throughout the history of science, individuals studying nature systematically have tried to describe it with mathematical models. The strength of such models lies not just in describing the observed, but also in their ability to predict as yet unseen phenomena. In the study of fundamental particles, all objects and phenomena observed thus far can be described by the Standard Model of Particle Physics (SM). With an accuracy that exceeds all current experimental limits, it is able to describe three of the four fundamental interactions of nature: electromagnetism, the weak nuclear force and the strong force. Using the formalism of Quantum Field Theory, the SM combines aspects of quantum mechanics, classical field theory and Special Relativity. It fails to incorporate the fourth known force: gravity. The gravitational force is best described by Einstein's Theory of General Relativity [1]. Although it is the weakest of all fundamental forces, it dominates on large scales, where it is able to describe the properties of time and space by linking gravitation to the geometry of the Universe. Unifying all four forces into one theory is the greatest challenge for fundamental physics. Section 2.1 will briefly introduce the SM, while possible theories beyond it are saved for Chapter V, where they are mentioned in the scope of a search for new physics. A more thorough description of the SM can be found in Reference [2].

2.1 THE STANDARD MODEL OF PARTICLE PHYSICS

The SM introduces point-like particles with half-integer spin (fermions) whose interactions are mediated by integer spin particles (gauge bosons). These fermions include three leptons with electric charge $Q = -1e$, the electron (e), muon (μ) and tau (τ), and corresponding neutral particles called neutrinos. They are complemented by the up-, down-, charm-, strange-, top- and bottom-quark with electric charge $Q = +\frac{2}{3}e$ or $Q = -\frac{1}{3}e$. For each of these particles, a corresponding anti-particle with inverted charges exists. They are organized into three generations of up- and down-type quarks, and of neutral and charged leptons, with massive particles in each generation being heavier than those in the previous generation. Each quark can exist in three different states of a quantum property called color charge, as first proposed by Gell-Mann [3]. It is not known why the fundamental fermions are arranged into generations in this way, nor whether additional generations of still heavier particles exist.

By unifying quantum electrodynamics (QED) and the theory of weak interactions first proposed by Glashow, Weinberg and Salam [4–6], the SM is able to describe interactions through the electromagnetic and weak nuclear force in one, electroweak, theory. Quantum chromodynamics (QCD) is used to describe the strong force. One of the key concepts of all theories of the SM are local gauge symmetries. For example, the assumption that the the electron field is invariant under local gauge transformations leads to a new massless spin 1 gauge field, which materializes as the photon. Similarly, the gluons are introduced in the strong interaction and the weak bosons (W^+ , W^- ,

Z) in the electroweak interaction. These gauge theories can be summarized with the $U(1) \times SU(2) \times SU(3)$ group. The non-abelian nature of the $SU(2)$ and $SU(3)$ symmetry groups leads to the important effect of self-coupling of the respective bosons, for example two oppositely charged W bosons can couple to a photon or a Z boson.

There is one major problem with this formalism: any mass term in the theory would violate the chiral symmetry of the $SU(2)$ group. By introducing the concept of spontaneously symmetry breaking, Brout, Englert and Higgs [7, 8], were able to resolve this issue by introducing an additional scalar field doublet. The so called Higgs mechanism allows for massive leptons and weak bosons while retaining a massless photon. In addition, it predicts a massive excitation of the field, a Higgs boson, whose only free parameter is its mass. Both the weak bosons and the Higgs boson were experimentally confirmed at CERN by the UA1 and UA2 experiments in 1983 [9, 10] and the ATLAS and CMS experiments in 2012 [11, 12]. Figure 1 gives an overview of all the constituents of the SM and their masses.

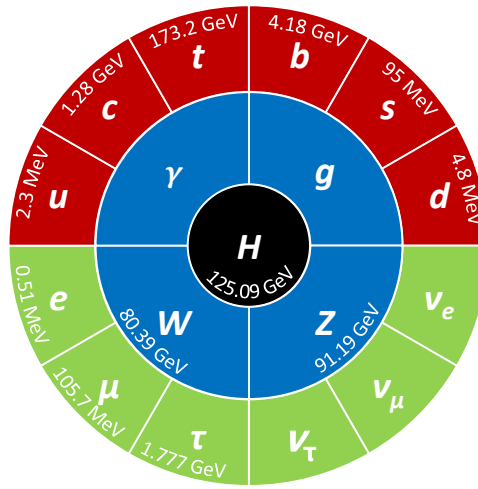


Figure 1: Elementary particles of the Standard Model and their experimentally measured masses. The photon (γ), the gluon (g) and the neutrinos (ν) are assumed to be massless. The outer ring consists of the fermionic particles, quarks in red and leptons in green. For each fermion a corresponding anti-particle exists. Gauge bosons, the mediators of the fundamental forces described by the Standard Model, are in the blue ring. In the center is the Higgs boson, which gives rise to mass of the weak bosons.

The ATLAS experiment [13] is a project with more than 20 years of history (the Letter of Intent was written in 1992). The detector itself is enormous, being 44 metres wide, 22 metres in height and weighting 7000 tonnes. It is a multipurpose particle detector, designed to probe the forefront of Particle Physics, and is situated at the LHC [14] along with three other big experiments. CMS is another multipurpose detector and like ATLAS it is able to measure, reconstruct and identify leptons, photons, quark jets, individual charged particles and primary and secondary vertices. ALICE and LHCb are designed for more specific purposes, which are recording events from heavy ion collisions and detecting signatures from heavy flavor decays respectively. The main components of the ATLAS detector are described in the following and can be seen in Figure 2.

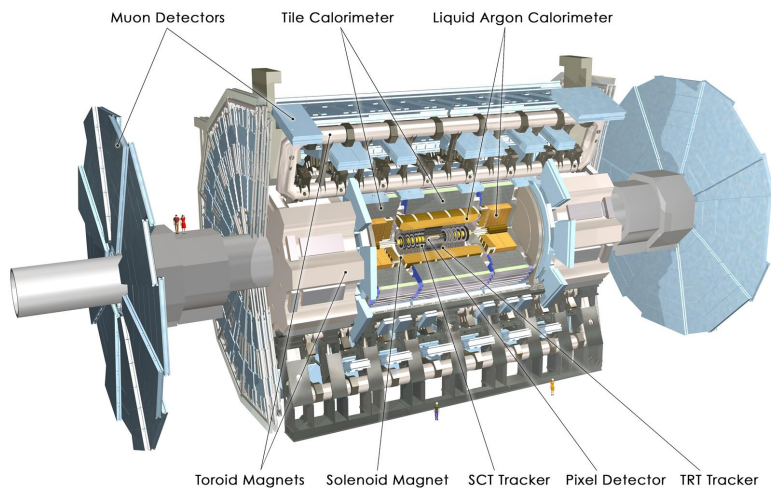


Figure 2: A schematic drawing of the ATLAS detector. [13]

3.1 LARGE HADRON COLLIDER AT CERN

The LHC is a superconducting proton accelerator and collider installed in a 27 kilometers circumference underground tunnel at CERN. The 4-meter-wide tunnel was built for the Large Electron Positron (LEP) collider in 1985. The first studies for a high-energy proton-proton collider in the LEP tunnel started in 1984. LEP2 was closed in 2000, and installation of LHC machine and experiments started in 2003. The first collisions at $\sqrt{s} = 900$ (center-of-mass frame energy) GeV were recorded on November 23, 2009. The first collisions at $\sqrt{s} = 7$ TeV took place on March 30, 2010, starting a long physics program. First collisions at $\sqrt{s} = 8$ TeV were recorded on May 1st, 2012, and the machine performed spectacularly, delivering quickly increasing luminosities [15]. On July 4th, 2012 the discovery of a Higgs-like boson was announced by

the ATLAS and CMS collaborations. In 2015 the collision energy was further increased to $\sqrt{s} = 13$ TeV and in 2016 the LHC surpassed its design luminosity reaching values of $1.37 \times 10^{34} \text{ cm}^{-2}\text{s}^{-1}$.

3.2 COORDINATE SYSTEM

The coordinate system and nomenclature used in the ATLAS experiment are briefly summarized here, since they are used repeatedly throughout this thesis. The nominal interaction point is defined as the origin of the coordinate system, while the beam direction defines the z -axis and the x - y plane is transverse to the beam direction. The positive x -axis is defined as pointing from the interaction point to the center of the LHC ring and the positive y -axis is defined as pointing upwards. The azimuthal angle ϕ is measured around the beam axis, and the polar angle θ is the angle from the beam axis. The pseudorapidity is defined as $\eta = -\ln(\tan(\theta/2))$. In the case of massive objects such as jets, the rapidity

$$y = 0.5 \ln[(E + p_z)/(E - p_z)] \quad (1)$$

is sometimes used. The transverse momentum p_T , the transverse energy E_T , and the missing transverse energy E_T^{miss} are defined in the x - y plane unless stated otherwise. The distance ΔR in the pseudorapidity-azimuthal angle space is defined as $\Delta R = \sqrt{\Delta\eta^2 + \Delta\phi^2}$ [13].

3.3 THE MAGNET SYSTEM

The ATLAS magnet system is an arrangement of a central solenoid providing the magnetic field for the ID, surrounded by three air-core toroid magnets which generate the magnetic field for the muon system. The generated field strength is 3.9 and 4.1 T for the barrel and the end-cap toroids respectively. Each of the toroids consists of eight coils which are aligned radially symmetric around the beampipe. This system, shown in Figure 3, has been one of the biggest engineering challenges of the ATLAS experiment due to its unusual layout and large size. The design is motivated by the goal to measure the muon momentum with an accuracy of 10% at 1 TeV.

The axial symmetric magnetic field of the solenoid has a strength of 2 T. It has been designed to have as little density as mechanically possible, because any material degrades the performance of the calorimeters. This resulted in the housing of both calorimeter systems in the same vacuum vessel. The hadronic calorimeter and its support structure also serve as the return yoke of the enclosed solenoid.

The resolution of particles reconstructed by the ID is directly dependent on the strength of the magnetic field B in Tesla, since the reconstructed momentum p in units of GeV is related to the radius of track curvature ρ in meters by

$$p = 0.299792458 \cdot B\rho. \quad (2)$$

As a consequence, the resolution of particles reconstructed in the ID increases at higher η due to the lower magnetic field provided by the solenoid in that phase space.

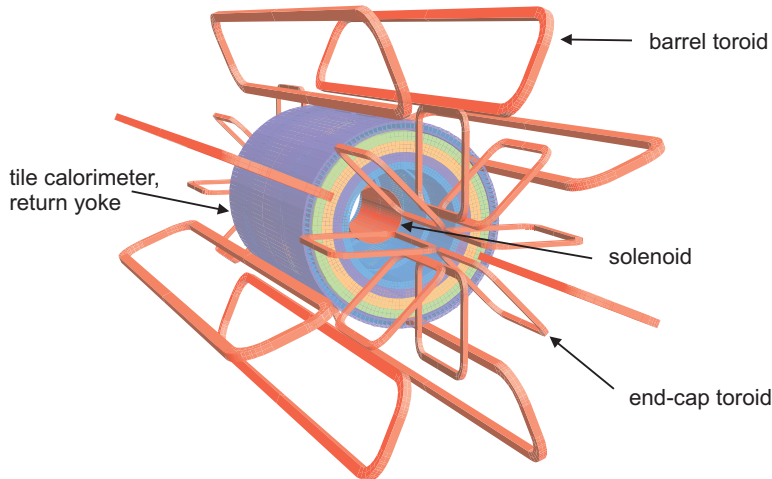


Figure 3: A schematic sketch of the ATLAS Magnet System which shows all four magnets systems as well as the tile calorimeter which acts as the return yoke of the solenoid. [13]

3.4 THE INNER DETECTOR

The ATLAS ID [16] acts as a precise tracking and vertexing device. High precision measurements with fine granularity sensors are required to make this possible within the high track density environment of LHC collisions. These are realized in the silicon pixel detector (including the recently added insertable B-layer or IBL) and silicon strip detector (SCT), for which the detector elements closest to the beamline are only about three centimeters from the interaction point. As a result of this setup each track crosses at least four pixel and four silicon strip layers. On average there are 37 measurements per track, the majority of which are provided by the transition radiation tracker (TRT). The TRT enables tracks to be reconstructed out to large radii, although with a more limited resolution. This limitation is countervailed by the large number of measurements as well as the large-radius, which still makes these measurements an important addition to the momentum measurement. The TRT is also used for particle identification and e/π separation with the help of the photons from transition radiation created in its straw tubes.

The ID itself is 6.2 meter long and has a radius of 1.2 meter. It resembles the onion-like structure of classical collision experiments. In the end-caps the same components are present as described above (see Figure 4). The momentum resolution of reconstructed tracks is proportional to $\sigma/p_T \sim 3.8 \times 10^{-4} p_T(\text{GeV}) \oplus 0.015$ [13].

3.4.1 The Pixel Detector

The pixel detector's sensors are designed to provide a high-precision measurement as close as possible to the interaction point, in a pseudorapidity range of $|\eta| < 2.5$. For Run 2 of the LHC this capability was further enhanced by the addition of the IBL, which moves the first measurement from a radius of roughly 5 centimeters to 3 centimeters. The former first pixel layer is still referred to as B-layer. The pixel detectors

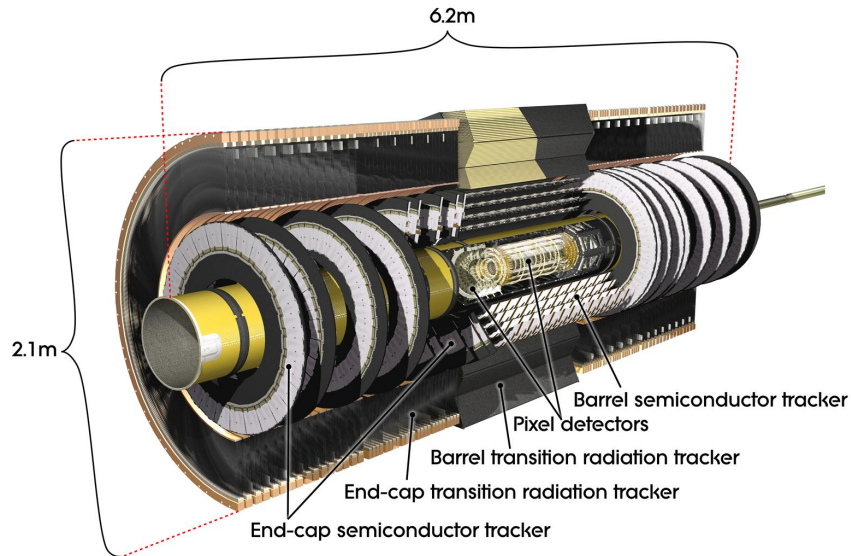


Figure 4: A cut-out view of the ATLAS inner detector. [13]

measurements determine the possible resolution of the impact parameters, a quantity which is crucial for finding short lived particles such as b -mesons and τ -leptons. The two dimensional readout has certain disadvantages. It requires the readout chips to be of large area, with individual circuits for each pixel element. The proximity to the interaction point comes at the cost of a very high radiation dose (around 158 kGy/year) compared to the other sub-detectors. The SCT only receives around 8 kGy/year. The whole system consists of 86 million detector elements with a size of 50 micrometers \times 400 micrometers for the original pixel layers and 50 micrometers \times 250 micrometers for the IBL which provide an intrinsic resolution of 10 micrometers in R - ϕ and 100 micrometers (50 micrometers for IBL) in z . A small number of pixels on each sensor are longer (500 micrometers for the IBL and 600 micrometers for the outer layers) to cover the gap between readout chips. The thickness of the original modules is 250 micrometers and 200 micrometers for the IBL. As the number of readout channels per module is not sufficient to read out every single pixel, as a compromise the last eight pixel rows are only connected to four readout channels which leads to an ambiguity in 5% of the hits, which can be resolved offline. These pixels are called *ganged*. In addition to the four barrel layers at distances of 3.33, 5.05, 8.85 and 12.25 centimeters from the detector's center, there are three disks on each side - at a distance of 49.5, 58.0 and 65.0 centimeters from the detector's center- completing the angular coverage. All detector elements have a readout such that the determination of the charge deposited by the traversing particles for each pixel by the so called Time-over-Threshold (ToT) method [17] is possible. All layers other than the IBL can do so with a 8-bit resolution. The IBL's readout is only realized with a 4-bit resolution.

3.4.2 The Semiconductor Tracker

The SCT was designed to contribute to the measurement of momentum, impact parameter and vertex position in the intermediate volume outside the pixel detector,

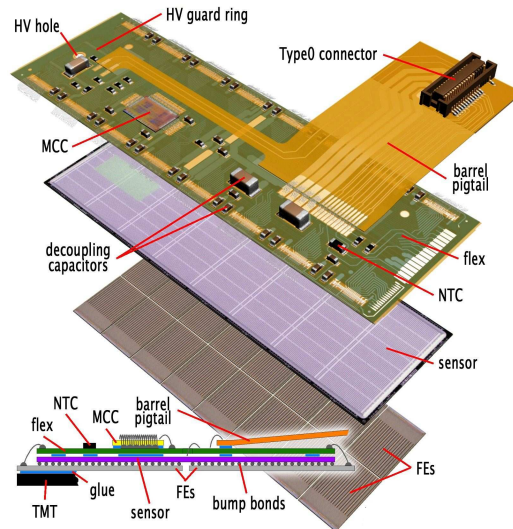


Figure 5: Schematic view of a barrel pixel module. The main components are shown, including the MCC (module-control chip), the front-end (FE) chips, the Negative Temperature Coefficient (NTC) thermistors, the high-voltage (HV) elements and the Type0 signal connector. The side view on the bottom illustrates the bump-bonding of the silicon pixel sensors to the electronics. [13]

covering a pseudorapidity range of $|\eta| < 2.5$. Compared to the pixel, the still high-granularity is also crucial for good pattern recognition. In the barrel it consists of four double-sided layers of silicon microstrip detectors at 29.9, 37.1, 44.3 and 51.4 centimeters from the detector's center. This is complemented by nine disks at a distance of 85.38, 93.40, 109.15, 129.99, 139.97, 177.14, 211.52, 250.50 and 272.02 centimeters from the detector's center. A small angle between the two sensors of each module enables measurements in the z coordinate. There is a total of 6.3 million sensors, each measuring $80 \text{ micrometer} \times 12 \text{ centimeters}$, providing an intrinsic resolution of 16 micrometers in $R-\phi$ and 580 micrometers in z . This allows tracks separated by more than approximately 200 micrometers to be resolved. The readout consists of a front-end amplifier and discriminator, followed by a binary pipeline. This binary output prohibits measuring the deposited charge in any way.

3.4.3 The Transition Radiation Tracker

The TRT consists of straw tubes with a thickness of four millimeters and covers a range in pseudorapidity up to $|\eta| < 2.1$. Only the $R-\phi$ coordinates are measured with an intrinsic accuracy of 130 micrometers per straw. Still, it contributes significantly to the momentum measurement, since the low accuracy per measurement is compensated by their abundance.. The 144 centimeters long straws are parallel to the beam axis in the barrel region, while in the end-cap region they are arranged radially in wheels. The total number of TRT readout channels is approximately 351 000. Electron identification capabilities are added by measuring the signal of transition radiation photons created in a radiator between the straws. For this reason the straws are filled with either a xenon or argon based gas mixture.

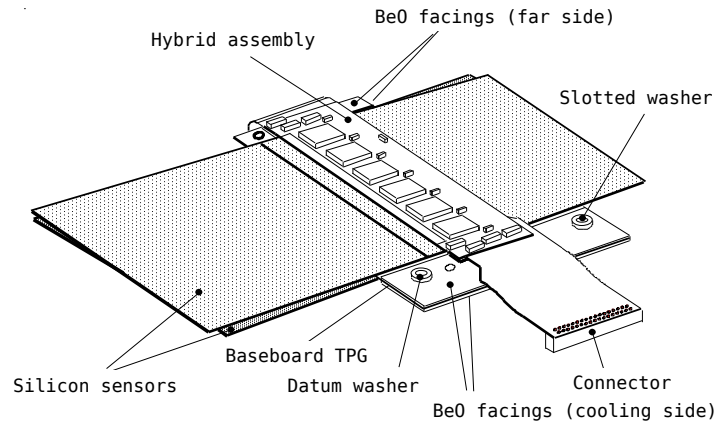


Figure 6: Drawing of a barrel SCT module, showing its components. [13]

3.5 THE CALORIMETER

The ATLAS calorimeters (see Figure 7) are located outside of the solenoid. The ATLAS electromagnetic calorimeter is based on Pb-LAr (lead-liquid argon) technology, with a novel accordion-like layout. It provides trigger, e/π identification and an energy measurement with resolution of $\sigma/E \sim 10.1\%/\sqrt{E} \oplus 0.17\%$ [13] and coverage in pseudorapidity $|\eta| < 3.2$ [15]. The forward liquid argon calorimeter provides coverage in the range $3.1 < |\eta| < 4.9$ and a resolution of $\sigma/E \sim 29\%/\sqrt{E} \oplus 0.04$. The hadronic central calorimeter is based on steel/scintillator tiles. It provides coverage up to $|\eta| < 1.7$ and a resolution of $\sigma/E \sim 50\%/\sqrt{E} \oplus 0.03$. The end-cap calorimeters use a copper/tungsten-LAr design, with coverage in pseudorapidity $1.5 < |\eta| < 3.2$ and resolution of $\sigma/E \sim 95\%/\sqrt{E} \oplus 0.08$. The total mass of the ATLAS calorimeter is about 4000 tons.

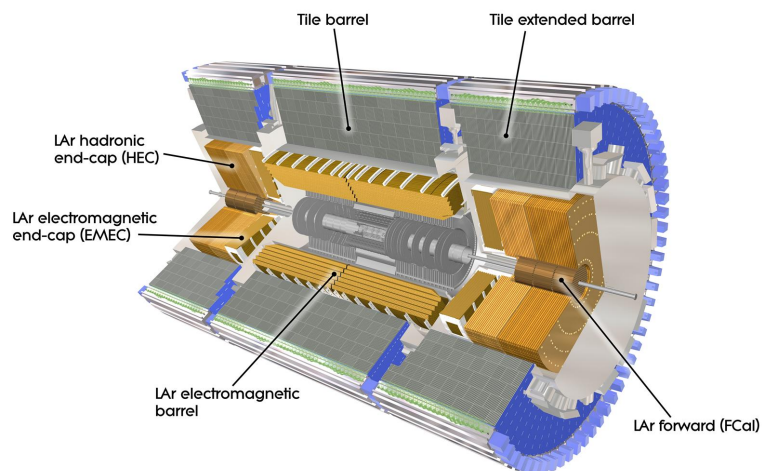


Figure 7: A cut-out view of ATLAS calorimeter detectors. [13]

3.6 THE MUON SPECTROMETER

The ATLAS muon spectrometer (see Figure 2) consists of gas-based muon chambers immersed within a toroidal magnetic field originating from air-core coils. The muons are detected with tracking chambers based on Cathode Strip (CSC) and Monitored Drift Tubes (MDT) designs with a momentum resolution $< 10\%$ up to transverse momenta of about 1 TeV. Also triggering information is provided by its thin-gap (TGC) and resistive-plate (RPC) chambers.

3.7 THE TRIGGER SYSTEM

The ATLAS trigger and data acquisition system is responsible for selecting for permanent storage and analysis ~ 1000 Events/s, out of the initial ~ 40 MHz. This two stage system is build up of the Level 1 Trigger (fast online electronics with decision times $< 2.5 \mu\text{s}$ per event [15]) and the High Level Trigger (average decision time ~ 40 ms) consisting of off-the-shelf computers and networking equipment.

3.8 THE ATLAS COMPUTING NETWORK

The ATLAS computing network is a distributed system which consists of the Tier-0 at CERN where the data is recorded onto tape and the first pass reconstruction is performed, 13 Tier-1 and 160 Tier-2 centers, which both participate in MC production and support user analysis. For further details see Reference [18].

3.9 THE ATLAS OFFLINE SOFTWARE - ATHENA

The goal of the ATLAS offline software [19] is to process the multitude of measurements from the ATLAS detector, to deliver from this processed data the physics objects to physicists, and to provide the necessary framework to analyze them in order to produce physics results. Among the many additional requirements to the software, one shall be pointed out explicitly: the need to process the collected data within the available CPU and memory resources provided to ATLAS, while at the same time meeting the physics performance requirements. As the lifetime of the ATLAS experiment is decades rather than years, its software needs to be able to adapt and evolve along with the changing physics challenges. This motivates Athena, the common offline software framework in ATLAS. It adopts an object-oriented approach and is written in the C++ language. Python is used to configure the run-time settings. The framework is built primarily from three types of software entities: algorithms, tools and services. Each algorithm is responsible for some basic task involving the input of data objects and the output of new or modified objects. Tools and services are summoned by the algorithms as needed, and the same instances may be used by multiple algorithms. Athena processes a given event by passing its constituent objects along a chain of algorithms, referred to as a sequence. Algorithms retrieve and store the data objects in a transient event store called StoreGate. At any stage in the algorithm sequence this transient data can be written to disk through a persistency service.

Part II

TRACK RECONSTRUCTION IN DENSE ENVIRONMENTS

In order to understand the importance of the track reconstruction performance in dense environments one has first to understand how charged particle reconstruction is performed, which is explained in this chapter. Chapter 5 will then provide an overview of specific improvements aimed at dense environments and Chapter 6 will demonstrate the resulting performance on MC simulated samples.

From the creation of the basic measurements in the ID known as clusters to the final high resolution track fit, the reconstruction of charged particles' trajectories, or tracks, is one of the most challenging computational and algorithmic tasks at the LHC. After the creation of three-dimensional measurements, so called *space-points*, from clusters of pixels and SCT measurements, an iterative combinatorial track finder uses these as input to create track candidates. An ambiguity solver is then used to process all track candidates and filter out those that are likely to be redundant. The outputs of this algorithm, in combination with measurements from the TRT, are the final ID tracks used for all further analyses. This chapter provides a detailed overview of the whole chain, while focusing on the most relevant parts of the algorithms for tracks in dense environments. A detailed description of aspects omitted here, such as how tracks are extended into the TRT, is given elsewhere [20].

4.1 PIXEL AND SCT CLUSTERIZATION

Single measurements on the same pixel or SCT module which share an edge or a corner are grouped together by a connected component analysis (CCA) [21]. The geometric mean position of the group is used as the initial position estimate of the intersection of the particle with the module. If the spatial separation of charged particles at the module surface reaches the dimensions of a few pixels or strips, their charge deposits start to overlap and the CCA will reconstruct a single *merged* cluster. Figure 8 illustrates this behavior.

4.2 ITERATIVE COMBINATORIAL TRACK FINDING

In order to allow for as many combinations of space-points as possible, but still achieve a rough momentum estimate, track seeds are built from three space-points. Seeds can be built from space-points from either the pixel or SCT detector, or from combinations of space-points from both detectors. This allows exactly four types of seeds with varying purities. The purity is the fraction of seeds which in the end produce a good quality track, and it is highest for seeds only formed from SCT space-points, followed by seeds formed only from pixel space-points. To maximize the efficiency of the track finding, seeds are processed ordered by their type. In addition, several selections are applied on the seeds in order to further maximize their purity, including requirements on the minimum momentum of the seeds and their impact parameter. The latter are calcu-

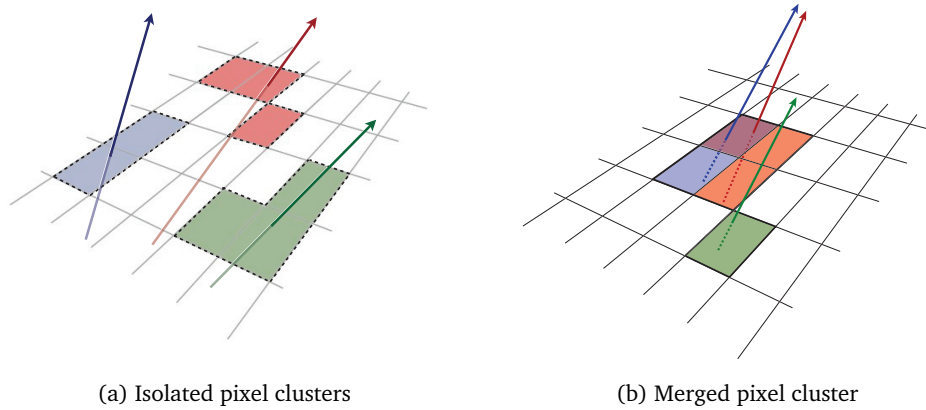


Figure 8: Illustration of (a) isolated pixel clusters on a pixel module and (b) a merged pixel clusters due to very collimated tracks. Different colors represent charge deposits from different charged particles traversing the sensor and the particles trajectories are shown as arrows.

lated assuming a perfect helical trajectory of the particle through a uniform magnetic field. Finally, seeds passing these selections are also required to have one more space-point being compatible with their extrapolated trajectory. Space-points used by a seed passing all these requirements are not considered further for other seeds, minimizing the computational complexity of the algorithm. After seed creation, a combinatorial Kalman filter [22] is used to create track candidates based on the seeds. Multiple track candidates can be built for each seed in case there are multiple possible extensions of the trajectory on a certain layer.

For a single muon about 13 combinations of space-points are created, but due to the quality requirements on the seeds, the Kalman filter is on average only called for 1.1 of them. The resulting efficiency to reconstruct a muon track is higher than 99% [23].

4.3 TRACK CANDIDATES AND AMBIGUITY SOLVING

Due to the combinatorial nature of the track finding, certain track candidates will have clusters falsely assigned to them. Therefore the concept of ambiguity solving is used: following the track candidate search, tracks are scored based on additional quality criteria and afterward compared to each other. In case of ambiguities between multiple track candidates the score decides which one to keep. Such approaches to track finding have been around since the era of LEP experiments [24].

In the ATLAS offline reconstruction, track candidates are processed one after the other in order of descending score by such an ambiguity solver. The score needs to be based on basic but robust measures of track quality, since the performance of the ambiguity solver strongly depends on it. Initially, the logarithm of the track transverse momentum and the χ^2 of the track fit are used as a base score of the track candidate. This gives preference to more energetic tracks and those with a good fit quality. At the same time, badly reconstructed tracks, which often have rather low transverse momentum or a worse track fit are suppressed. In addition, every measurement assigned to a track candidate increases the score by a specific weight, based on the expected

number of measurements in the respective sub-detector and its resolution. As holes¹ are an indication of a badly reconstructed track, they reduce the score.

During the ambiguity solving, tracks are required to fulfill additional requirements. One of them is limiting the number of pixel and SCT clusters which are used by multiple tracks. These so called *shared* clusters can be an indication of clusters wrongly assigned to a track. At the same time, a merged cluster is expected to be assigned to multiple tracks. To decide if multiple track candidates are allowed to use the same cluster, or if they should be penalized for doing so, one needs a method to identify merged clusters. A first attempt to do so with the help of neural networks has been introduced to ATLAS during Run 1, and a detailed description of these neural networks is provided in Reference [25]. Correctly identifying merged clusters does improve the cluster assignment and track reconstruction efficiency, while at the same time decreasing the rate of badly measured tracks. Tracks may not share more than two clusters, and a cluster may not be shared by more than two tracks. Only track candidates which were accepted before the currently considered track are used to determine if a cluster is shared. In case an additional shared cluster would bring the current, or any of the previous, track candidates above the maximum number of shared clusters, this cluster is removed from the track candidate. In such cases, the score of the track is recalculated and it is added back to the list of track candidates which are to be processed. This score would become zero, if the updated track candidate fails any of the basic minimum cluster or hole requirements. Track candidates with a score of zero are rejected. The flow of track candidates through the ambiguity solver is shown in a simplified form in Figure 9.

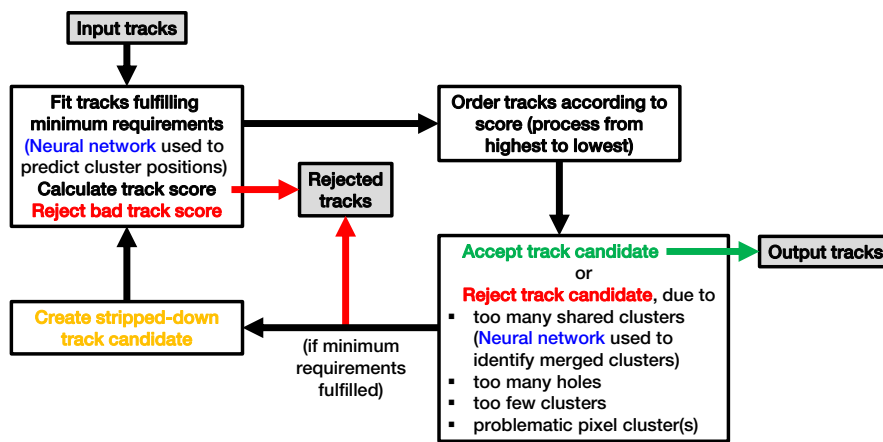


Figure 9:
Sketch of the flow of tracks through the ambiguity solver.

Finally, a high resolution fit is performed for all tracks which were not rejected by the ambiguity solver. This is only done at this point, to minimize the computing resources used by the fitter.

¹ A hole is an intersection of the predicted particle's trajectory with an active sensor element from which no measurement is assigned to the track (inactive sensors are excluded from this definition).

4.4 TRUTH-BASED RECONSTRUCTION

An ideal detector level performance, without any inefficiencies due to the reconstruction algorithms, is used as a benchmark for several results in the following sections. This is obtained from a truth-based² reconstruction approach [26], which replaces all steps described above apart from the final track fit. Clusters are assigned to track candidates based on truth information skipping the pattern recognition completely. The resulting track candidate must only fulfill a minimum silicon cluster requirement, be above the same minimum p_T as reconstructed tracks, and produce a successful track fit. This results in perfect cluster assignment efficiency and in the maximum achievable reconstruction efficiency with the ATLAS detector. These tracks are referred to as *pseudo-tracks*.

4.5 TRUTH-BASED TRACK QUALITY

In simulation, tracks are classified using a truth matching probability, defined as the fraction of measurements originating, from the same simulated particle. It is calculated via

$$\Pr_{\text{Particle}}(\text{Track}) = \frac{\sum w_{\text{Det}} \times n_{\text{Meas}}^{\text{Track}}}{\sum w_{\text{Det}} \times n_{\text{Meas}}^{\text{Particle}}}, \quad (3)$$

where $n_{\text{Meas}}^{\text{Track}}$ is the number of measurements from the simulated particle used by the track, $n_{\text{Meas}}^{\text{Particle}}$ the actual number of measurements created in the detector by the simulated particle, and w_{Det} a sub-detectors specific weight (10 for measurements in the pixel detector, 5 for the SCT and 1 for the TRT). A properly reconstructed track is required to have a truth matching probability above 0.5, and only those tracks are considered in the presented results from simulation. Tracks below that requirement are considered to be *fake tracks*.

² *Truth* refers to all information taken directly from MC simulation, and which is not available in data.

ALGORITHMIC IMPROVEMENTS TO THE TRACK RECONSTRUCTION

Chapter 4 described the ATLAS track reconstruction and touched upon some of the aspects crucial for tracking in dense environments (TIDE), for example the concept of shared clusters. This setup was overhauled to prepare the offline reconstruction for the challenges of LHC Run 2, and to improve the overall performance. Being the key step for dense environments, the ambiguity solver received the largest updates. Particularly the handling of merged clusters was revised. This chapter gives an overview of these changes. Most of the content in this and the next chapter has been previously presented in Reference [27] with significant contributions from the author of this thesis.

5.1 SAMPLES

Simulated samples of single particle decays with very close-by charged decay products were created to study the performance of the track reconstruction on event topologies with highly collimated particles. This was achieved by generating parent particles with a flat transverse momentum spectrum from 10 GeV to 1 TeV within $|\eta| < 1$. A sample with two highly collimated tracks ($\rho \rightarrow \pi^+ \pi^-$) and a sample consisting of a single τ -lepton decaying to three charged hadrons ($\tau^\pm \rightarrow \pi^+ \pi^- \pi^\pm \nu_\tau$) is used. In addition, a sample of single B^+ , decaying into a higher multiplicity of charged particles at a significant radius from the luminous region, is used.

In the next Chapter, 6, additional samples are used of a Z' with a mass of 3 TeV decaying to a pair of top quarks. These events were simulated using the PYTHIA 8 [28] generator with the AU2 [29] tuned parameters and the MSTW 2008 LO [30] parton distribution functions (PDF) sets. Effects due to multiple pp interactions in the same and adjacent bunch crossings (*pile-up*) are considered by overlaying, on average, 41 minimum bias events simulated with PYTHIA 8. A value of 41 was the anticipated average number for the pile-up per bunch crossing during Run 2, before the run began.

5.2 MERGED CLUSTERS ON RECONSTRUCTED TRACKS

ATLAS uses an artificial neural network (NN) to identify merged pixel clusters during the reconstruction. ToT information in combination with shape and physical location of clusters within the detector provides enough discriminating information for the NN. Due to the inherent randomness of the charge deposition process of charged particles in the pixel detector, the ultimate performance of such a technique is limited. Emission of low energy δ -rays can also be problematic, since they can lead to larger than expected ToT values and larger than average clusters. This can also have a negative impact on the spatial resolution achievable for pixel clusters. Failing to identify merged clusters has a negative impact on the track reconstruction efficiency, can lead to in-

creased rates of shared clusters, and influence the number of holes on reconstructed tracks.

In the original setup used during Run 1, the NN's output was used directly during the clusterization. Clusters identified as merged were physically copied (*split*). Based on the information from additional NNs predicting the particles intersections with the cluster, the positions of the copied clusters were updated. This approach has several weaknesses. During clusterization there is no available information on the track candidates associated with the cluster, so there exists no accurate information of the expected incident angle of the particle with respect to the pixel sensors. Since this information is highly correlated with the cluster shape and the measured ToT, it can significantly improve the NN performance. Figure 10 demonstrates this by comparing the rate of incorrectly split one-particle clusters versus the rate of non-split two-particle clusters for NNs both with and without the track information. In the former case, the physical position of the pixel module with respect to the luminous region position is used as an approximation of the average expected incident angle. For the same false positive rate for one-particle clusters, the efficiency to correctly identify merged clusters was 15% higher using the track information in Run 1.

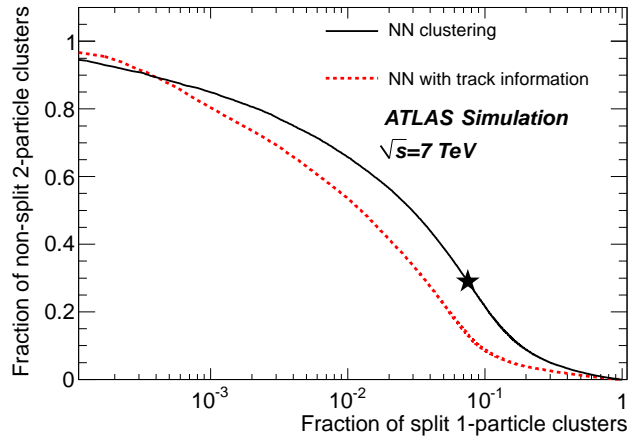


Figure 10: Fraction of pixel clusters falsely identified as merged (*split*) versus the fraction of correctly identified merged clusters from two particles in simulation. The performance of the NN using the track information is compared to the NN only using the luminous region information. The star represents the working point for Run 1 and the setup without track information. [25]

In addition to an underperforming NN, an additional load is put on the CPU and memory resources due to the duplicating of clusters. In particular the resource expensive combinatorial track finding suffers significantly under the additional clusters. Even for environments without real merged clusters, the NN has a non-negligible false-positive rate of around 10%, also visible in Figure 10. As a result, delaying the use of the NN until the ambiguity solver stage, where precise estimates of the incident angles of the tracks are available, does not only improve its identification power, but simultaneously reduces the number of track candidates that need to be processed by about 10%. This results in a reduction of the required CPU and memory resources.

Not treating pixel clusters as isolated objects, but rather in a global picture including track candidates, opens the door for additional developments. In the updated setup, the NNs output is only requested in case a cluster is assigned to more than one track at the ambiguity solver stage. As such the false-positives have negligible impact on the track reconstruction performance. Previously, clusters assigned to multiple tracks were only allowed as shared clusters, as described in Section 4.3. Now such clusters can be used by multiple track candidates without penalty if the NN identifies them as merged. This introduced the designation of *shareable* pixel cluster, while at the same time retiring the previously used definition of split clusters. Clusters marked as shared still exist. These are not identified as shareable but used by multiple tracks, and are subject to the restrictions mentioned in Section 4.3.

In cases where the NN fails to identify a merged cluster, due to its residual inefficiencies, information from other clusters assigned to the track can be used to still mark it as shareable. Since the separation between particles usually increases with increasing radius from the interaction point, it is likely that a cluster merged in layer n is also merged in layer $n - 1$. If a cluster is shareable in layer n , and a cluster on the same track in layer $n - 1$ is assigned to multiple tracks, yet the NN does not identify it as merged, it is still marked as shareable.

Motivated by these changes, a re-optimization of the minimum likelihood for a cluster to be identified as originating from two (three or more) particles based on the NN output is in order. Working points of 0.6 (0.2) maximize the track reconstruction efficiency while keeping the fake rate well under control. Further measures to maximize the quality of the tracks passing the ambiguity solver are discussed in Section 5.3.

Figure 11 compares the distributions of three different categories of pixel cluster created from the decay products of a single ρ and τ versus the p_T of the mother particles. The actual average number of merged pixel clusters is compared to the average number of split clusters in the baseline and shared clusters in the TIDE reconstruction setup. Based on truth information, the actual number of merged clusters is determined by the number of clusters where more than one simulated particle deposited energy into. With increasing p_T , the separation between the two (three) charged decay products of the ρ (τ) decreases, which is reflected by the increase of merged clusters labeled as *Ideal*. Clusters marked as shareable in the TIDE setup closely follow the Ideal distribution, suggesting that this definition is adequate. As expected, at very low p_T both of them converge to zero. Contrary to this, the Baseline distribution suffers from false-positives of the NN and stays well above zero.

At high p_T , there is a lack of clusters marked as shareable/split in both reconstruction setups, but much less prominent for the optimized TIDE setup. This effect is exacerbated in the τ decay, where merged clusters can be created by more than two particles.

Cluster assignment efficiency is an important measure of the performance of a track reconstruction algorithm. It measures the efficiency with which a cluster created by a charged particle is correctly assigned to the reconstructed track associated to that particle. Figure 12 shows this efficiency for the IBL and B-layer. For the Baseline setup a sharp drop in efficiency is apparent for small minimum separations between particles. For tracks from the ρ decay, the TIDE setup recovers 17% (13%) efficiency at a minimum separation on the order of a single pixel size for clusters on the B-layer

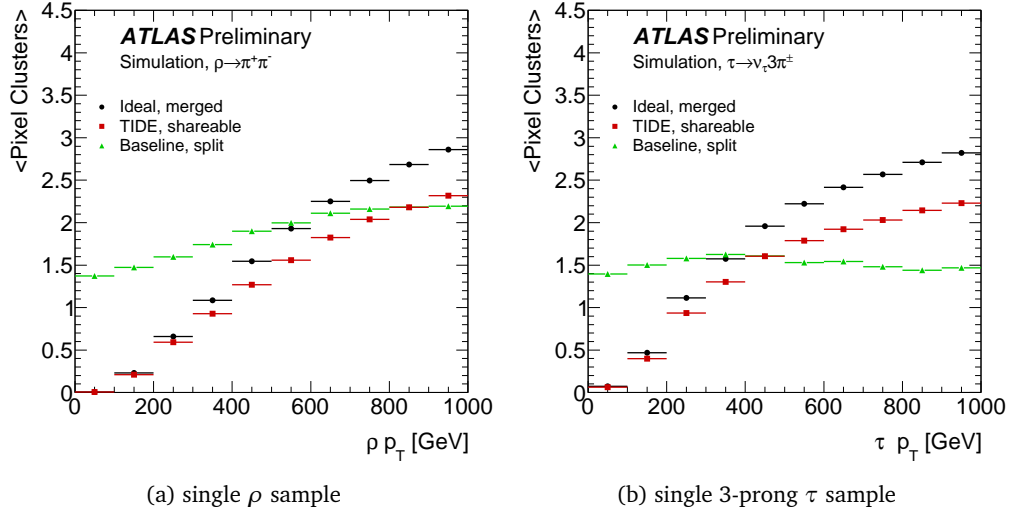


Figure 11: Average number of merged pixel clusters (based on truth information) and split (shareable) pixel clusters shown as a function of the (a) ρ and (b) τ transverse momentum.

(IBL). Compared to the resulting 98% cluster assignment efficiency for tracks from the ρ decay, the overall efficiency for clusters in the B^+ decay is lower due to the particles non-zero lifetime and higher multiplicity in charged decay products. Still, the efficiency was increased at the smallest separation from 48% to 67% for clusters on the IBL and from 62% to 94% for clusters on the B-layer. Similar improvements were also achieved for the remaining layers of the pixel detector.

Figure 13 shows the average number of pixel clusters on track for events of single ρ and 3-prong τ decays versus the p_T of the parent particle. The average number of pixel clusters on tracks from the decay products of the ρ and 3-prong τ as a function of the p_T of the parent particle are shown in Figure 13. Evidently, the number of clusters on track for the TIDE setup follows closely the expected number based on truth information, labeled Ideal, while for the Baseline setup the distribution diverges. This directly relates to the observations in Figure 11: since at high p_T the Baseline setup fails to identify most of the merged clusters, they are removed from the track candidate because of the limitation on the maximum number of shared clusters. With large enough boost, the 3-prong τ decay can occur after the IBL, so the expected average number of clusters decreases with the p_T of the τ . Both the Baseline and TIDE setup mirror that behavior, whereas the later again shows a significantly improved performance. A residual inefficiency in assigning all clusters to the reconstructed track remains for the 3-prong decay, due to clusters created by more than two particles and the corresponding higher inefficiencies of the reconstruction. Compared to the Baseline the revised TIDE reconstruction setup recovers on average up to 0.3 (0.45) pixel clusters on track from the ρ (τ) decay.

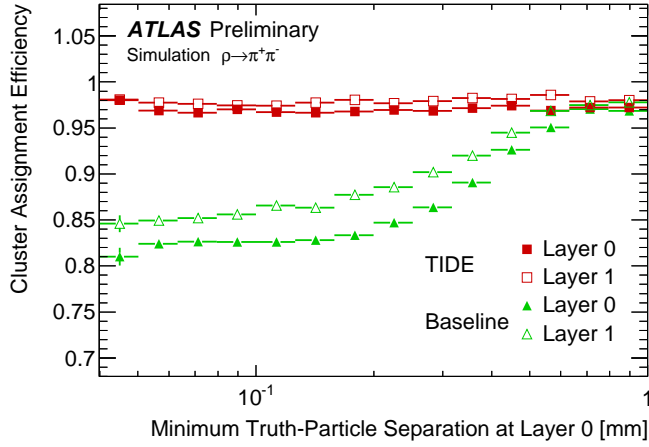
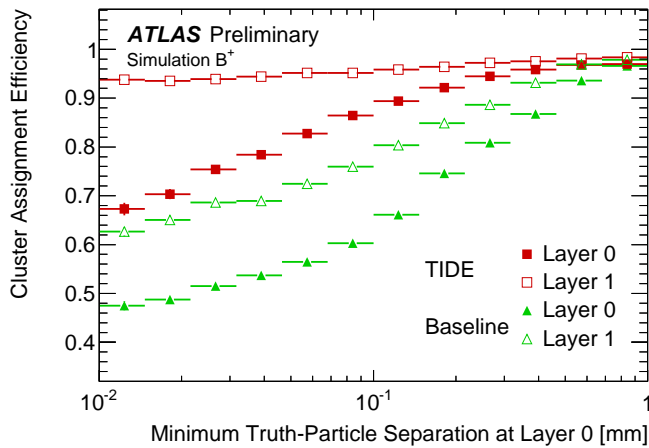
(a) single ρ sample(b) single B^+ sample

Figure 12: Efficiency with which a cluster created by a charged decay product of the (a) ρ and (b) B^+ is correctly assigned to the reconstructed track associated to that particle for the IBL and B-layer as a function of the minimum truth particle separation at the IBL.

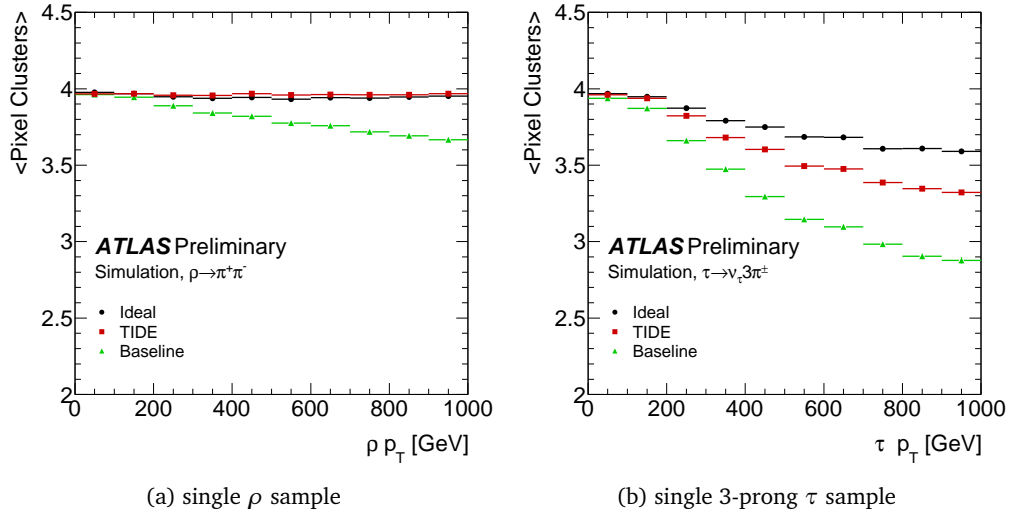


Figure 13: Comparison of the average number of pixel clusters on track for the Ideal, Baseline and TIDE reconstruction setup as function of the parent particle p_T in single (a) ρ and (b) τ events.

5.3 LIMITATIONS ON SHARED CLUSTERS

A first mention of how the updated ambiguity solver in combination with the NN can limit the negative effects from shared pixel clusters was given in the previous section. The NN is not just able to identify merged clusters, but also to tag those created by a single particle. Using this information, one can add a requirement based on the NN output, in order to allow a cluster to be shared between multiple tracks. Pixel clusters with a predicted likelihood of being created by two particles of less than 0.05 cannot be shared. This serves as an additional mean to limit the number of fake tracks. Also, a track must have a minimum of nine clusters associated with it in order to allow any of these clusters to be shared with another track. This directly counteracts the fact that many mismeasured tracks arise from secondaries created in the outer layers of the ID, for example by inelastic interactions of the particles with the detector material. Tracks from these particles are likely to get clusters in the inner layers wrongly assigned to them. Further, tracks are required to have a minimum p_T of 1 GeV and at least four SCT clusters associated with it which are not shared with another track in order to mark a pixel cluster assigned to it as shareable. Tuning was also performed on how the ambiguity solver counts the number of shared clusters. In Run 1, once a track candidate passed the solver, its shared cluster count was fixed. This could lead to cases where a subsequent track increases the number of shared clusters on an already accepted track, and at a certain point, the already accepted track could violate the maximum shared cluster requirement. In the optimized setup, no track will be accepted if it either fails the maximum shared cluster requirement itself, or causes any previously accepted track to do so, which eventually favors higher scored tracks.

In summary, major changes compared to Run 1 are:

1. Delaying the evaluation of the pixel cluster NN from the clusterization to the ambiguity solving.

2. Introducing the denomination of shareable cluster, while at the same time abolishing split clusters:
 - Pixel clusters identified by the NN as merged, and assigned to multiple tracks, are shareable.
 - Pixel clusters assigned to multiple tracks but not identified by the NN as merged are shareable if the next outward cluster of the track is a shareable cluster.
 - Shareable clusters are not penalized for being used by multiple tracks (split clusters were not allowed to do so at all).
3. Existing cuts tuned to optimize efficiency and fake rejection:
 - Minimum NN likelihood of two particle hypothesis for shareable cluster: 0.6
 - Minimum NN likelihood of more than two particle hypothesis for shareable cluster: 0.2
 - Maximum NN likelihood of two particle hypothesis for shared cluster: 0.05
 - Minimum number of pixel plus SCT clusters required to allow a cluster to be shared by a track: 9
4. Additional cuts to allow designation of a cluster as shareable (suppresses fake tracks):
 - Minimum number of SCT clusters used only by the track candidate: 4
 - Minimum track candidate p_T : 1 GeV

Due to the lack of charge information from the detector, the track reconstruction does not possess the possibility to identify merged SCT clusters in the same way as it does for pixel clusters. Since loosening the shared cluster requirement (maximum two per track) would disproportionately increase the rate of badly reconstructed tracks, this puts an inherent limit on the currently achievable track reconstruction efficiency in dense environments. Assuming perfect identification of merged pixel clusters, Figure 14 demonstrates this effect based on the efficiency of reconstructing all tracks of the charged decay products from ρ and τ decays. This result is not based on actual reconstructed tracks, but rather on the truth-based tracks introduced in Section 4.4. The only factor limiting the efficiency is the requirement of a minimum number of clusters on each track, and the varying requirement on the maximum number of shared SCT clusters. At higher momentum the decay products of the ρ and τ become so collimated, that on average even at the radius of the SCT their clusters merge.

Disentangling this effect, Figure 15 shows the actual efficiency to reconstruct all primary tracks where none are expected to share more than two clusters in the SCT. The comparison between the Baseline and TIDE setup at high p_T reveals a clearly higher efficiency of the later, due to the improvements in handling merged pixel clusters. Another factor limiting the achievable efficiency are inelastic interactions of the particles with the detector material. Therefore, the algorithmic efficiency without these interactions is almost 100% for the ρ , and slightly lower for the τ . A residual inefficiency remains at high p_T , where errors of the pattern recognition and the NN can lead to

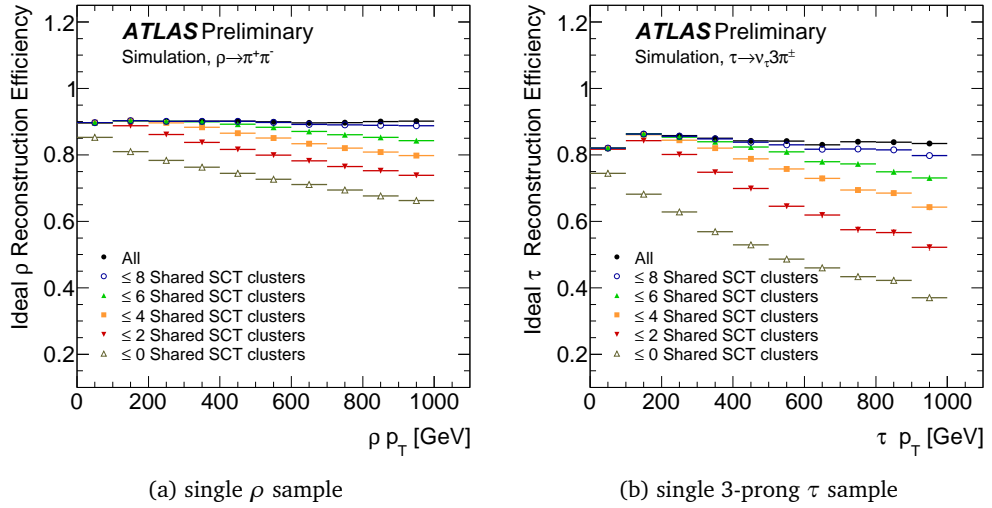


Figure 14: Truth-based efficiency to reconstruct all tracks of the charged decay products from (a) ρ and (b) τ decays. It is assumed that merged pixel clusters will always be identified as such, and only the requirement on the number of shared SCT clusters is varied.

incorrect cluster assignments, which ultimately lead to a failure to classify the track as being good. In events where secondary particles from interactions add additional clusters, and possible confusion, this effect is more evident.

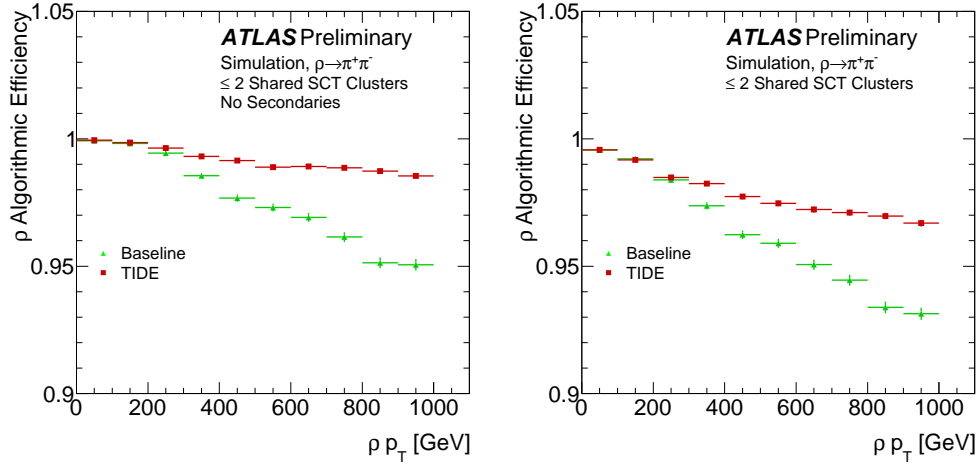
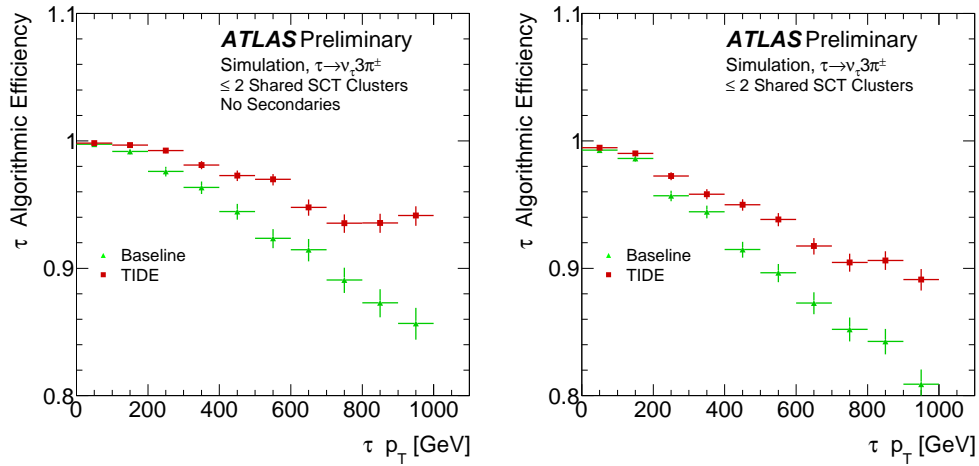
(a) single ρ sample(b) single 3-prong τ sample

Figure 15: Efficiency to reconstruct all primary tracks from (a) ρ or (b) 3-prong τ decays as a function of the parent p_T . Based on truth information, none of the tracks are expected to share more than two SCT clusters. Left: primary particles generate no secondary particles through inelastic interactions with the detector material. Right: no requirement on the generation of secondary particles.

6.1 JET RECONSTRUCTION

Jets are collimated streams of particles resulting from the production and hadronization of high energy quarks and gluons. Energy deposits from these particles in the calorimeter cells, or the reconstructed charged particle tracks, serve as input to the jet reconstruction. Most calorimeter-based methods reconstruct the jet four-momentum from the magnitude, direction and topology of the deposited energy. ATLAS uses topologically adjacent calorimeter-cell clusters (topo-clusters [31]) as inputs to the jet finding algorithms, and treats them as massless four-vectors of energy $E = \sum E_{cell}$. The jet finding then tries to combine four-vectors which are likely to originate from the same quark or gluon using two p_T weighted distances between them. The first distance d_{ij} between two four-vector i and j can be defined as

$$d_{ij} = \min(p_{Ti}^a, p_{Tj}^a) \times \frac{\Delta R_{ij}}{R}, \quad (4)$$

where a is an algorithm specific coefficient, ΔR_{ij} is the angular distance between the two four-vectors and R is the radius parameter defining the final size of the reconstructed jet. The second distance is defined as $d_{iB} = p_{Ti}^a$ and describes the separation between a four-vector and the beam axis in the momentum space.

Each jet algorithm based on these distances finds the minimum of d_{ij} and d_{iB} . If d_{ij} is the minimum, the two four-vectors i and j are combined into one, and removed from the list of four-vectors. If d_{iB} is the minimum, i is removed from the list and is designated as being a final jet. This is repeated until all four-vectors, within $\Delta R_{ij} < R$, are assigned to a final jet. Two different values of a are used within the context of this thesis: $a = 2$ and $a = -2$. They correspond to the so-called k_t and anti- k_t algorithm [32]. The former prefers to assign lower p_T particles to the jet first, which makes it sensitive to noise effects as pile-up. However, it does perform well when resolving subjets (i.e. jets reconstructed with a smaller R parameter within a jet reconstructed using a larger R parameter). The negative a value of the anti- k_t algorithm results in reconstructed jets most sensitive to high p_T contributions, which makes it stable against any noise effects. At the same time, it is unable to resolve any substructure [33] by building small R jets. Figure 16 shows the same truth-level particles clustered by the two different algorithms. While anti- k_t has a very robust reconstructed jet area, the k_t algorithms jet's area clearly varies significantly.

Small-radius jets are built from topo-clusters, at the electromagnetic scale and then corrected on average for the effects of pile-up, using the FASTJET [34] implementation of the anti- k_t algorithm with a distance parameter $R = 0.4$. Next, a calibration to the hadronic scale is applied as documented in Reference [35]. To account for differences in the response determined by in-situ methods [35], a final correction is applied to data.

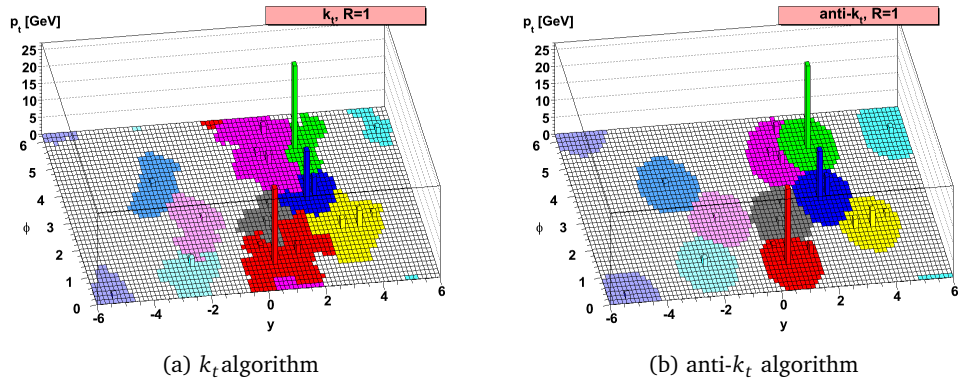


Figure 16: A sample event with topo-clusters in the ϕ - y plane clustered with two different jet algorithms, illustrating in color the areas of the resulting final jets. [32]

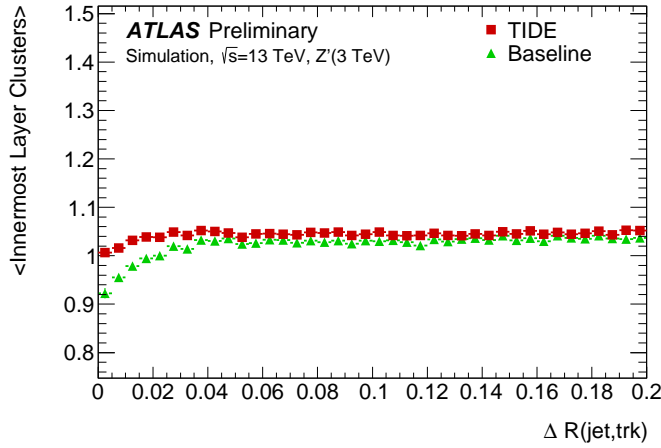
Large-radius jets are also formed with the anti- k_t algorithm, but with a distance parameter $R = 1.0$. The local cell signal weighting (LCW) method [31] is used to calibrate calorimeter-cell clusters to the hadronic scale, which are then used as input to form large-radius *calorimeter jets*. To reduce noise effects, like pile-up, the k_t algorithm is used to build subjets with a distance parameter $R_{\text{sub}} = 0.2$ within the large-radius jet, and removing any constituents of subjets with p_T less than 5% of the large-radius jet p_T . This procedure is referred to as *trimming* [36]. Simulation based energy and η dependent calibration factors are used to further calibrate energy and η of the jet and to remove residual detector effects [35, 37, 38]. Finally, the large-radius jet mass is calibrated as described in Section 10.2. For all results in this chapter, large-radius calorimeter jets are required to have $p_T > 200$ GeV with $|\eta| < 2.0$. Simulated particles with a large enough lifetime ($c\tau > 10$ mm), excluding muons and neutrinos, are used as inputs for *truth jets* which are built from the generated truth particles.

If in simulation a truth W/Z -boson (top quark) is associated to the untrimmed area of the large-radius calorimeter jet using the ghost association method [39], the jet is labeled a W/Z -jet (top-jet).

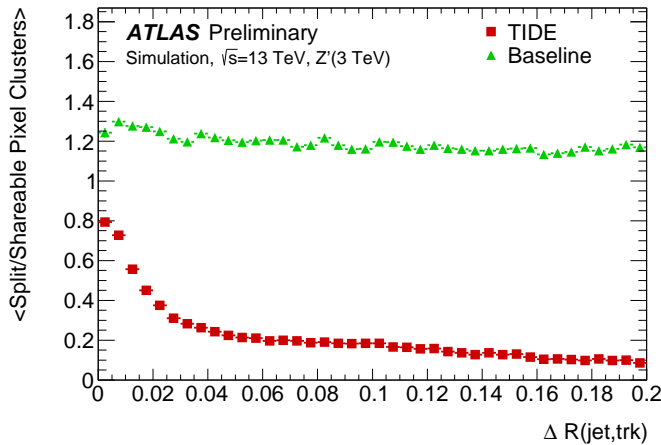
6.2 TRACK RECONSTRUCTION PERFORMANCE IN THE CORE OF JETS

In the previous sections, the differences in performance between the Baseline and TIDE setup have been shown for single particle decays. These samples demonstrated the performance in very specific topologies, thus they are not fully representative of the expected performance on physics data. The most abundant objects for which the track reconstruction encounters dense environments are high momentum jets. Figure 17 (a) compares the average number of IBL clusters on tracks inside jets from a $Z' \rightarrow t\bar{t}$ decay (introduced in Section 5.1). These jets are required to have p_T greater than 100 GeV and to be within the acceptance of the ID ($|\eta| < 2.5$). For small separations between the track and the jet axis, both reconstruction setups show a drop in the average number of clusters on track, while the effect is less prominent for the TIDE setup. Figure 17 (b) compares the distributions of clusters previously defined as split with the distribution of shareable clusters in the TIDE setup. While the Baseline

distribution does not exhibit any physical trend, the TIDE distribution shows a slight increase in the number of shareable clusters with decreasing $\Delta R(\text{jet,track})$, followed by a sharp rise for tracks in the very core of the jet. This rise is correlated with the increased particle density in the core.



(a)



(b)

Figure 17: (a) Average number of clusters from the innermost pixel layer assigned to primary tracks and (b) average number of split/shareable pixel clusters assigned to primary tracks as a function of the angular distance between the track and the jet axis. It is required that the production vertex of the particle is before the innermost pixel layer and that the jet $p_T > 100$ GeV.

A comparison of the Baseline and TIDE reconstruction efficiency for charged primary particles is presented in Figure 18 as a function of jet p_T . The Baseline setup shows a significant drop in efficiency at higher jet p_T , while the TIDE setup is much more robust.

In jet cores, that is, for angular distances between the charged particle and the jet axis of about 0.05 and less, a residual reconstruction inefficiency is likely. Clusters created by multiple particles are common there, similar to tracks from the previously discussed B^+ and τ decays. The track reconstruction efficiency for charged

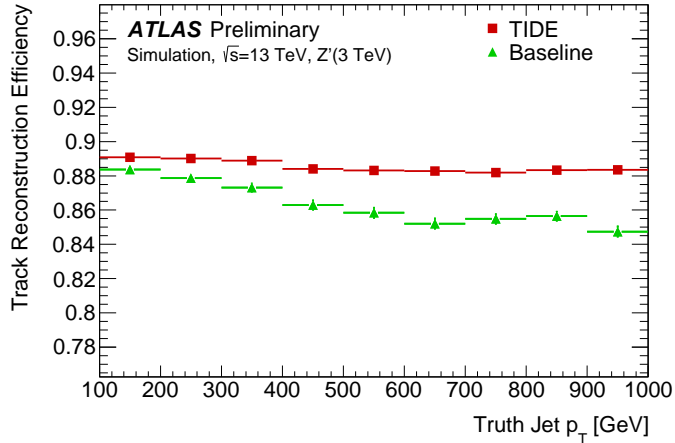
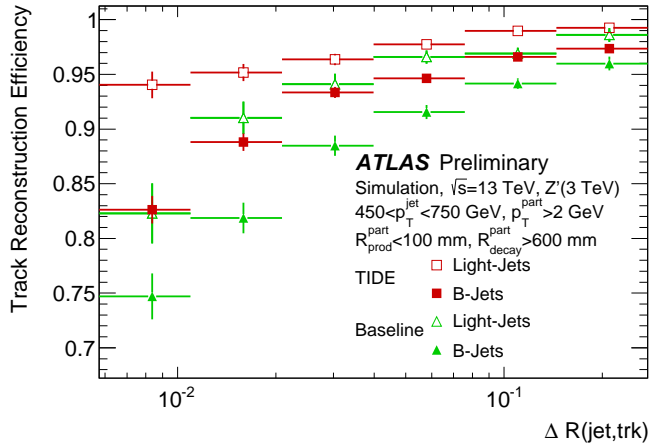


Figure 18: Track reconstruction efficiency of primary particles with a production vertex before the IBL dependent on the jet p_T .

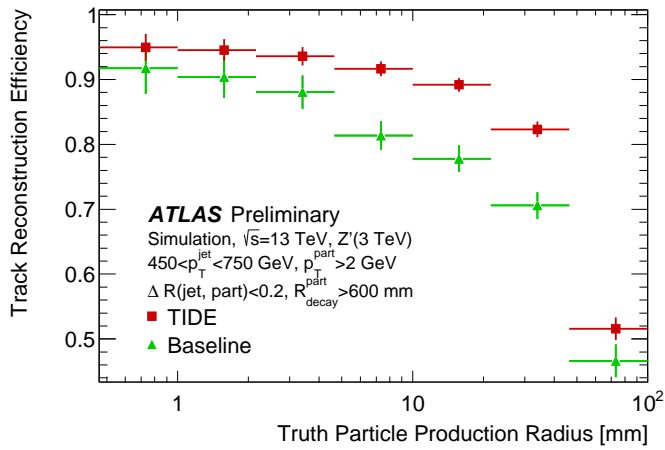
primary particles as a function of $\Delta R(\text{jet}, \text{track})$ is shown in Figure 19 (a) for jets with p_T 450–750 GeV. Charged particles used in this result need to have a minimum p_T of 2 GeV, must have been created within a radius of 100 mm from the center of the detector, and must not decay or undergo inelastic scattering within the SCT volume ($R_{\text{decay}}^{\text{part}} > 600$ mm). Due to displaced decays of heavy flavor quarks, the observed inefficiency at low angular separations is worse for b -jets. An improvement of 10% (14%) is achieved in the core of light (b) jets with the TIDE reconstruction setup. With the TIDE setup, the same track reconstruction efficiency within b jets is achieved than was previously possible in the Baseline setup for light jets. Figure 19 (b) shows, with the same selections as Figure 19 (a), the track reconstruction efficiency for charged primary particles as a function of the production radius of the particle. Two main effects will reduce the efficiency at higher production radii. Firstly, decays occurring immediately before a pixel layer will lead to an increased probability of merged clusters from several charged particles. Secondly, the total number of created clusters in the detector will decrease if the the particle is created after the n^{th} pixel layer. The latter results in a sharp drop in efficiency down to around 80% and 50% at a production radius above 33 and 50 mm (the radii of the IBL and B-layer). For particles created close to the IBL, an increase in efficiency of 17% is achieved with the TIDE reconstruction setup.

6.3 IMPLICATIONS FOR FLAVOR TAGGING

Several techniques exist to identify jets containing b -hadrons, though all of them in some way seek the characteristic displaced production vertex. This is usually achieved through an analysis of the impact parameters of the tracks or a direct reconstruction of the displaced vertex [40]. ATLAS combines the results from multiple taggers, each using a different approach to flavor tagging, through a multivariate approach to obtain the final jet flavor variable. The impact parameter based taggers are especially sensitive to mis-assignments or the lack of clusters on the reconstructed tracks, as both can directly impact the impact parameter resolution. An improved performance due to the improvements to the track reconstruction is expected. To some level, secondary vertex



(a)



(b)

Figure 19: Track reconstruction efficiency for charged primary particles as a function of (a) the angular distance between the particle and the axis of the jet and (b) the production radius of the particle.

based taggers will also see an improvement, since discriminating variables derived from the associated tracks are used.

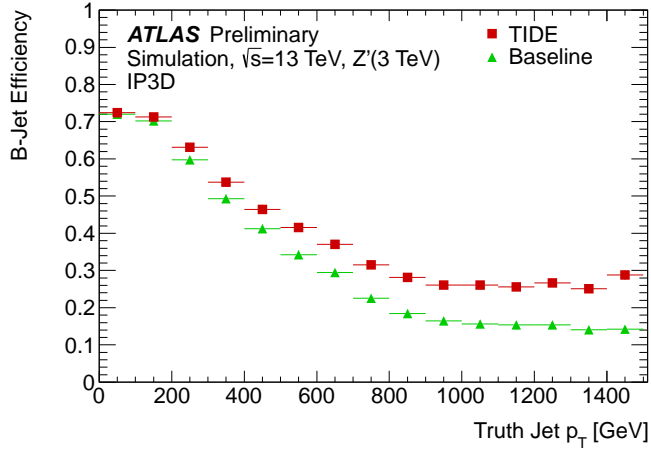
In order to evaluate the actual possible gains for flavor tagging due to the improvements of the track reconstruction, one would need to re-optimize and tune the whole set of used taggers because of the change in the inputs. Since this is beyond the scope of this thesis, only the change in performance of the IP3D tagger [41], which is expected to be most sensitive to the changed track inputs, will be presented. No optimization was performed on it, and the results shown in the following therefore serve as a lower limit on the actual resulting improvement. The b -jet tagging-efficiency, Figure 20 (a), and the light-jet rejection at the 70% efficiency working point, Figure 20 (b), are shown for different truth jet p_T for jets from the Z' decay. An increased efficiency, especially at high jet p_T , with about the same light-jet rejection is observed for the TIDE setup compared to the Baseline. Figure 21 shows the b -jet efficiency versus the light-jet rejection for all jets with a $p_T > 100$ GeV. For a light jet rejection equal to that at the 50% and 80% b -jet identification efficiency working points of the IP3D tagger, a relative increase in efficiency of 13% and 7% is obtained when using the TIDE track reconstruction setup.

6.4 PERFORMANCE OF TRACK RECONSTRUCTION IN DENSE ENVIRONMENTS WITH THE ITK

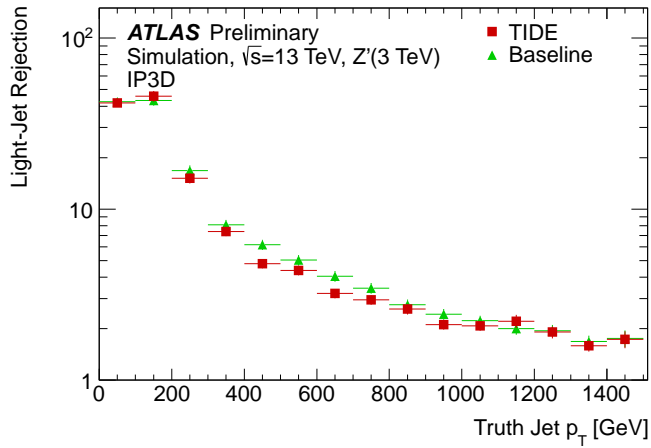
The LHC will undergo a significant upgrade with the goal of increasing its integrated luminosity by a factor of 10 in the years after Run 3 [42]. To achieve this, an event pile-up of up to 200 inelastic pp interactions per bunch crossing is necessary. To prepare the ATLAS detector for this harsh environment, the entire ID will be replaced by the new Inner Tracker (ITk) [43]. One of the main tasks of the ITk will be the reconstruction of tracks in jets in the currently uncovered very forward region of η up to 4.0. This will be crucial if ATLAS is to be able to reject pile-up jets in that region by means of track-to-vertex matching [43]. The expected tracking performance in dense environments is one of the main areas of study for the ITk preparations. Figure 22 shows the efficiency to reconstruct all tracks from the charged decay products of a 3-prong τ -decay as a function of the τ p_T for a specific candidate tracker layout. This layout differs significantly from the current ATLAS ID. Most prominently it is a silicon-only tracker made out of five pixel layers and four strip layers with strip doublet modules in the barrel, with a novel inclined sensor arrangement in the forward region. Figure 22 shows this candidate layout and its details and the reconstruction setup are described in Reference [44]. A clear degradation of the performance is visible in the very forward region $\eta > 2.7$. Such studies are crucial in determining the capabilities of proposed future detector layouts.

6.5 CONCLUSION

Optimizations provide a vastly improved track reconstruction setup in terms of performance in dense environments for Run 2. An improved performance is demonstrated for highly collimated tracks from decays of single particles, as well as in the more physical environment of hadronic Z' decays in the presence of event pile-up. Up to 10%



(a)



(b)

Figure 20: (a) b -jet efficiency and (b) light-jet rejection using the IP3D tagger at the 70% working point with input tracks from the Baseline and TIDE reconstruction setups as a function of truth-jet p_T for jets within $|\eta| < 2.5$.

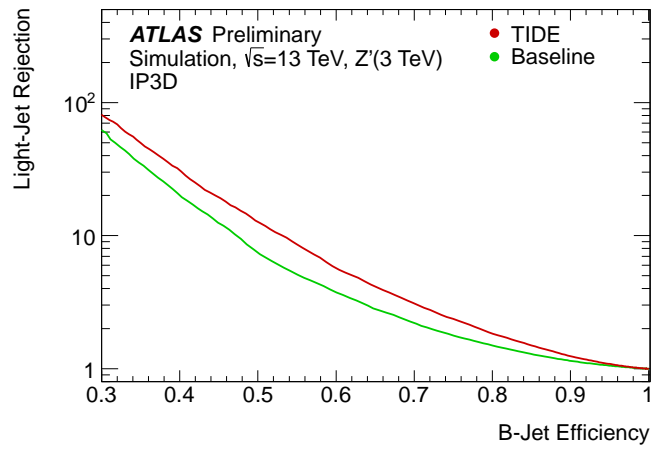


Figure 21: Light-jet rejection as a function of b -jet identification efficiency using the IP3D algorithm with input tracks from the Baseline and TIDE reconstruction setups. Jets are required to have p_T greater than 100 GeV and $|\eta| < 2.5$.

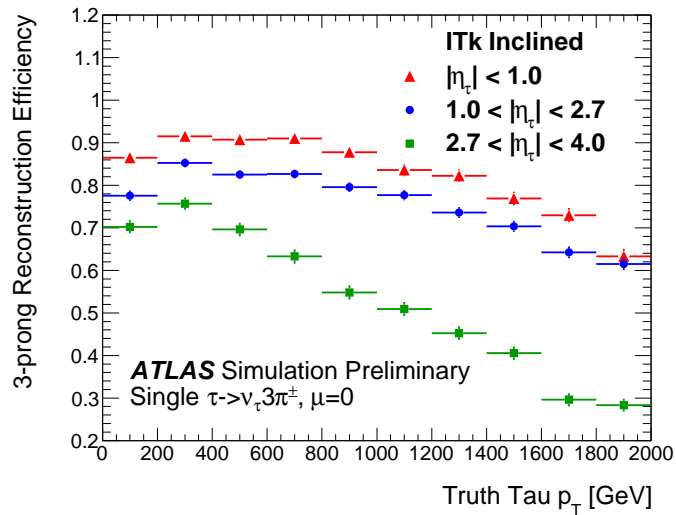


Figure 22: Efficiency to reconstruct all primary tracks from 3-prong τ decays as a function of the parent p_T with a proposed ITk tracker layout for three different η regions.

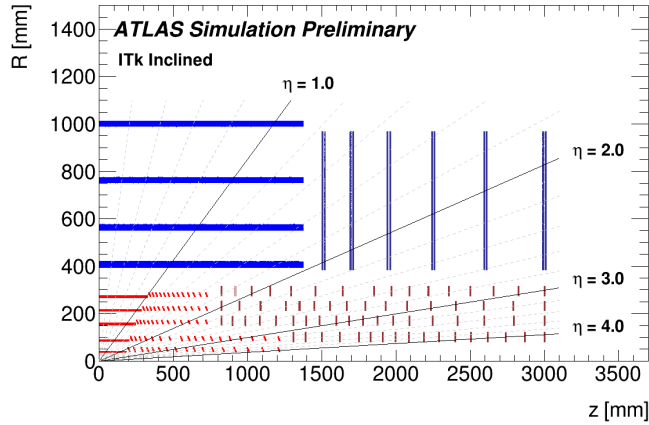


Figure 23: Diagram showing simulated energy deposits in active layers for a candidate ITk layout with an “inclined” pixel barrel, shown in the R - z plane. The pixel tracker is in red, while the strip tracker is blue. [44]

more pixel clusters are associated to tracks in the core of high p_T jets, which results in a much more robust track reconstruction efficiency. This improvement becomes most apparent for charged particles with a high production radius (>30 mm), where 17% efficiency is recovered, as well as in the core of high p_T b - and light-jets, where 10% and 14% efficiency is recovered. The higher quality and efficiency of reconstructed tracks directly boosts the performance of several derived physics objects, which was demonstrated with the example of flavor tagging, and is also relevant for the jet mass described in Chapter 10. For flavor tagging a 7–13% improvement in b -jet efficiency is achieved for a fixed light-jet rejection for jets with $p_T > 100$ GeV, using an IP3D tagger which has not been re-optimized.

Part III

MEASURING TRACK RECONSTRUCTION PERFORMANCE IN
DATA

PROPERTIES OF RECONSTRUCTED TRACKS IN DENSE ENVIRONMENTS IN RUN 2 DATA

The previous part of this thesis described the track reconstruction in dense environments and discussed its performance based on MC simulated samples. Due to imperfect modeling of the multiplicity and angular distribution of charged particles within a jet in simulation, certain discrepancies with data are expected. Simulation is also known to describe the properties of pixel and SCT clusters observed in data only to a certain level. This chapter contains comparisons of basic properties of tracks in the core of high p_T jets between data and MC simulation to probe the overall agreement between the two. Chapter 8 describes the use of data to evaluate the performance of the NN identifying merged clusters and Chapter 9 discusses a measurement of the residual inefficiency of the track reconstruction in data.

The comparisons in this chapter are mainly performed as a function of $\Delta R(\text{jet}, \text{track})$, the separation between the track and the jet axis. Tracks are associated to the calorimeter jets following the ghost association procedure. Where results from data are presented, 3.2 fb^{-1} of 2015 LHC collision data is used and standard data quality requirements are applied to select the luminosity blocks where all sub-systems of the detector were fully operational. A simulated MC sample generated with the PYTHIA 8 with the A14 [29] tuned parameters and the NNPDF23LO [45] PDF sets is used. Interactions of all generated particles with the detector are fully simulated through GEANT 4 [46] and simulation is reweighted to make sure that the average number of interactions per bunch crossing and the jet η spectra match those in data.

Besides considering the average number of pixel and IBL clusters on track as a function of the distance of the track to the jet axis, the main interest lies in the average number of shared and shareable clusters. These numbers are strongly depended on the charged particle density in the jet. The average number of tracks versus the angular distance from the jet axis in data and MC is compared in Figure 24. In data, about 5 to 10% less tracks are observed as in simulation and the discrepancy between the two becomes larger with increasing jet p_T .

Figure 25 shows the average number of shared pixel and SCT clusters on tracks in jets for data and MC versus the angular distance from the jet axis. For small distances a sharp increase in the number of shared pixel clusters is visible. Although the SCT sensors are located at much higher radii than the pixel sensors, a large numbers of shared clusters exist. This is due to the larger sensor dimensions of the SCT strips, as well the fact that no NN can be utilized to identify merged SCT clusters, as discussed for the pixel clusters in Section 4.3. The MC simulation on overall agrees well with data in the individual bins of jet p_T , but the average number of shared pixel clusters deviates from it with decreasing angular separation between the track and the jet axis. A maximum discrepancy of around 15% is observed for $\Delta R(\text{jet}, \text{track}) < 0.04$. Considering the agreement observed in Figure 24 and the fact that a simplified charge deposition model is used in simulation, such differences for pixel clusters are expected.

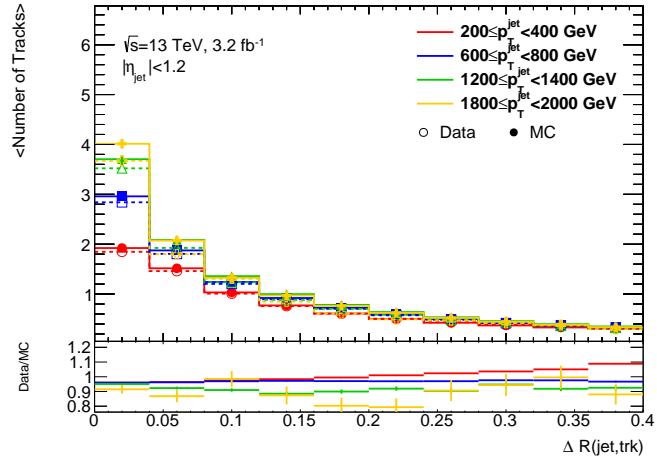
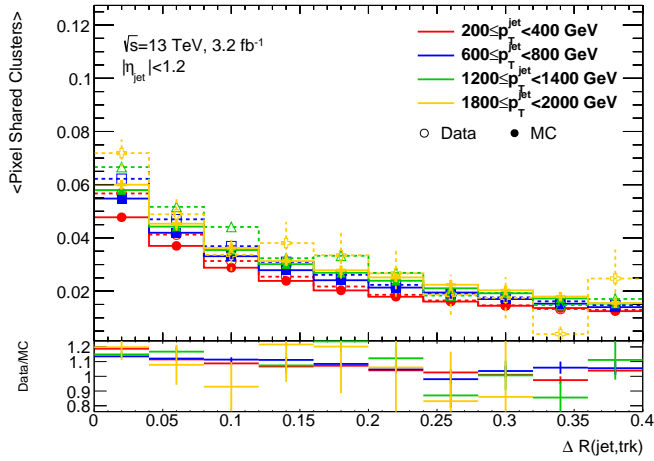
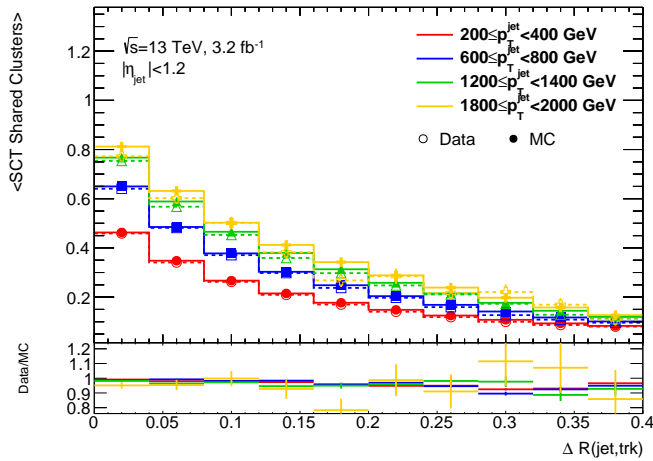


Figure 24: The average number of tracks in different bins of angular distance from the jet axis. Data and MC are compared in bins of jet p_T .

Figure 26 shows the average number of IBL clusters, and the fraction of pixel clusters which are identified as merged, on tracks in jets for data and MC versus the angular distance from the jet axis. For small separations the number of clusters shows a slight drop, while the number of shareable clusters steeply rises. MC and data show good agreement in the individual bins of jet p_T .

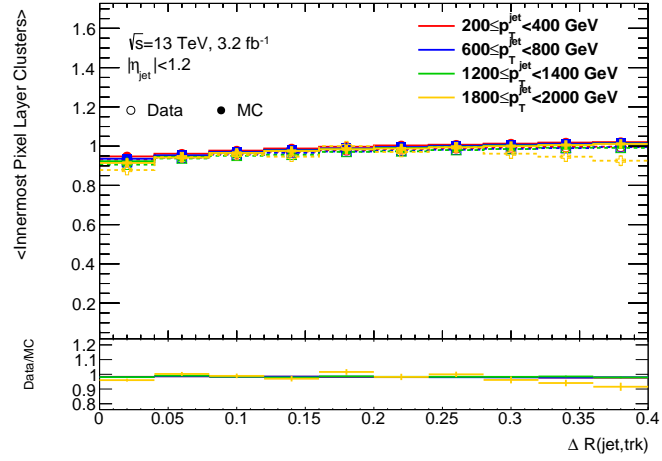


(a)

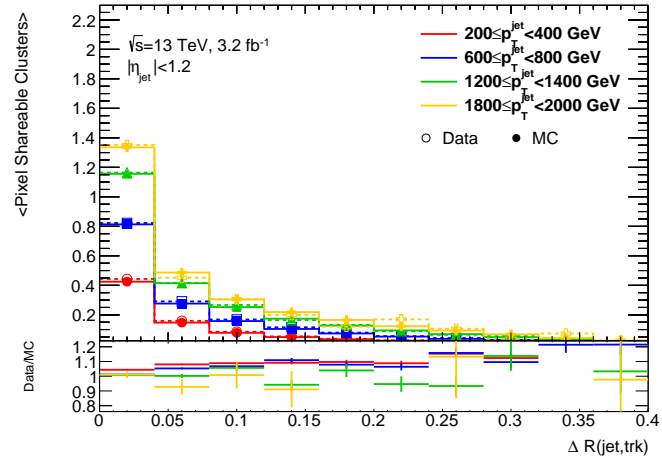


(b)

Figure 25: The average number of shared (a) pixel and (b) SCT clusters for primary tracks (with a production vertex before the first layer) as a function of the angular distance between the track and the jet axis. Data and MC are compared in bins of jet p_T and show an overall excellent agreement.



(a)



(b)

Figure 26: The average number of (a) innermost pixel layer clusters and (b) number of shareable pixel clusters on primary tracks (with a production vertex before the first layer) as a function of the angular distance between the track and the jet axis. Data and MC are compared in bins of jet p_T and show an overall excellent agreement.

It was shown in Chapters 4 and 5 that for tracks in dense environments a good performance and understanding of the NN pixel clustering used in the ATLAS track reconstruction is vital. The basic performance of this method has been presented previously based on MC simulation [25]. However, no study of the ability of the reconstruction software to identify merged clusters in data has been performed. Such a measurement from data is crucial to obtain confidence in the agreement between the output of the NN in data and MC simulation, and the related uncertainties. Two independent techniques are introduced in Section 8.1 which allow such a measurement, and results are presented in Section 8.2. The study is performed on a subset (43.4 pb^{-1}) of the data set used in Chapter 7 and the same dijet MC simulation is used. Results from this chapter have been presented in Reference [47] with significant contributions from the author of this thesis.

8.1 METHODS

The principal of both methods measuring the ability of the ATLAS track reconstruction, and its NN pixel clustering, to identify merged clusters is simple: pairs of collimated tracks are built, of which each has to pass the following selection:

- $p_T > 1 \text{ GeV}$,
- $|\eta| < 2.5$,
- Longitudinal impact parameter, $|z_0|$, with respect to the primary vertex¹ $< 5 \text{ mm}$,
- Number of clusters in the pixel and SCT ≥ 7 ,
- Number of holes in the pixel and SCT ≤ 2 ,
- Number of holes in the pixel ≤ 1 ,
- Number of shared clusters in the pixel and SCT ≤ 1 ,

To ensure that only highly collimated pairs of tracks are considered, each of them must be within a radial separation, $\Delta R(\text{track}, \text{track})$, of 0.1. Every pair in every event satisfying the above criteria is considered for this study, which results in three million pairs of tracks from data. The simulation is normalized to this number. Figure 27 compares the leading and sub-leading track p_T distribution between data and simulation. Like for other kinematic variables of the track pairs, such as the η distribution, simulation provides a reasonable description of the data.

¹ The primary vertex is identified as the reconstructed vertex with the highest sum of track p_T associated to it.

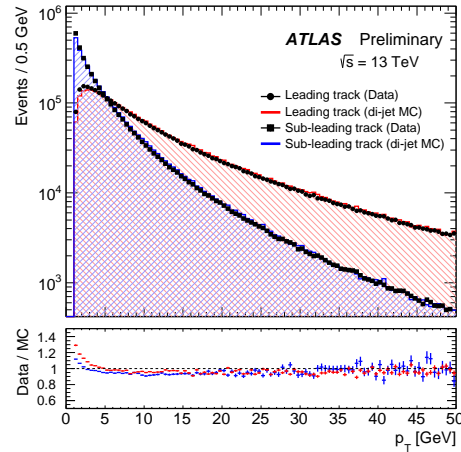


Figure 27: Comparison of leading and sub-leading track p_T distributions of selected track pairs in data and MC simulation. The simulation is normalized to match the number of track pairs in data.

8.1.1 Extrapolation Measurement

Collimated tracks from prompt particles are most likely to create merged clusters in the innermost layers. For this reason, only results for the IBL and the B-layer are presented in the following. They are obtained as follows:

- A track pair, with associated clusters in the B-layer or 3rd pixel layer is used as a starting point to measure the properties of clusters in the IBL or B-layer respectively.
- The position of the particles at the IBL or B-layer is obtained by extrapolating back along the reconstructed trajectory of the particle, while taking into account possible effects due to multiple scattering.
- If a cluster is found near the extrapolated position on the inner layer, the separation between the extrapolated position and that clusters is used as an estimate of the distance of the pair of tracks at that layer.
- Depending if the track reconstruction labeled the cluster as shareable, the found cluster is categorized as either being a
 1. single-particle-cluster,
 2. shareable cluster (used by both tracks),
 3. shareable cluster (used by only one track).

In principle, the accuracy of the extrapolation is known to be very high. Nevertheless, due to residual mis-alignments of the pixel sensors resulting from inaccurately known positions of the pixel modules, a systematic uncertainty is introduced. This uncertainty is not quantified explicitly, but qualitatively monitored with the complementary measurement described in Section 8.1.2.

Single-particle-clusters created and used by only one track are expected to constitute the majority, and most of the clusters are identified as such. If the ambiguity solver, utilizing the NN pixel clustering, tags a cluster as shareable and this cluster is used by both tracks, it will end up in the second category. In the last category, a cluster is identified as being shareable, but only one track is associated to it. For these clusters, the second track of the pair must have a cluster on the same pixel module associated to it. All three categories are illustrated in Figure 28.

The fraction of clusters in the first category is expected to decrease with decreasing separation between the tracks. At a small enough separation, on the order of the size of a single pixel, merged clusters are unavoidable. With an optimally performant reconstruction, a population inversion should be produced, and all clusters would end up in the second category for shareable clusters. Category 3 can point to imperfections in the algorithmic performance of the ambiguity solver and the NN pixel clustering, but can also arise from shortcomings of the overall track reconstruction. One example would be errors in the combinatorial track finding described in Section 4.2. Clusters in this category do not necessarily lead to a decreased track reconstruction efficiency or an increased track resolution. They are therefore merged with Category 1 for this method.

Figure 29 (a) shows a schematic of this method.

8.1.2 Measurement Using Overlap Regions

The fact that the pixel modules in the individual layers overlap can be exploited to probe the identification power of merged clusters of the track reconstruction. All pixel (IBL) staves are installed with a specific tilt of 20° (25.714°) - where the angle describes the tangent to the plane perpendicular to the cylinder axis. An angular overlap in the ϕ -direction is created, which for the IBL is 1.821° . For all layers except the IBL an overlap between modules in the z -direction also exists.

Particles passing through these overlap regions are likely to create clusters on two modules in the same layer. Similar to the method outlined in Section 8.1.1, the outer cluster can be used as a reference and the inner one can again be assigned to one of the three categories. In contrast to the extrapolation method, no extrapolation is necessary for these topologies. Since the two clusters are nearly at the same radius, the distance of the two tracks at the inner module can just be taken as the distance of the two at the outer one. Since the relative position of the two modules is known with a high accuracy, the impact of alignment related uncertainties on this method is insignificant. Furthermore, due to the small radial distance between the two modules, the “type” of the two clusters will be strongly correlated, such that if the outer cluster is a merged cluster, the inner cluster should most likely also be merged and the track reconstruction should identify it as such. Conversely, if the outer cluster is not identified as being merged, one can probe for false-positives if the inner cluster is identified as such. Any discrepancy in the categorization of the two clusters can indicate inefficiencies of the track reconstruction. An incorrect prediction by the NN pixel clustering will be by far the dominant source of such an inefficiency. Other sources, like wrongly assigning a nearby cluster to the track also exist. Figure 29 (b) sketches how this method works and Figure 30 gives a schematic view of the scenarios described above.

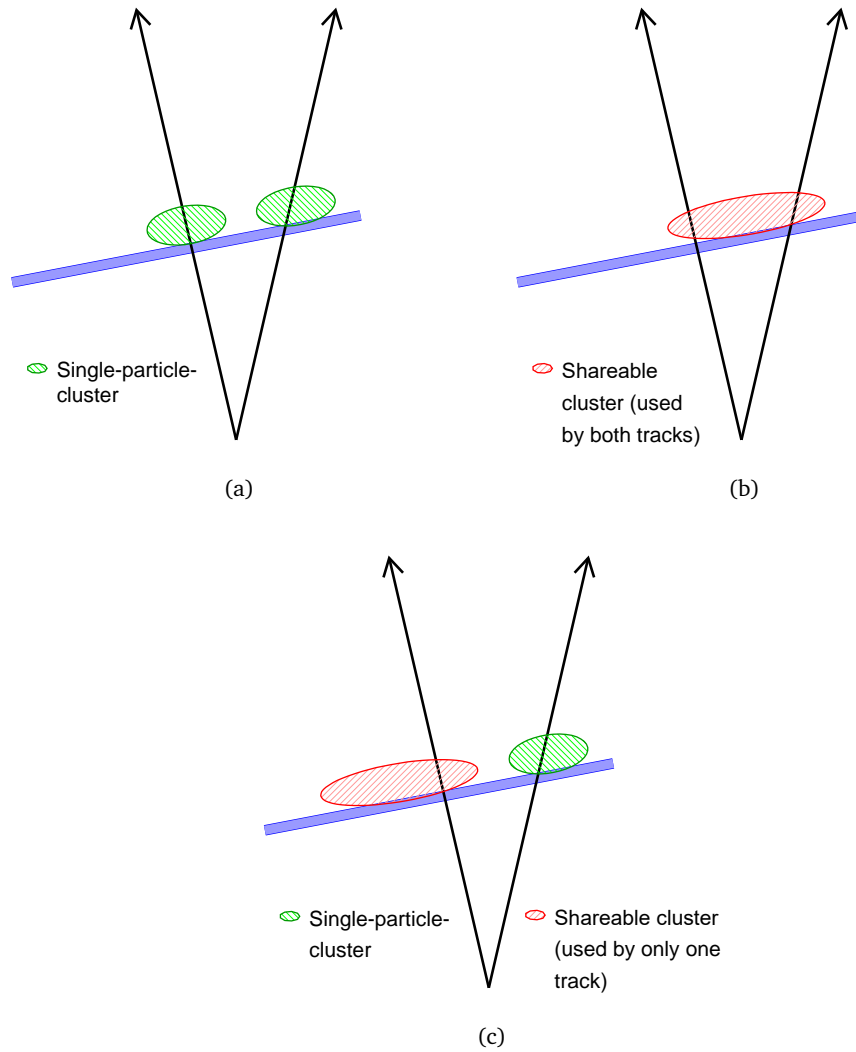


Figure 28: Illustration of the different cluster categories: (a) single-particle-cluster, (b) shareable cluster (used by both tracks) (c) shareable cluster (used by only one track). Both clusters have to be on the same module.

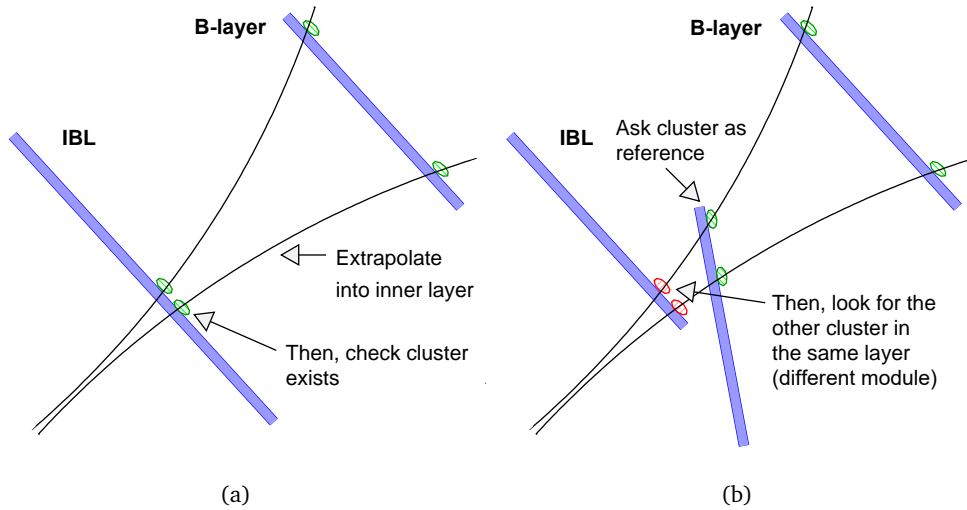


Figure 29: Sketch of (a) the extrapolation method and (b) the method using the overlap regions.

8.2 RESULTS

A qualitative agreement between data and MC simulation for the distance of two tracks of a pair at the IBL and B-layer is essential to interpret the results. Figure 31 shows that this distance is well modeled in MC simulation, with residual discrepancies of 10 to 20% at very small track separations. For the selected subset of tracks, the fraction of clusters being identified as shareable is 5.9% and 5.6% on the IBL and B-layer respectively.

Figure 32 shows the fraction of track pairs in each category as a function of the distance between two tracks. As previously explained, clusters of Category 1 and 3 are merged and called single-particle clusters in these results. As the separation between the two tracks decreases, the fraction of clusters being identified as shareable increases. Data agrees with MC simulation to within a few percent. Below a separation of the order of two single pixels (about 0.1 mm) clusters must start to merge, and a population inversion is observed. For the IBL (B-layer) the fraction of clusters identified as being shareable and assigned to both tracks reaches approximately 85% (93%) for data and simulation.

Due to imperfect modeling of pixel clusters in simulation, certain discrepancies are expected. For example, a simplified charge deposition model is used in simulation which is known to imprecisely describe the data. Furthermore, the constant radiation created by the LHC's collisions and interacting with the sensors changes the observed cluster properties with time in data, something which is not accounted for in simulation. The observed overall discrepancy in the fraction of cluster of Category 2 for the B-layer of about 10% is therefore expected. Due to the smaller longitudinal pixel dimensions in the IBL the overall higher fraction of clusters of Category 1 compared to the B-layer is reasonable.

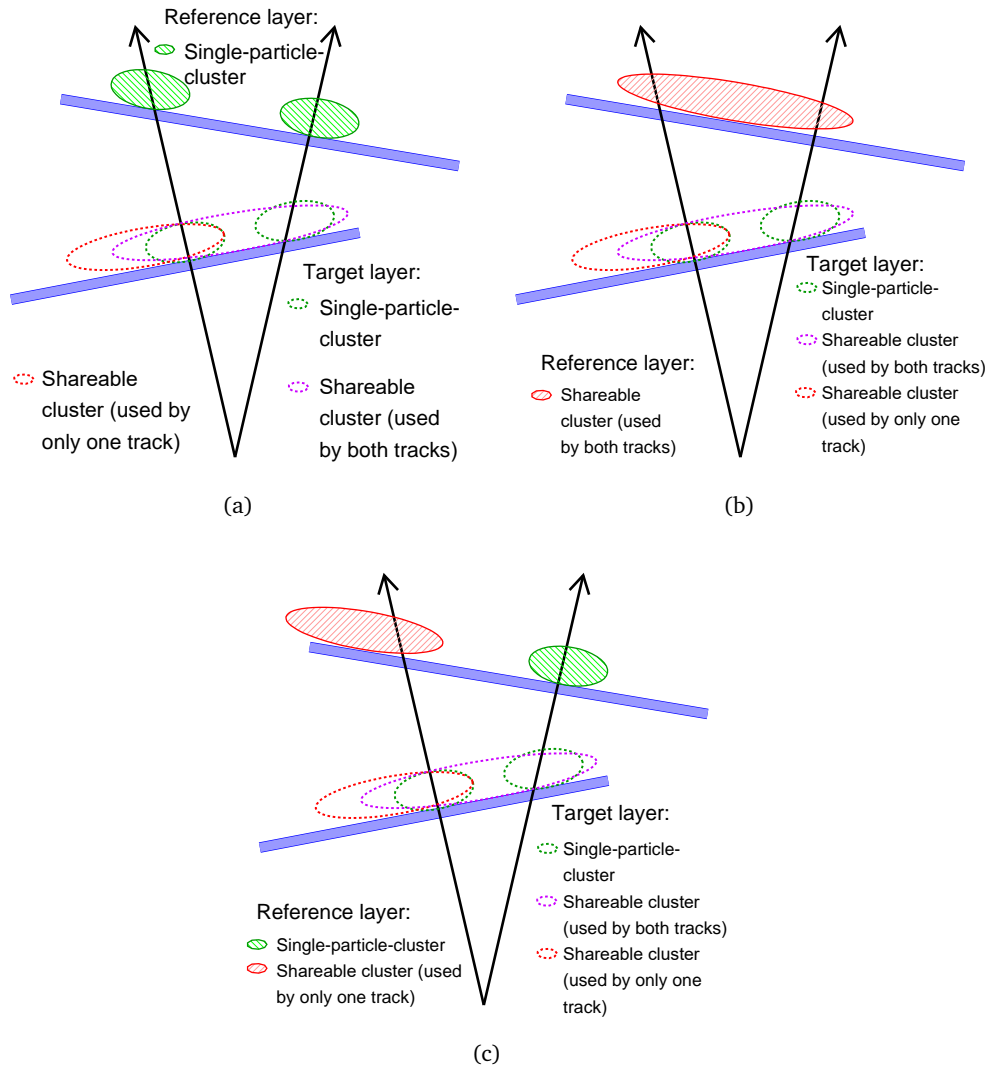


Figure 30: Illustration of the different cluster categories: (a) single-particle-cluster, (b) shareable cluster (used by both tracks) (c) shareable cluster (used by only one track), on the reference layer. For each case, the cluster on the target layer can also be from one of the three categories.

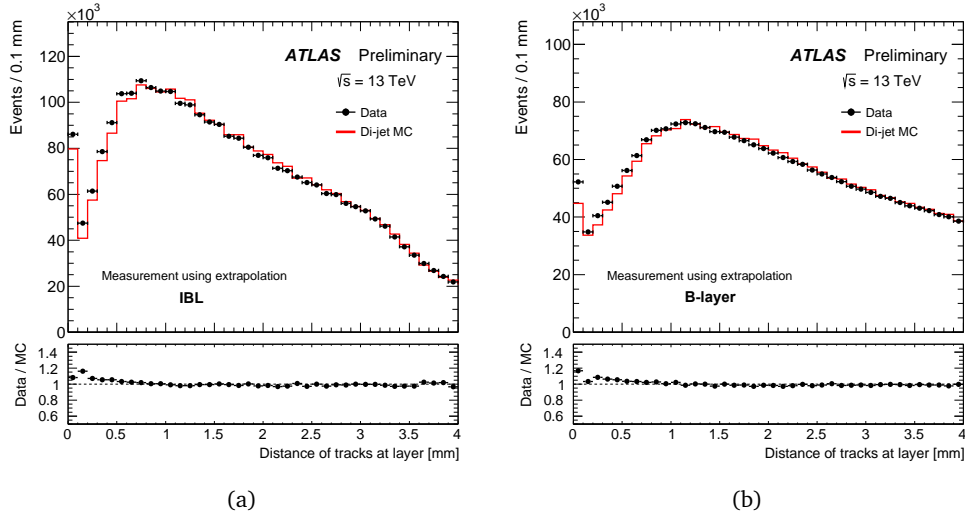


Figure 31: Distance between track pairs for (a) IBL and (b) B-layer, respectively in data and MC simulation.

Another interesting observation is that the fraction of Category 2 clusters is smaller for track distances below ~ 0.1 mm for the IBL than for the B-layer. This hints at a worse performance of the NN clustering in that layer. As pointed out in Section 3.4.1, this is due to the fact that the IBL only provides a 4-bit readout compared to the 8-bit readout used for the other pixel layers.

Distributions of the fraction of clusters in each category, from the method using the overlap region, are presented in Figure 33. Clusters from categories 1 and 3 are again merged in this figure. Compared to Figure 32, the overall features observed in all distributions are the same. For the B-layer, the fraction of clusters identified as being shareable and assigned to both tracks is approximately 95% and 90% for data and simulation, respectively. Clusters on the IBL again show a significantly lower efficiency as on the B-layer, about 80% in both data and simulation, while the overall agreement between data and simulation is within 10%. Figure 34 shows the fraction of clusters on the inner module with a different category with respect to the cluster in the outer module. For this figure the three categories are considered separately. For increasingly small separations the fraction of clusters with mismatching categories increases. Due to the smaller pixel dimensions of the IBL, this increase occurs at smaller separations than for the B-layer. At separations where clusters must merge (around 0.1 mm), there is a drop in the distribution for both the IBL and B-layer. Mismatches in the categories can arise for a variety of reasons. As described in Section 4.3, the NN pixel clustering can fail to identify a cluster as being merged, or wrongly identify it as being so. There will always be fluctuations in the shape of the clusters, even with identical incident angles. Therefore, there will never be a perfect match between the categories of the two clusters on the same layer, even if simulation would perfectly describe data.

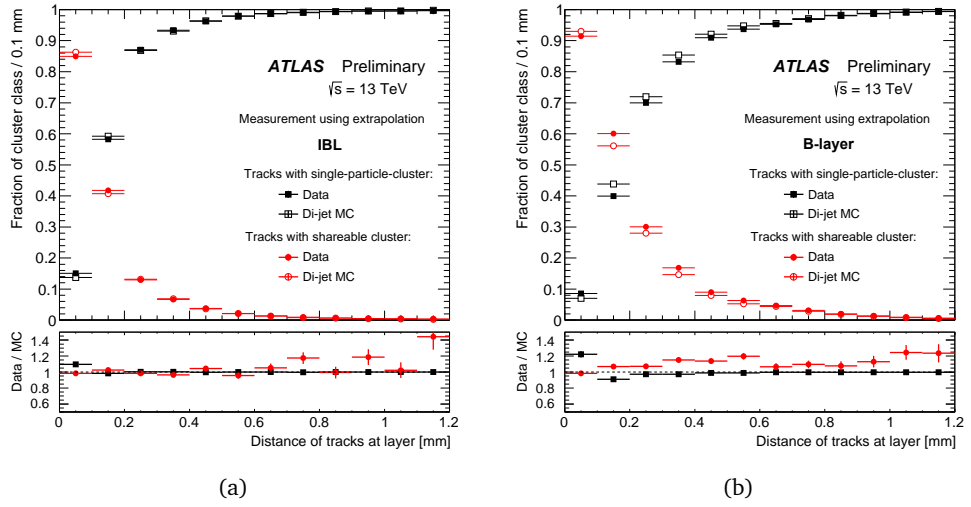


Figure 32: Fraction of tracks with single-particle and shareable clusters as a function of the distance between tracks using the extrapolation method for (a) IBL and (b) B-layer.

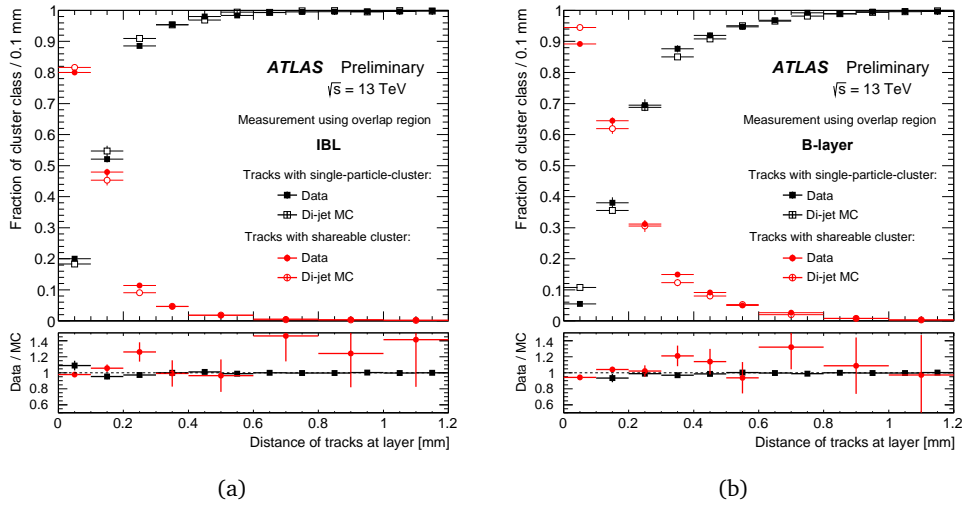
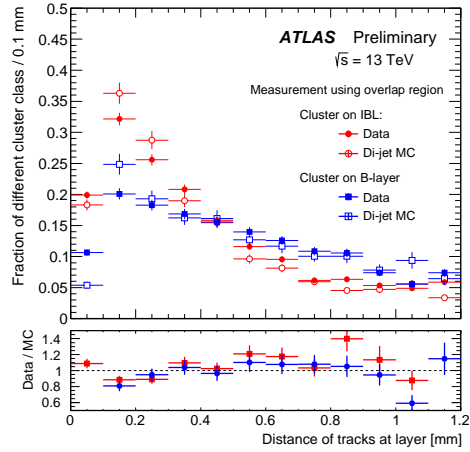


Figure 33: Fraction of tracks with single-particle and shareable clusters as a function of the distance between tracks using the overlap method for (a) IBL and (b) B-layer.



(a)

Figure 34: The fraction of tracks with mismatching categories between reference and target cluster.

8.3 CONCLUSION

Studying the properties of pixel clusters for collimated track pairs allows the probing of the identification efficiency of the track reconstruction of merged pixel clusters in data. For separations between the pair of tracks below the dimension of a single pixel, the efficiency for identifying the cluster as shareable and assigning it correctly to both tracks is above 80% for the IBL and above 90% for the B-layer. The performance of the track reconstruction is consistent between data and simulation, with residual discrepancies of 5% and 10% for the extrapolation and overlap methods respectively.

MEASURING TRACK LOSS IN DENSE ENVIRONMENTS WITH THE dE/dx METHOD

Detailed understanding of uncertainties related to the track reconstruction performance in dense environments is crucial for several performance studies, including calibration of the jet energy scale (JES) using charged particle quantities [35] and calibration of the jet mass in large-radius jets (see Chapter 10). These uncertainties can also directly affect analyses, which is discussed in the context of this thesis in Section 11.6.

Previous studies showed that the leading source of uncertainty was the track reconstruction efficiency in dense environments [48]. As described in Section 5, updates to the track reconstruction setup significantly improved its efficiency. Still, residual inefficiencies exist (see Section 6).

This chapter presents a novel data-driven method which uses the measure of ionization energy loss (dE/dx) provided by the pixel detector to quantify this track reconstruction inefficiency. Using the fact that a single charged particle produced in collisions at the LHC is expected to be a minimum ionizing particle (MIP), one can use the dE/dx in pixel clusters to distinguish clusters created by one or two MIPs. This can be used to identify the residual inefficiencies by asking how often are there two reconstructed tracks associated to a cluster from two particles. By comparing the measured inefficiency in data and MC, the respective uncertainty on the track reconstruction efficiency can be estimated.

As the previous chapters have shown, tracks have the highest collimation closest to the interaction point. Therefore the probability of finding a merged cluster is greater for the inner layers of the pixel detector. Clusters on the IBL cannot be used for this study since it does not measure dE/dx with sufficient resolution. Again, this is a result of its 4-bit ToT resolution, compared to eight bits used for the remaining pixel layers. As a result, this study uses information from clusters on the B-layer.

9.1 METHOD

The reconstruction and calibration of the $R = 0.4$ jets used in this study are described in Section 6.1. The same data set and simulated samples as described in Chapter 7 are used.

Reconstructed tracks must fulfill the following requirements:

- exactly one pixel cluster per layer
- $p_T > 10$ GeV
- $|\eta| < 1.2$
- $|d_0^{\text{BL}}| < 1.5$ mm
- $|z_0^{\text{BL}} \sin \theta| < 1.5$ mm

- number of SCT clusters ≥ 6

where d_0^{BL} is the transverse impact parameter calculated with respect to the measured beam line position, z_0^{BL} is the difference between the longitudinal position of the track along the beam line at the point where d_0^{BL} is measured and the longitudinal position of the primary vertex, and θ is the polar angle of the track. These stringent requirements select topologies with enhanced contributions of high quality collimated tracks, with negligible contributions from fake tracks.

Using data alone, this method shall quantify residual inefficiencies of the track reconstruction in the core of jets. To achieve this, three distinct distributions of cluster dE/dx are created through the selections outlined in Figure 35.

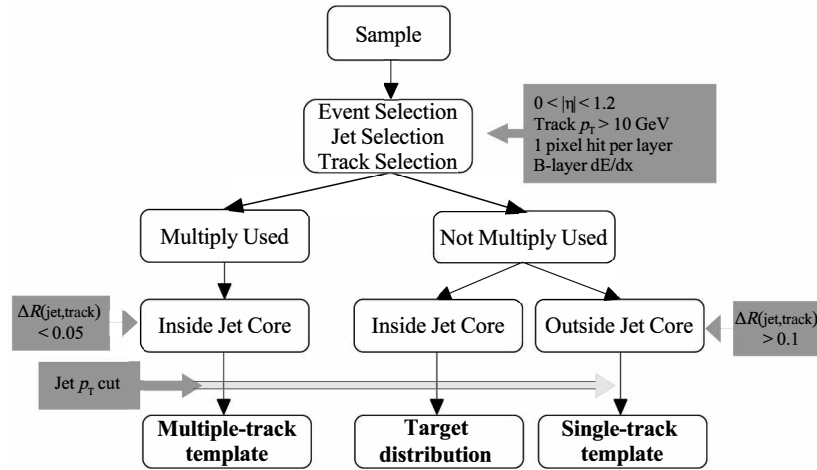


Figure 35: Selection chart for the three distinct dE/dx distributions used in the analysis.

One of them represents the dE/dx distribution of clusters from one MIP. This is achieved by selecting tracks which are outside the core of the jet ($\Delta R(\text{jet}, \text{track}) > 0.1$) and which use a cluster in the B-layer which is not used on any other track. For such tracks it is very likely that their clusters are created by one single particle and are labeled *Not-Multiply-Used* in the following. The second dE/dx distribution is built from tracks which are inside the core of the jet ($\Delta R(\text{jet}, \text{track}) < 0.05$) and which contain a cluster in the B-layer which is also used by another track. These clusters have a high probability to be created by more than one particle, i.e. to be merged clusters, and are further defined as *Multiply-Used*.

Figure 36 shows the two dE/dx distributions. The Not-Multiply-Used distribution, plotted as blue circles, exhibits a single peak at the dE/dx value expected for a MIP. The Multiply-Used distribution, plotted as green squares, instead peaks at a dE/dx value expected for two MIPs. At $dE/dx > 3.2 \text{ MeVg}^{-1} \text{ cm}^2$ one can also identify further peaks, which corresponds to B-layer clusters created by more than two charged particles. Such Multiply-Used clusters are still possible as was explained in Section 4.3.

The final distribution, the so called *target* distribution, is created from tracks inside the core of the jet ($\Delta R(\text{jet}, \text{track}) < 0.05$), which have a B-layer cluster which is only associated to one track. This subset of pixel clusters has two major populations, one consisting of clusters created by exactly one particle and correctly assigned to exactly

one track, and one of merged clusters created by multiple particles, which are only assigned to one track due to track reconstruction inefficiencies. Using the first two dE/dx distributions of Not-Multiply-Used and Multiply-Used clusters as templates, one can fit the target distribution to resolve the fractions of the two populations. With the resulting fitted fraction of merged clusters, F^{merged} , with only one track associated to them, one can set an upper limit on the fraction of unreconstructed particles which have created merged clusters:

$$F^{\text{lost}} = \frac{N_{\text{Lost}}}{N_2^{\text{True}}} = \frac{N_{\text{Lost}}}{N_2^{\text{Reco}} + 2 \cdot N_{\text{Lost}}}, \quad N_{\text{Lost}} = F^{\text{merged}} \cdot N_{\text{Data}}^{\text{Reco}}, \quad (5)$$

where N_{Lost} is the number of lost tracks, N_2^{True} is the true number of tracks that should be associated to a merged B-layer cluster from two particles, N_2^{Reco} is the number of reconstructed tracks inside the multiple-track template and $N_{\text{Data}}^{\text{Reco}}$ the number of reconstructed tracks in the target distribution. In the denominator, the number of lost tracks needs to be counted twice, since for every measured lost track two tracks are missing from the multiple-track template. The second equality is only strictly true if the assumption that lost tracks have the same properties as reconstructed tracks holds, which is known to be true from simulation. In other words, the number of tracks associated to a cluster created by two charged particles which would fail the track selection is negligible.

Since the peak in the dE/dx distribution from two MIPs for Multiply-Used clusters is by far the most prominent and clean, the fit is performed only between 1.1-3.07 (1.26-3.2) $\text{MeVg}^{-1}\text{cm}^2$ for data (simulation) to suppress contributions from higher dE/dx values. A imperfect description of the leading edge of the target distribution by the single-track-template would affect the fitted result. Since the area of interest lies at much higher dE/dx values, the lower edge of the fit range was chosen to avoid as much as possible the leading edge of the one particle dE/dx peak, while retaining high statistics for the remainder of the distribution. Simulation-based studies showed that no significant bias of F^{lost} is induced due to the choice of fit range, i.e. the true value of F^{lost} for tracks from clusters from the restricted and the inclusive range are comparable.

F^{lost} measures possible inefficiencies for tracks from particles using merged clusters from exactly two particles. The fit range is adjusted in simulation in order to have the same fraction of clusters as in the target distribution, which are inside the fitted range with respect to the total number of clusters. This is necessary since the calibrated response of the pixel sensors to a specific energy deposit has certain imperfections which results in a shift of the overall dE/dx distribution.

The used fitter fits an input data histogram (d) with two templates (T_1 and T_2) using a standard binned log likelihood fit and two fit parameters (n and F^{merged}) with the function:

$$f(x, F^{\text{merged}}, n) = n \times [(1 - F^{\text{merged}}) \times T_1(x) + F^{\text{merged}} \times T_2(x)] \quad (6)$$

where $T_{1/2}(x)$ is the number of entries in the template 1 and 2 in bin x , n is a floating normalization factor and F^{merged} is the fit parameter for the fraction of template T_2 (Multiply-Used template) entries in the data in bin x . For each bin x in the fit range

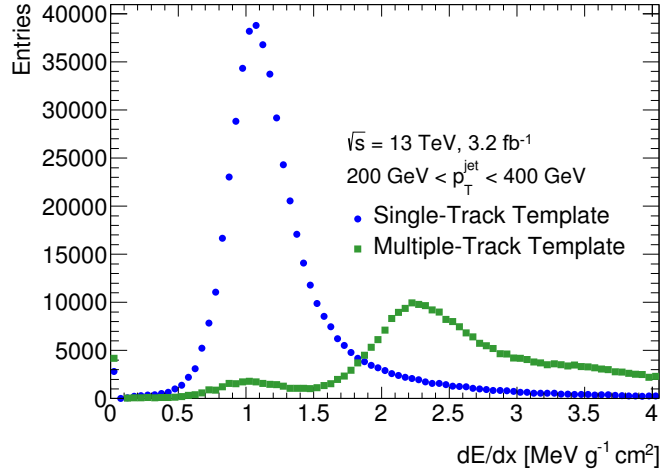


Figure 36: dE/dx distributions of the single- and multiple-track templates for data with a jet p_T in the range $200 \text{ GeV} < p_T^{\text{jet}} < 400 \text{ GeV}$.

the compatibility of the observed data with the fit model prediction is computed using a Poisson likelihood. The best set of parameters is found by minimizing the negative logarithm of the product of the Poisson likelihood over all bins in the fit range:

$$\sum_x d(x) \times \log f(x, F^{\text{merged}}, n) - f(x, F^{\text{merged}}, n) \quad (7)$$

Studies on the single ρ sample, also used in Chapter 5, show that the dE/dx distribution obtained by the selections applied to the target distribution is consistent with selecting potentially lost tracks. This reinforces the assumption that the fitted fraction F^{merged} corresponds to the fraction of lost tracks. For a single ρ decaying into two pions, two distinct event topologies can be observed. Firstly, the number of reconstructed tracks can match the number of reconstructed pseudo-tracks, and secondly, only one track can be reconstructed while two pseudo-tracks exist.

Figure 37 shows the dE/dx distributions for the two cases, where the distribution with one reconstructed track but two pseudo-tracks represents the dE/dx distribution when one track of a pair of collimated tracks is lost. For this distribution, the dominating second peak is due to the merged pixel clusters. The peak at a dE/dx of one MIP corresponds to tracks lost due to other effects than merging of the B-layer cluster. To check if the selections applied to obtain the Multiply-Used template really correspond to this distribution of lost tracks, the same selections are applied to this sample. The result can be seen in Figure 38, where the Multiply-Used template matches the distribution observed for lost tracks.

The jet p_T is directly related to the density of the environment and the frequency of merged clusters, and therefore expected to change the fraction of charged particles which might not be reconstructed into a track due to potential inefficiencies. For this reason the study is performed in jet p_T bins of 200 GeV ranging from 200 GeV to 1600 GeV. For simulation, jet p_T bin dependent templates are used. In the highest jet p_T bins in data, statistics is low. To not impair the fit quality due to the low statistics, the single-track and multiple-track templates obtained from the 200-400 GeV bin are

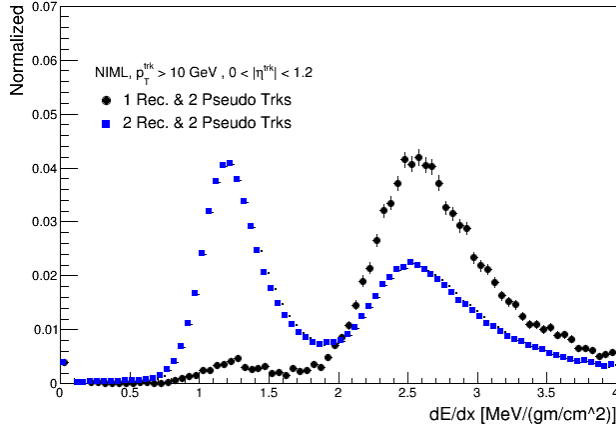


Figure 37: dE/dx distributions for two possible event topologies in the single ρ MC sample. The first topology with one reconstructed track but two pseudo-tracks represents the dE/dx distribution when one track of a pair of collimated tracks is lost. The second topology corresponds to the case where both tracks are reconstructed.

used to fit all jet p_T bins in data. Within the statistical uncertainty, these templates have the same shape as the ones at higher jet p_T within the fit range.

9.2 SYSTEMATIC UNCERTAINTIES

Two different groups of systematic uncertainties need to be considered. The first are uncertainties originating from the methodology described in Section 9.1. The second group arises from differences in the physics modeling between several MC event generators, and only affect the final data and MC comparison.

9.2.1 Uncertainties Related to the Method

Clusters created by more than two particles have a non-negligible contribution to the target dE/dx distribution. The choice of fit range, especially the upper bound, is expected to affect F^{lost} , the measured fraction of merged clusters associated to only one track. This effect is studied by increasing the fit range at higher dE/dx above the baseline selection. With each increment of $0.2 \text{ MeVg}^{-1}\text{cm}^2$, the relative increase in F^{lost} is about 5%. The maximum change in F^{lost} for each bin of jet p_T is added as a symmetrized uncertainty in that bin.

Due to the fitting of data in all jet p_T bins with templates from the lowest jet p_T bin, an additional systematic uncertainty is introduced. From studies on MC simulation, this procedure is known to introduce a small systematic bias in the fitted F^{merged} . This is caused by the varying contamination from clusters created by more than two particles in the multiple-track template with jet p_T , which varies between 3% and 8%. A jet p_T dependent correction factor is therefore applied to the result in data and an uncertainty on the order of the difference observed in simulation is assigned.

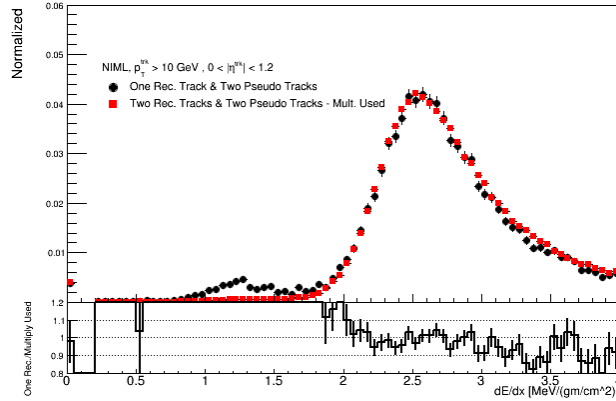


Figure 38: Distributions of dE/dx for events in the single ρ MC sample where only one track of the decay products of the ρ is reconstructed, but both are expected to be, compared to dE/dx distribution obtained in the Multiply-Used template.

Another possible source of uncertainty are possible contributions to F^{lost} not originating from the density of the environment. Such contributions could come from pile-up tracks creating merged clusters with tracks in the jets, as well as isolated track being lost. Conservative estimates based on truth-level studies on MC simulation showed that such contributions are on the order of 2% to 6% of the total F^{merged} in the studied jet p_T range, so much smaller as the other systematic uncertainties, and therefore are not considered explicitly in the final results. However, residual non-closure is considered inclusively.

A truth-based closure test was performed on simulated samples to validate the method for any missed systematic bias or contribution. It was found that in the lowest jet p_T bin, a significant non-closure is observed of the order of 21% - this corresponds to an absolute difference in the measured F^{lost} of about 0.013. This non-closure quickly decreases in the higher jet p_T bins. The non-closure arises mainly from two sources: the residual dE/dx peak at values expected from one MIP in the multiple-track template, and large dE/dx values from more than two clusters. The former effect is more relevant at low jet p_T while the second effect becomes stronger at high jet p_T . The non-closure is added as an additional uncertainty in all jet p_T bins for both simulation and data. Table 1 lists the relative uncertainties on F^{lost} .

Uncertainties on the JES calibration or resolution have negligible impact on the analysis. No effects due to the choice of binning in the individual bins of jet p_T are expected since the bin size is much smaller than the dE/dx resolution. This was checked explicitly by varying the bin size around the default binning used in the analysis. All variations produce identical results to the nominal binning. All relative systematic uncertainties on F^{lost} are summarized in Table 1.

Table 1: Summary of the relative systematic uncertainties on the fraction of lost tracks (F^{lost}) in bins of jet p_T for data.

Jet p_T bin	Fit Range [%]	Low p_T Templates [%]	Non-closure [%]
200–400 GeV	15	0	21
400–600 GeV	13	8	12
600–800 GeV	12	14	7
800–1000 GeV	14	21	1
1000–1200 GeV	14	25	0
1200–1400 GeV	13	19	0
1400–1600 GeV	19	20	0

9.2.2 Generator Uncertainties

In order to study the overall agreement of MC simulation with data, one has to take differences between different simulated models into account. Generator dependent differences provide the dominant systematic uncertainty. Comparing the measured values of F^{merged} for samples generated with either PYTHIA 8, SHERPA [49] or Herwig++ [50] allows to estimate this uncertainty as is shown in Figure 39. The observed differences are most likely due to different modeling of the charged particle multiplicities and distributions inside jets. For each bin of jet p_T , the assigned uncertainty is the largest symmetrized difference between the fitted value of F^{merged} between either of the three generators. This results in relative uncertainties of F^{merged} between 4 and 34%. It is important to note that this uncertainty does not need to be considered if one only compares a specific simulated sample to data.

9.3 RESULTS

Target distributions for data, fitted with the Not-Multiply-Used and Multiply-Used templates, are shown in Figure 40 for two bins of jet p_T . The combinations of both templates are able to well describe the target distribution, since the ratio of the fitted function to the target distribution is consistent with unity.

Figure 41 shows that F^{lost} is slightly increasing with jet p_T and that simulation is able to describe the data. In the core of jets, the fraction of lost tracks ranges from $0.061 \pm 0.006(\text{stat.}) \pm 0.014(\text{syst.})$ to $0.093 \pm 0.017(\text{stat.}) \pm 0.021(\text{syst.})$ between a jet p_T of 200 to 400 GeV and 1400 to 1600 GeV, respectively. This increase is caused by increasingly boosted particles, which cause higher collimation of the track pair, and is not due to confusion in correctly assigning clusters to tracks. At a certain point, the two particles are so collimated that the reconstructed tracks start to overlap completely up to the radius of the SCT detector. At that point a similar effect as shown for tracks from the ρ decay in Figures 12 and 15 occurs. The cluster assignment efficiency for reconstructed tracks remains constant with increasing jet p_T , indicating no degradation

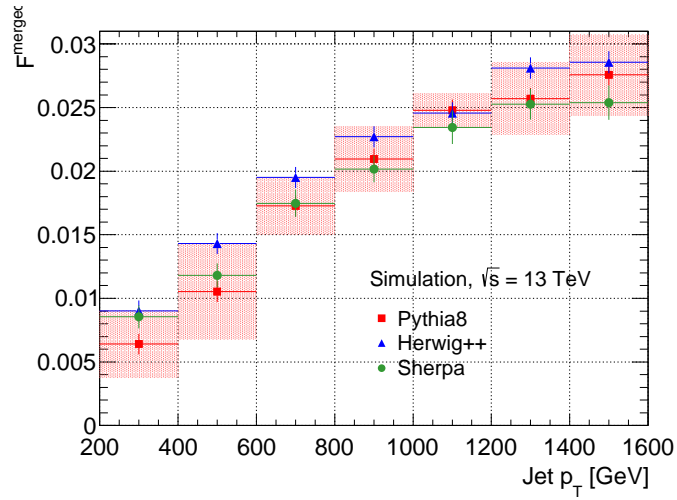
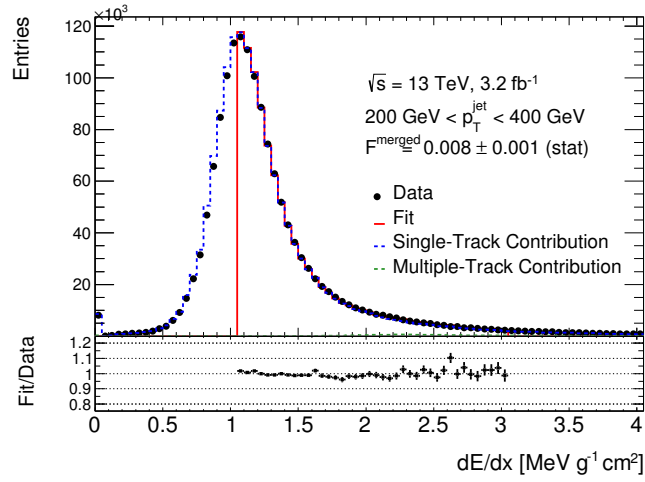


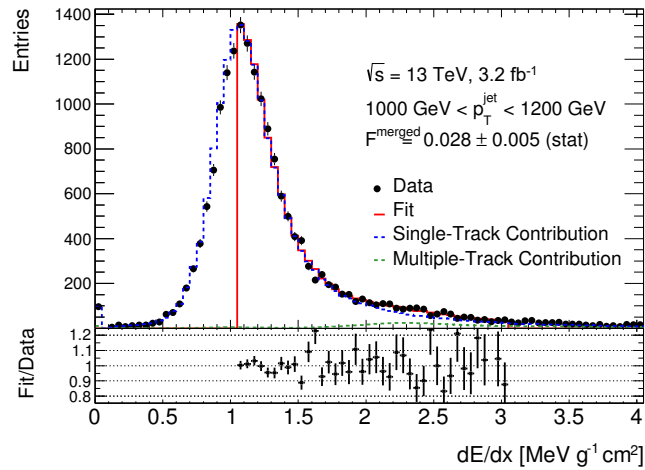
Figure 39: Comparison of the fitted fraction of merged clusters, F^{merged} , between Pythia8, Herwig++, and Sherpa as a function of jet p_T . Errors bars are purely statistical while the red error band for Pythia8 reflects the derived generator uncertainty.

of performance due to the environmental effects besides the second track. The probability of losing one of the tracks rises only because of their increasing collimation. This effect has been confirmed on simulation for tracks selected by this analysis.

Fitting a constant value to the ratio of F^{lost} shows that data and MC simulation are consistent across the whole studied jet p_T range.



(a)



(b)

Figure 40: Comparison of target dE/dx distributions with the fitted results for a jet p_T between (a) 200-400 GeV and (b) 1000-1200 GeV. The two template distributions scaled by their fitted fractions are also shown. The ratio between the fit and the target distribution is shown on the bottom within the fit range (1.1–3.07 $\text{MeVg}^{-1}\text{cm}^2$).

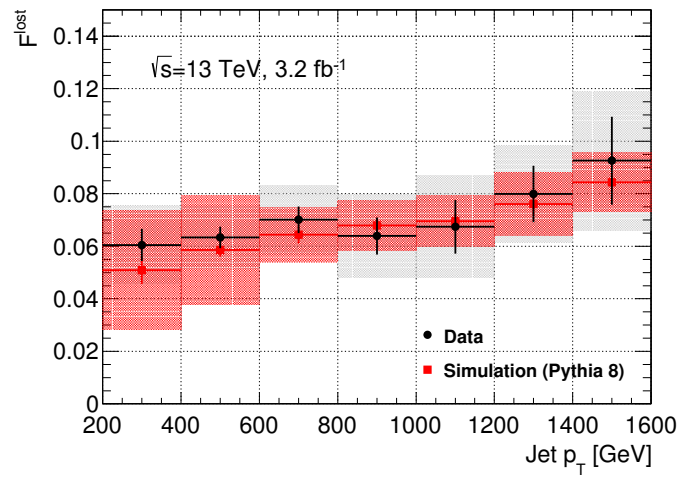


Figure 41: The measured fraction of lost tracks (F^{lost}) in the core of jets ($\Delta R(\text{jet}, \text{track}) < 0.05$) as a function of jet p_T for data and simulation. The gray (red) error bands indicate the total uncertainty, while the black (red) error bars show only the statistical uncertainty for data (simulation).

Part IV

JET MASS RECONSTRUCTION

Massive particles produced in the decay of TeV-scale resonances, such as W and Z bosons or top quarks, are highly boosted. As a result, their decay products become increasingly collimated as the mass of the resonance increase. In case they decay into quarks, they are reconstructed as a single large-radius jet. One of the strongest discriminants between these jets and the multijet background is their mass (*jet mass*). Improving the resolution (JMR) of the reconstructed jet mass and reducing related uncertainties is therefore essential.

This part of the thesis introduces the different approaches to jet mass reconstruction used in ATLAS. Most of the content in this chapter has been previously presented in Reference [51] with significant contributions from the author of this thesis. Where not explicitly stated, all result in this thesis are based on the optimized track reconstruction setup discussed in detail in Part II. MC samples are used in this chapter to obtain the expected performance of multiple jet mass definitions, to perform the mass calibration, as well as for the derivation of related uncertainties. The same MC and data samples as described in Chapter 7 are used. In addition, simulated samples of W' boson (Z' boson) event provide a rich source for boosted W/Z bosons and top quarks. They are simulated with the same event generator (PYTHIA), the same PDF (NNPDF23LO) and tuned parameters (A14) as the dijet MC samples.

Two basic jet mass definitions, each with strength in specific kinematic regimes, and a method to combine the two are presented. Built solely from calorimeter information, the *calorimeter-based* jet mass serves as the baseline mass definition. This mass definition can be expanded, using the higher granularity information available from the ID. This leads to the definition of the so called *track-assisted* jet mass. By combining these two variables, one can achieve the performant *combined* jet mass. Each of these jet mass definitions are described in more detail in Sections 10.1 and 10.5. After introducing the various mass definitions, their resolutions are compared in simulation in Section 10.3 and corresponding systematic uncertainties are discussed in Section 10.4.

10.1 JET MASS DEFINITIONS

The jet mass is mainly used as a variable to identify jets originating from boosted particles. For these topologies large-radius jets are used and the following results are presented for such jets. However, the general mass definitions provided below, as well as their calibration procedures, are also valid for small-radius jets.

The classical jet mass definition within ATLAS is the calorimeter-based jet mass (m^{calo}). For a calorimeter jet J composed of calorimeter-cell clusters i with energy E_i , momentum \vec{p}_i ($|\vec{p}_i| = E_i$) it is defined as:

$$m^{\text{calo}} = \sqrt{\left(\sum_{i \in J} E_i\right)^2 - \left(\sum_{i \in J} \vec{p}_i\right)^2}. \quad (8)$$

Since this jet mass depends on both angular (used to build \vec{p}_i) and energy information, the resolution of both individual measurements will determine the resolution of the mass. As described in Section 3.5, the calorimeters offer excellent energy resolution. However, the spatial granularity, which determines the angular resolution, can become a limiting factor for very collimated streams of particles. For a sufficiently high Lorentz boost of the parent particle, the spatial separation of its decay products is so small that their spatial separation reaches the calorimeter granularity. In the limit of a jet reconstructed from a single calorimeter-cell cluster, the jet mass following the classical definition above becomes zero.

As a way out, high resolution angular information from the tracking detectors can be used to complement the calorimeter measurements. Similar approaches have previously shown to provide superior performance, for example in particle-flow [52].

There have been previous attempts to improve the reconstructed jet mass, the first of which extended the electromagnetic calorimeter measurement by using the hadronic information [53, 54]. In the context of tagging jets originating from a top quark, information from the tracker was used for the first time to complement the calorimeter measurement of the mass [55]. Phenomenological studies for future colliders discussed a track-assisted mass in connection with highly boosted ($p_T \gtrsim \mathcal{O}(10)$ TeV) jets from bosons and top quarks [56, 57].

Information from the tracker and the calorimeter can be combined into the track-assisted jet mass (m^{TA}):

$$m^{\text{TA}} = \frac{p_T^{\text{calo}}}{p_T^{\text{track}}} \times m^{\text{track}}, \quad (9)$$

where p_T^{calo} is the transverse momentum of a calorimeter jet, p_T^{track} is the transverse momentum of the sum of all tracks' four-vectors associated to the jet, and m^{track} is the invariant mass of this sum. For a single reconstructed track the mass is set to m_π , a good approximation since $p_T^{\text{track}} \gg m_\pi$. The ratio of the transverse momenta $p_T^{\text{calo}}/p_T^{\text{track}}$ corrects for the component from neutral particles, which the ID cannot reconstruct, and which is missing in p_T^{track} . This minimizes the effect of charged-to-neutral fluctuations, and improves the resolution with respect to a track-only jet mass definition (m^{track}). Figure 42 compares the uncalibrated calorimeter-based jet mass (dashed red line) to the uncalibrated track-assisted jet mass (dashed black line), and shows that the latter is superior in resolution with respect to the uncalibrated track-only jet mass (dashed blue line) for jets with $1.6 \text{ TeV} < p_T < 1.8 \text{ TeV}$.

Besides the charged-to-neutral fluctuations, the resolution and purity of the subset of tracks selected as input to the track-assisted mass limits its resolution. By replacing

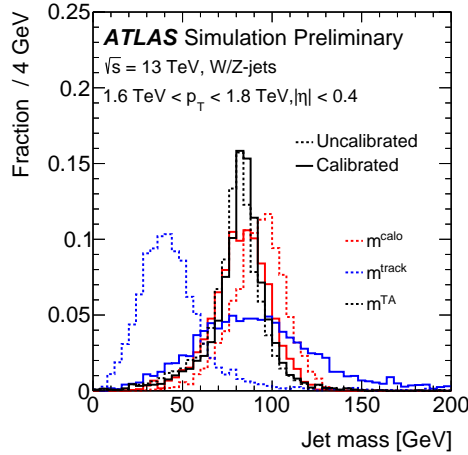


Figure 42: Reconstructed jet mass distributions for calorimeter-based jet mass, m^{calo} , track-assisted jet mass m^{TA} and the track-only jet mass m^{track} for W/Z -jets. Each mass is shown before and after calibration.

the reconstructed tracks directly with the charged particles associated to the truth jet matched to the calo jet, one can estimate the ultimate possible performance of this method using MC simulation. As shown in Figure 43, the resolution would be improved by a factor of two, if the efficiency to reconstruct all tracks would be 100%, their resolution zero, as well as the assignment of the tracks to the reconstructed jet would be perfect.

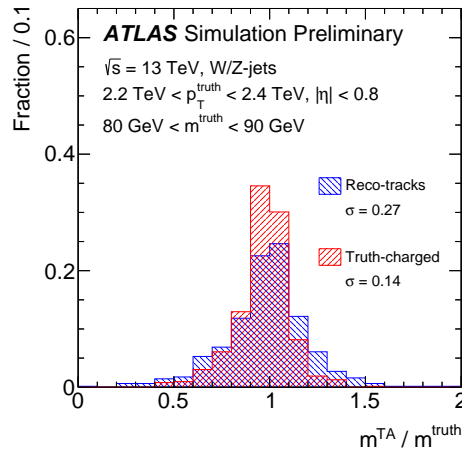


Figure 43: Response distribution of m^{TA} built from reconstructed tracks is shown in blue while the red distribution uses charged truth particles with $c\tau > 30 \text{ ps}$ (excluding muons) as input. Jets are restricted to $2.2 \text{ TeV} < p_T < 2.4 \text{ TeV}$ and $80 \text{ GeV} < m^{\text{truth}} < 90 \text{ GeV}$

10.2 JET MASS CALIBRATION

Analogously to the calibration applied to correct the JES [35, 37, 38], also the jet mass scale (JMS) needs to be calibrated. The goal of this calibration is to correct the reconstructed jet mass on average to the mass of the jet on truth-particle-level.

The mass response for a given jet mass is defined as the ratio between the reconstructed jet mass and the mass of the matched truth-level jet:

$$\mathcal{R}_m = m^{\text{reco}} / m^{\text{truth}}; \quad m^{\text{reco}} \in c^{\text{JES}} \cdot m^{\text{calo}}, c^{\text{JES}} \cdot m^{\text{TA}}, \quad (10)$$

where c^{JES} is the E^{reco} and η_{det} dependent JES calibration factor - hence the mass calibration is performed with the JES calibration already applied.

The jet mass calibration factors are determined by the mean of a Gaussian fit to the average response $\langle \mathcal{R}_m \rangle$ in bins of p_T^{truth} , $|\eta_{\text{det}}|$, m^{truth} . This calibration is performed in a sample of QCD dijet MC by matching isolated large-radius jets to isolated truth-level jets. Isolation requires no other jet within $\Delta R = 1.5$ (2.5) for the reconstructed (truth) jet. The truth-level jet is matched if its $p_T > 100$ GeV and it is within $\Delta R < 0.6$ of the reconstructed jet. To transform the dependence of this calibration from truth based values to reconstructed jet quantities, a numerical inversion is performed [51]. The average jet mass response is said to be calibrated if $\langle \mathcal{R} \rangle = 1$.

Although the JES calibration partially corrects for η dependent detector effects, a full jet mass calibration is still required. Figure 44 shows the average response versus p_T^{truth} after energy, but before mass calibration. A much more uniform response before mass calibration for m^{TA} is observed compared to m^{calo} , since p_T^{calo} in Equation 9 is already calibrated.

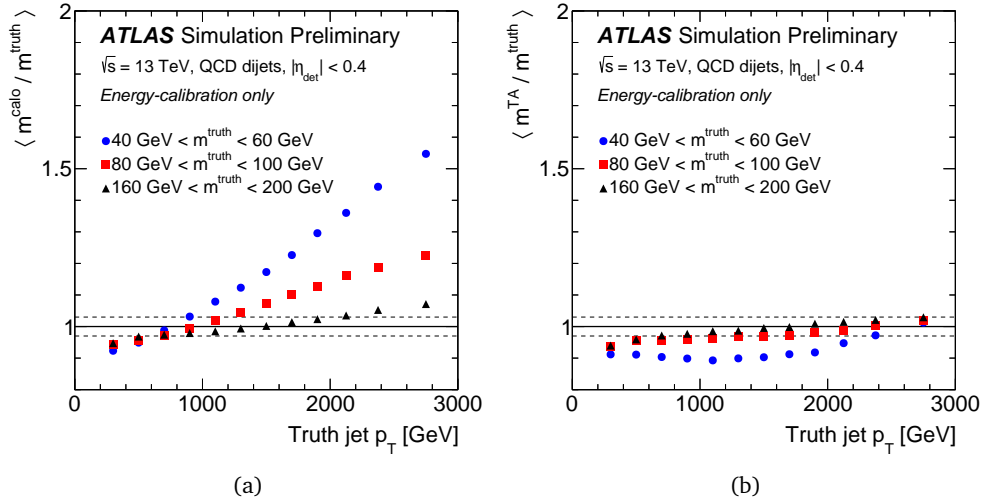


Figure 44: Average jet mass response of (a) m^{calo} and (b) m^{TA} as a function of p_T^{truth} for central jets in dijet MC shown in three bins of m^{truth} after energy but before mass calibration.

As shown in Figure 45, after calibration the m^{calo} and the m^{TA} have a uniform jet mass response within 3% across all bins of p_T^{truth} , m^{truth} and $|\eta_{\text{det}}|$. For low m^{truth} and high p_T^{truth} the calibration of the calorimeter-based mass fails to achieve perfect closure. Due to the high gradient of the response of m^{calo} in this region, two jets on the high and low edges of the same m^{truth} bin can receive very different corrections. In combination with the poor jet mass resolution (JMR) in this region, two populations of jets will exist: those with a higher mass where a calibration factor close to one is applied, and

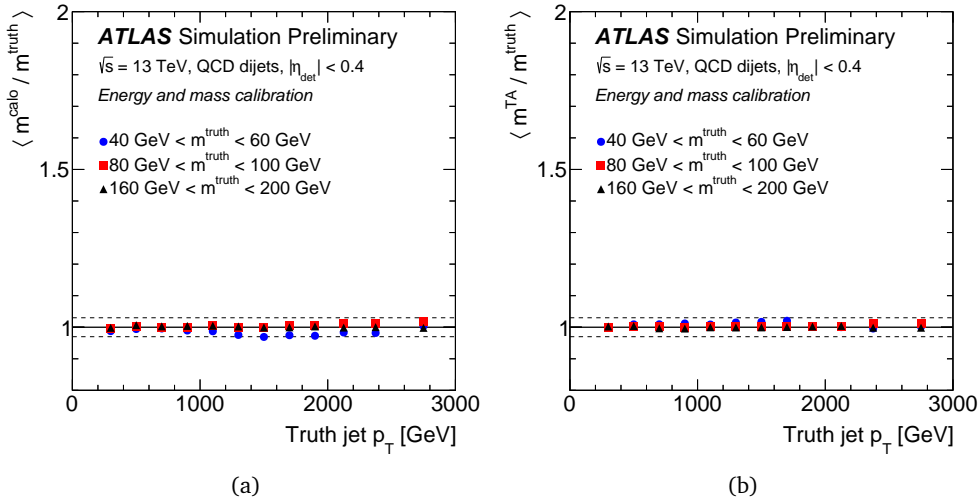


Figure 45: Average jet mass response of (a) m^{calo} and (b) m^{TA} as a function of p_T^{truth} for central jets in dijet MC shown in three bins of m^{truth} after energy and mass calibration.

those with lower mass where a large correction is applied (calibration factor $\ll 1$). This is illustrated by Figure 46 (a). For the remainder of the calibrated phase space, closure is observed after correcting the jet mass for both mass definitions, as is shown for an example bin in Figure 46 (b).

10.3 JET MASS PERFORMANCE IN SIMULATION

Figure 47 shows the resolution of the jet mass response as a function of truth jet p_T for jets originating from boosted W and Z bosons as well as top quarks. There are several possibilities for quantifying the resolution of the response distribution. Using half of the 68% interquantile range (IQNR)¹ divided by the median has proved to be a robust measure for this quantity, which is insensitive to outliers. In the limit of a Gaussian distribution this quantity equals the standard deviation. Both the calorimeter-based and track-assisted JMR degrade at high p_T , as shown in Figure 47; for the calorimeter-based mass this is due to finite granularity discussed in Section 10.1 and for the track-assisted mass it is mainly due to a worsening track resolution.

For jets initiated by W or Z bosons the m^{TA} provides superior resolution compared to the m^{calo} above 1 TeV. At lower momentum the charged-to-neutral fluctuations significantly limit the resolution of the m^{TA} so the m^{calo} provides the better performance. For different reasons the m^{TA} is unable to match the performance of the m^{calo} for top jets in the studied phase space. Since the mass of the top is higher than the W and Z boson, a greater p_T is needed to achieve the same collimation of its decay products. At sufficiently high p_T a cross-over point where the m^{TA} is superior to the m^{calo} is still expected. In addition, top jets on average exhibit a higher number of subjets than jets from W or Z bosons, which again reduces the density of the environment and therefore the granularity of the detector needed to resolve it.

¹ This is defined as $q_{84\%} - q_{16\%}$, whereby $q_{16\%}$ and $q_{84\%}$ are the 16th and 84th percentiles of a given distribution.

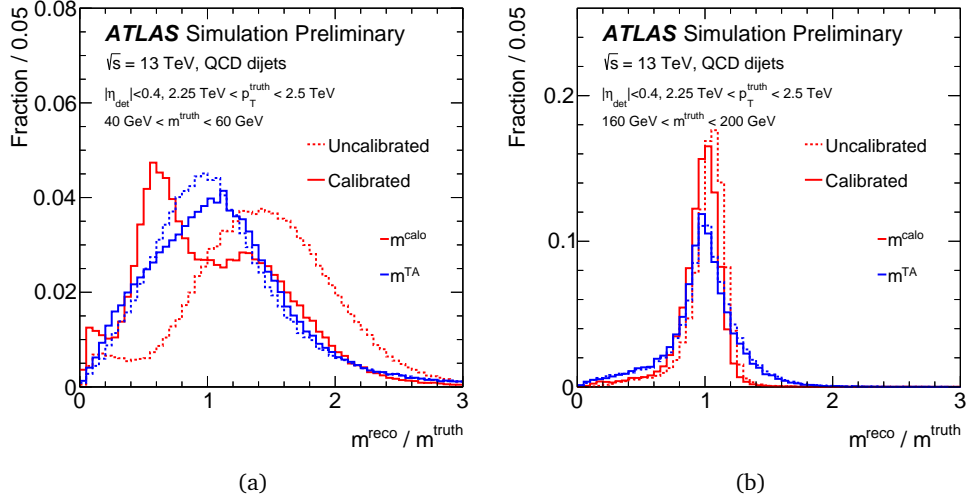


Figure 46: Jet mass response distribution for m^{calo} and m^{TA} for central jets in dijet MC with $2.25 \text{ TeV} < p_T^{\text{truth}} < 2.5 \text{ TeV}$ before and after the mass calibration is applied. Two bins of m^{truth} are shown: (a) $40 \text{ GeV} < m^{\text{truth}} < 60 \text{ GeV}$ and (b) $160 \text{ GeV} < m^{\text{truth}} < 200 \text{ GeV}$

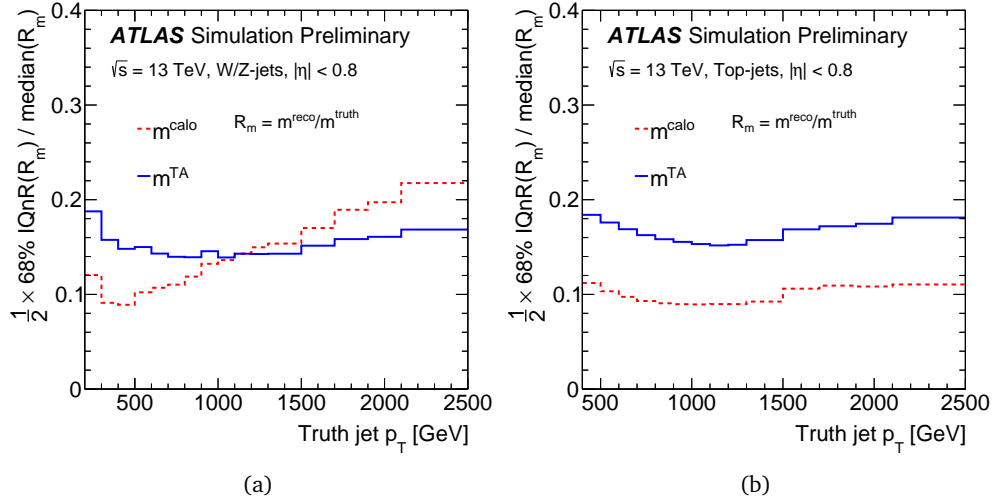


Figure 47: Resolution of m^{calo} and m^{TA} for central (a) W/Z-jets and (b) top-jets in MC as a function of p_T^{truth} . The resolution is defined as half of the 68% interquartile range (IQnR) divided by the median of the distribution.

10.4 JET MASS SYSTEMATIC UNCERTAINTIES

The JMS cannot be obtained from data by methods such as jet balancing, since the partonic center of mass energy is unknown at the LHC. One alternative method for probing the JMS in data involves the use of r_{track}^m , defined as the ratio between m^{calo} and m^{track} , for QCD dijet events [38]. This quantity is proportional to the JMS under the assumption that it can be decomposed into

$$r_{\text{track}}^m = \mathcal{R} \times (m^{\text{truth}} / m^{\text{charged truth}}) \times (m^{\text{charged truth}} / m^{\text{track}}). \quad (11)$$

A residual dependence of the calorimeter response on charged-to-neutral fluctuations makes this factorization only approximately true. As a result, $1 - \langle r_{\text{track}}^m \rangle_{\text{Data}} / \langle r_{\text{track}}^m \rangle_{\text{MC}}$ provides an upper limit on the scale uncertainty. Uncertainties on the fragmentation modeling, as well as the track reconstruction performance can affect the double ratio and as consequence limit the precision of this method to $\sim 5\%$. The method cannot be used to determine the JMR because the resolution of the track term is dominated by charged-to-neutral fluctuations. In the case of m^{TA} , both the uncertainties on the track reconstruction and the calorimeter-jet p_T are known, so the systematic uncertainties on both its JMS and JMR can be evaluated directly by propagating the uncertainty on the individual components. This is one of the key advantages of the track-assisted mass compared to the calorimeter-based mass and the uncertainties on the individual components are derived as explained below.

The material in the ID is not precisely known. Since hadronic interactions with its material are the main source of track reconstruction inefficiencies for isolated particles, the introduced uncertainty is evaluated by varying the amount of material within its measured uncertainty [58]. As extensively discussed in the previous chapters, a residual track reconstruction inefficiency in the core of highly energetic jets exists and the uncertainties on it are derived as described in Chapter 9. Fake track provide the second biggest source of uncertainty on the reconstruction. Using the assumption that the number of reconstructed tracks is expected to increase linear with pile-up, one can estimate the number of fake tracks by measuring any deviation from this non-linearity. By comparing this non-linearity in data and MC, one obtains a 30% uncertainty on the fake rate [59]. A possible uncertainty due to a bias in the reconstructed momentum of the tracks can be assessed using $Z \rightarrow \mu\mu$ events, where the momentum is reconstructed iteratively to obtain the mass of the Z boson [60] (as defined by the particle data group [2]). As already mentioned in Section 9.2.2, the fragmentation modeling differs between different event generators, which leads to differences in the track reconstruction performance. Such differences can lead to changes in m^{TA} and their magnitude is estimated by comparing PYTHIA 8 and HERWIG++. The calorimeter-jet p_T uncertainty is estimated in analogue with the calorimeter based-mass: $r_{\text{track}}^{p_T} = p_T^{\text{calo}} / p_T^{\text{track}}$.

The individual components of the JMS uncertainties for both m^{TA} and m^{calo} are shown in Figure 48. Full correlation is assumed between the track reconstruction uncertainties on m^{TA} and m^{calo} , since for both quantities a variant of the r_{track} method is used to estimate parts of the uncertainty. m^{TA} is built through $m^{\text{track}} / p_T^{\text{track}}$ so the overall uncertainty on the JMS due to track reconstruction uncertainties is much smaller as they cancel out in the ratio. In the region of $p_T = 300 - 1000$ GeV, the uncertainty is about 4% for m^{calo} and about 2% for m^{TA} . At higher p_T , the uncertainty is limited

for both mass definitions by the statistics available in the data set, which limits the precision of the r_{track} measurement.

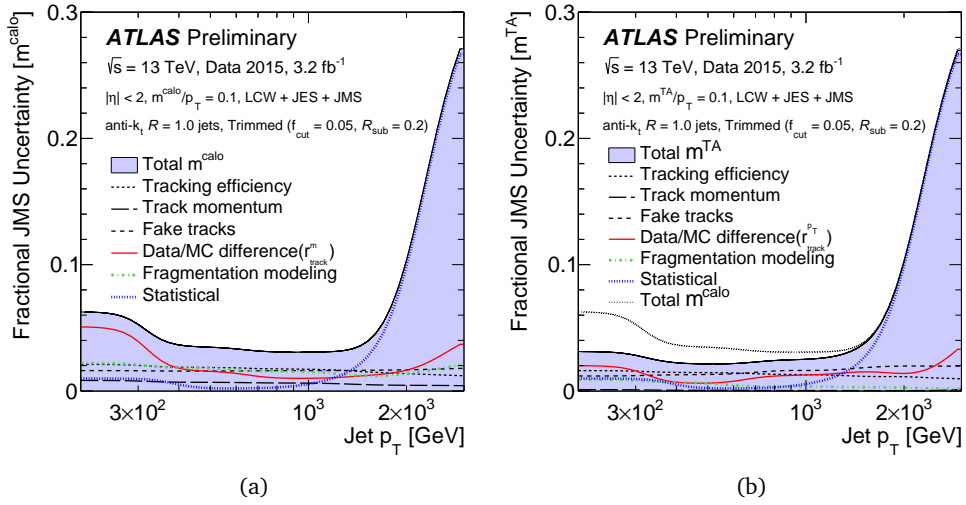


Figure 48: Fractional JMS uncertainty and its individual components for (a) m^{calo} and (b) m^{TA} as function of p_T^{truth} for $m^{\text{reco}}/p_T = 0.1$ and $|\eta| < 2$.

10.5 COMBINATION OF m^{TA} AND m^{calo}

The calorimeter-based jet mass is not explicitly used in deriving the track-assisted jet mass and as Figure 49 shows, the correlation between the two masses is indeed very small.

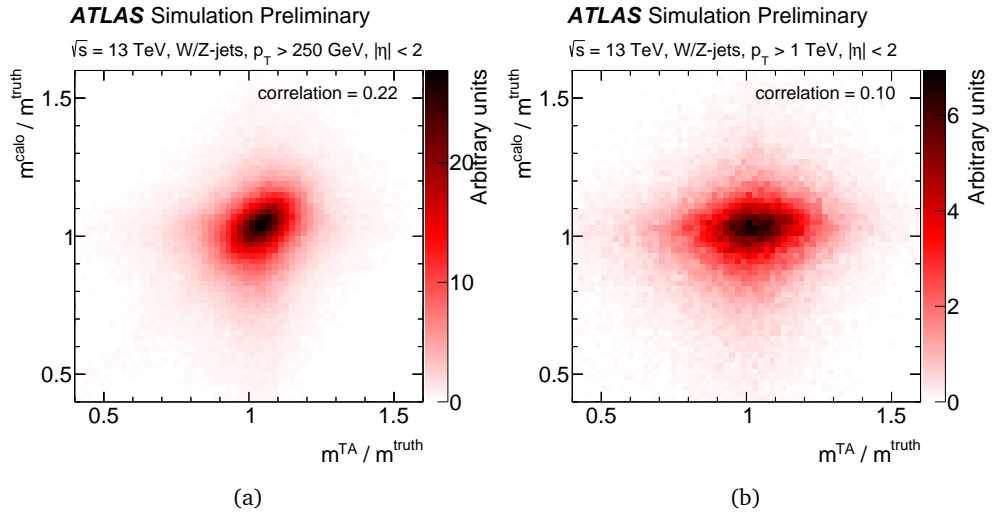


Figure 49: Correlation between the mass responses of m^{calo} and m^{TA} for W/Z-jets in MC with $|\eta| < 2$ and (a) $p_T > 250$ GeV and (b) $p_T > 1$ TeV.

For jets with $p_T > 1$ TeV the correlation coefficient is just 0.1. Both m^{calo} and m^{TA} are influenced by local fluctuations in the energy response of the calorimeter, but the im-

fact on p_T^{calo} is much smaller. Motivated by this fact, a combination of the two masses, the so called combined jet mass, can potentially provide a more powerful mass definition. Under the assumption that both individual jet mass responses are Gaussian, the combined jet mass is given by a linear combination $m^{\text{comb}} = a \times m^{\text{calo}} + b \times m^{\text{TA}}$. Further, since both individual jet masses are already calibrated, also m^{comb} is calibrated by requiring $a + b = 1$. Considering these two facts, choosing weights which are proportional to the individual mass resolutions is an appropriate choice for the combination:

$$a = \frac{\sigma_{\text{calo}}^{-2}}{\sigma_{\text{calo}}^{-2} + \sigma_{\text{TA}}^{-2}} \quad b = \frac{\sigma_{\text{TA}}^{-2}}{\sigma_{\text{calo}}^{-2} + \sigma_{\text{TA}}^{-2}} \quad (12)$$

In Equation 12, σ_{calo} and σ_{TA} are the calorimeter-based and track-assisted mass resolutions respectively. The resolution of all three mass definitions is compared in Figure 50 for W and Z -jets in MC as a function of the p_T of the truth jet. At low p_T $m^{\text{comb}} \sim m^{\text{calo}}$ and at higher p_T $m^{\text{comb}} \sim m^{\text{TA}}$ with a smooth interpolation in the intermediate phase space. There is a non-trivial increase in resolution of the intermediate jet p_T range, and the combined JMR is always superior to the individual jet masses.

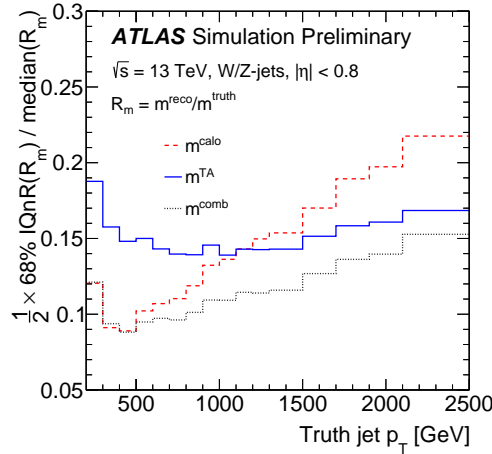


Figure 50: Resolution of m^{calo} , m^{TA} and m^{comb} for central W/Z -jets in MC as a function of p_T^{truth} . The resolution is defined as half of the 68% interquantile range (IQnR) divided by the median of the distribution.

Systematic uncertainties on m^{comb} are obtained by propagating the individual uncertainties on m^{TA} and m^{calo} through Equation 12, while the contributions of the track reconstruction uncertainties need to be treated as fully correlated.

10.6 CONCLUSION

The jet mass is an invaluable tool in identifying the nature of large-radius jets. Several different options exist to build this mass purely from calorimeter information, from tracks of charged particles associated to the jet, or by combining all available information into a combined jet mass. A simulation based calibration procedure for the JMS is inevitable, and it is demonstrated that such a technique can provide closure. At high p_T the track-assisted mass outperforms the classical definition in topologies from hadronic

W/Z -boson decays in terms of both resolution and uncertainties, while providing no gain in resolution for top-jets. Combining the strengths of both the calorimeter-based and track-assisted mass into the combined mass provides the most performant reconstructed jet mass currently available.

Part V

SEARCH FOR RESONANCES WITH BOSON-TAGGED JETS

The increased data set of proton-proton collisions at the LHC at $\sqrt{s} = 13$ TeV offers an improvement in sensitivity to searches for new heavy objects with masses at the TeV-scale. Diboson resonances are predicted in several extensions to the SM, such as extended gauge symmetry models (EGM) [61–63], Grand Unified theories [64–67], theories with warped extra dimensions [68–72], two-Higgs-doublet models [73], little Higgs models [74], theories with new strong dynamics [75], including technicolour [76–78] and more generic composite Higgs models [79].

In this search, two specific benchmark models are used to optimize the event selection and as a result increase the sensitivity of the search. They are also used for comparison with the observed data. The first is the Heavy Vector Triplet Model (HVT) [80] which provides signals such as $W' \rightarrow WZ$ and $Z' \rightarrow WW$, and the second a model predicting a spin-2 graviton G_{RS} decaying into WW or ZZ pairs, described by Kaluza-Klein modes [68, 69] of the Randall-Sundrum (RS) graviton [70–72].

With the Run 1 data ATLAS excluded at the 95% confidence level (CL) the EGM $W' \rightarrow WZ$ with masses between 1.3 and 1.5 TeV. Upper limits were set on the production cross section times branching ratio for a G_{RS} of the RS model decaying to WW in the fully hadronic channel. The largest excess of events over the background was seen at 2.0 TeV in the WZ channel with a global significance of 2.5 standard deviations, taking the entire mass range of the search in all three channels into account [81]. CMS excluded in the fully hadronic channel the EGM W' with masses below 1.7 TeV, and G_{RS} with masses below 1.2 TeV, both at the 95% CL. The largest excess of events over the background was seen at 1.9 TeV with a global significance of 1.3 standard deviations [82]. Upper limits on the production of generic diboson resonances using semileptonic final states were also published by CMS [83]. Using dileptonic final states, ATLAS has excluded at 95% CL a bulk $G_{RS} \rightarrow ZZ$ with masses below 740 GeV [84]. For narrow resonances decaying exclusively to WZ or WW , the ATLAS search in the semileptonic channel excluded a G_{RS} with masses below 700 GeV [85].

Both collaborations have performed searches using the early Run 2 data at $\sqrt{s} = 13$ TeV collected in 2015. In the ATLAS results [86] several final states ($\ell\nu qq$, ℓlqq and $qqqq$) are combined to search for narrow-width resonances with mass between 500 and 3000 GeV. No significant deviations from the SM background predictions were observed. The data excludes at 95% CL a scalar singlet with mass below 2650 GeV, a HVT boson with mass below 2600 GeV, and a graviton with mass below 1100 GeV. Similar results from CMS [87] were presented, with no significant deviations above the SM predictions.

The analysis described in this chapter is a search for narrow diboson resonances (WW , WZ and ZZ) decaying into fully hadronic final states. This search is performed utilizing the combined jet mass introduced in Chapter 10, in contrast to previous results from ATLAS with the same data set [88] (with significant contributions from the author of this thesis). W and Z bosons produced in the decay of TeV-scale resonances

are highly boosted and their decay products become increasingly collimated as the mass of the resonance increases. In case they decay into quarks, they are reconstructed as a single large-radius jet. In consequence, the signature of such heavy resonance decays in this mode is a resonant structure in the dijet invariant mass spectrum. The dominant multijet background produces a smoothly falling invariant mass spectrum, lacking any resonant structures. A grooming-trimming procedure is performed on the jets used in the analysis to minimize the effects of pile-up. To distinguish the signal from the background, jets are selected as bosonic in character, using a tagging technique based on the mass of the jet and further substructure properties. This strongly suppresses the multijet background, while still keeping a smoothly falling invariant mass distribution. The contribution to background from processes containing bosons, as $V + \text{jets}$ (where V represents W or Z bosons), SM VV , $t\bar{t}$ and single top production, is significantly smaller than from the dominant multijet background. None of the backgrounds explored are expected to contain any resonant structures within the SM. Within the analysis, to avoid problems caused by the poorly modeled and low statistics backgrounds in MC samples, the expected background is modeled by a fit to the smoothly falling distribution in data.

11.1 DATA SAMPLE AND SIMULATED SAMPLES

11.1.1 Data Sample

This search is performed using data collected in 2015 and 2016 from $\sqrt{s} = 13$ TeV LHC pp collisions with 25 ns bunch crossing separation, using the lowest- E_T un-prescaled single large-radius jet trigger, jet $E_T \geq 360$ GeV in 2015 and $E_T \geq 420$ GeV in 2016.

For these runs the standard data quality requirements are applied to select the luminosity blocks where all sub-systems of the detector were fully operational, as well as limited periods where there was no toroidal magnetic field. The integrated luminosity after these selections is estimated following the methodology described in [89] and is 3.2 fb^{-1} in 2015 and 12.3 fb^{-1} in 2016. Incomplete events, as well as events flagged as being unusable for analysis in either the LAr or Tile calorimeters are removed.

11.1.2 Simulation of Signal and Background Events

Effects due to event pile-up are considered by overlaying additional minimum bias events simulated with PYTHIA 8. To reproduce the pile-up conditions in data, simulation is reweight to match the pile-up distribution observed in data.

11.1.3 Signal Samples

The HVT and Kaluza-Klein Graviton in RS warped extra dimensions models described below are used as benchmarks to optimize the analysis and ultimately set limits.

11.1.3.1 Heavy Vector Triplet Model

A generic parametrization of the couplings of a new HVT (W', Z') with the SM fields allows for many models to be described. The HVT phenomenological Lagrangian [80] introduces such a parametrization and allows for mixing of the SM vector bosons with the new triplet field. Defining g_V as a new parameter describing the coupling strength to the new bosons, the coupling between the SM fermions and the new triplet can be described as: $g^2 C_F / g_V$. Here, the gauge coupling of the SM $SU(2)_L$ is denominated as g , and C_F represents a multiplicative factor, modifying the coupling to SM fermions. Similarly, $g_V C_H$ describes their coupling to the Higgs boson, C_H again being a multiplicative modifier.

A specific model assuming $g_V = 1$ forming the HVT is investigated. In this scenario, the W' and Z' decay to SM particles, with a branching fraction to boson pairs (WZ , WW , WH and ZH) of approximately 2% and a decay width of approximately 2.5% in the studied mass range. The model creates the new triplet field by an extension of the SM gauge group and is characterized by a weak coupling to the SM fields. Table 2 lists cross sections, branching fractions and widths for selected HVT benchmarks.

Signal MC samples with masses between 1.0 and 3.0 TeV are generated using MADGRAPH 2.2.2 [90] interfaced to PYTHIA 8 for hadronization with the A14 tuned parameters and the NNPDF23LO PDF sets. The samples are in intervals of 100 GeV up to 2.0 TeV, then with intervals of 200 GeV up to 3.0 TeV. Only events are simulated where the new vector bosons decays into WW or WZ pairs which in turn decay hadronically. The root mean square (RMS) of the invariant mass of the decay products of the simulated HVT bosons is about 3.5% of the boson's pole mass.

11.1.3.2 Kaluza-Klein Graviton in Randall-Sundrum Bulk Warped Extra Dimensions

Another model considered is the so-called bulk RS model [70], an extension to the original RS model [68, 91]. Through the introduction of a warped extra dimension it allows the SM fields to propagate in the bulk of the extra dimension. The model has a dimensionless coupling constant, which can be described by the curvature of the warped extra dimension (k) and the reduced Plank mass (\overline{M}_{Pl}) as $k/\overline{M}_{\text{Pl}} \sim 1$. Decays of the Kaluza-Klein graviton, G_{RS} , into pairs of WW and ZZ bosons have a considerable branching fraction in this model. In the scope of this search, signals from the bulk RS model with $k/\overline{M}_{\text{Pl}} = 1$ and G_{RS} masses larger than 1 TeV are studied. In this model, the branching fraction of the G_{RS} decaying to a WW (ZZ) boson pair varies between 18.7% and 16% (9.5% and 8%) with the graviton pole mass, and its decay width is approximately 2.5% in the studied mass range Table 2 lists cross sections, branching fractions and widths for selected G_{RS} benchmarks.

Signal MC samples where the bulk G_{RS} , with masses between 1.0 and 3.0 TeV, decays into WW or ZZ pairs are generated using MADGRAPH 2.2.2 interfaced to PYTHIA 8 for hadronization with the A14 tuned parameters and the NNPDF23LO PDF sets for the same mass points as for the HVT model. The RMS of the invariant mass of the decay products of the simulated bulk G_{RS} is about 10% of the its pole mass.

Table 2: Resonance width (Γ) and cross-section times branching ratio ($\sigma \times \text{BR}$) of the diboson final states for different pole masses m in the described HVT and graviton model.

m [TeV]	HVT W' and Z'			G_{RS}		
	WW		WZ	WW		ZZ
	Γ [GeV]	$\sigma \times \text{BR}$ [fb]	$\sigma \times \text{BR}$ [fb]	Γ [GeV]	$\sigma \times \text{BR}$ [fb]	$\sigma \times \text{BR}$ [fb]
1.2	40	102.1	212.7	69	29.4	14.9
1.8	56	14.4	30.6	109	2.40	1.21
2.4	74	2.94	6.37	149	0.326	0.164
3.0	92	0.726	1.58	187	0.057	0.029

11.1.4 Background Samples

The dominant background in this analysis is from the multijet QCD processes. Due to the requirement of two high p_T jets in the event, this background is well modeled by simulated dijet processes. Due to the high background rejection of the boosted tagging criteria and the high masses explored in this search, the dijet MC contains too few events in the high dijet mass tails. For the final analysis a parametrized fit is used to model the backgrounds from data. The dijet MC samples are mainly used to test the efficiency of selection criteria, to validate the kinematic distributions and boosted boson jet substructure variables in the background control regions (CR), as well as to study the background fitting functions. These samples are generated with PYTHIA 8.186 with the NNPDF23LO PDF and the A14 ATLAS tune.

In addition to the dijet process, the W/Z +jets process is also considered to study the boosted boson tagging performance. The W +jets and Z +jets events are generated with SHERPA 2.1.1 interfaced with the CT10 PDF set. Only the hadronic decays of the W and Z are included.

11.2 PRESELECTION

In this section the baseline preselections used in this analysis are documented, including the trigger and physics object selections. Veto selections, which are orthogonal to the other signal regions with similar final states, are also described.

11.2.1 Trigger Selection

Events are initially selected by the two level ATLAS trigger system. In this analysis a high E_T , un-prescaled large-radius jet trigger¹ is used. This is the lowest un-prescaled large-radius jet trigger present in the selected 2015 and 2016 data sets. For both data taking periods the offline selections are nearly 100% efficient with these triggers.

¹ HLT_j420_a10_lcw_L1J100 for 2016 and HLT_j360_a10_lcw_sub_L1J100 for 2015.

11.2.2 *Lepton and Missing Transverse Momentum Vetoes*

ATLAS performs additional searches for heavy resonant objects decaying to bosons in non-fully hadronic final states. To ensure they cover independent signal regions each of the searches uses an orthogonal data sample. Lepton and missing transverse momentum vetoes are applied. Events with central ($|\eta| < 2.5$), and high- p_T ($p_T \geq 25$ GeV) leptons (muons or electrons) which pass both medium identification criteria [23, 92] and loose isolation requirements are rejected to place the analysis in an orthogonal region to the (semi-)leptonic diboson channels. Events with a missing transverse momentum above 250 GeV are rejected to produce orthogonality to the $\nu\nu J$ analysis.

11.2.3 *Standard Jet Cleaning*

Jets can be reconstructed from calorimeter signals that come from non-collision sources including calorimeter noise, beam halo and cosmic rays. These can be an important background at high- p_T , and so criteria have been developed using early 2015 data to reject such jets based on timing and jet shape. Events containing a small radius jet failing the loose criteria [93] are rejected.

11.3 EVENT SELECTION

11.3.1 *Jet Selection*

Each event must contain a pair of large-radius jets (as described in Section 6.1) which satisfy the following requirements. Firstly, $|\eta|$ of each jet must be smaller than 2.0 to ensure a good overlap with the volume of the ID, allowing the use of reconstructed tracks for boosted boson tagging (see sec. 11.3.4.1) and systematic uncertainties evaluation [94]. After this selection, the leading- p_T jet must have $p_T > 450$ GeV, to ensure full trigger efficiency.

The two leading jets with the highest p_T passing the requirements in each event are taken as the initial boson candidates. These are taken to arise from the decay of the signal particle $X \rightarrow VV$, where X is one of the theoretical particles mentioned in the introduction and V is either a W or Z . To avoid sculpting the dijet mass spectrum by the jet p_T requirement, the invariant mass formed from the two leading jets, m_{JJ} , is required to fulfill $m_{JJ} > 1.0$ TeV.

11.3.2 *Rapidity Difference*

Signal events produced by the s -channel are more central than the t -channel QCD multijet background events - the signal peaks near $\Delta y_{12} = 0$, whereas the background peaks at larger values of $|\Delta y_{12}|$.

This selection was optimized using the modeling in MC samples for the $W' \rightarrow WZ$ models. By requiring that the dijet mass in both signal and dijet MC is within $\pm 10\%$ of the generated W' mass, only the relevant region of phase space is selected.

Figure 51 shows the rapidity separation between the two leading trimmed anti- k_t $R = 1.0$ jets in QCD MC, W' MC and data for different dijet mass ranges corresponding

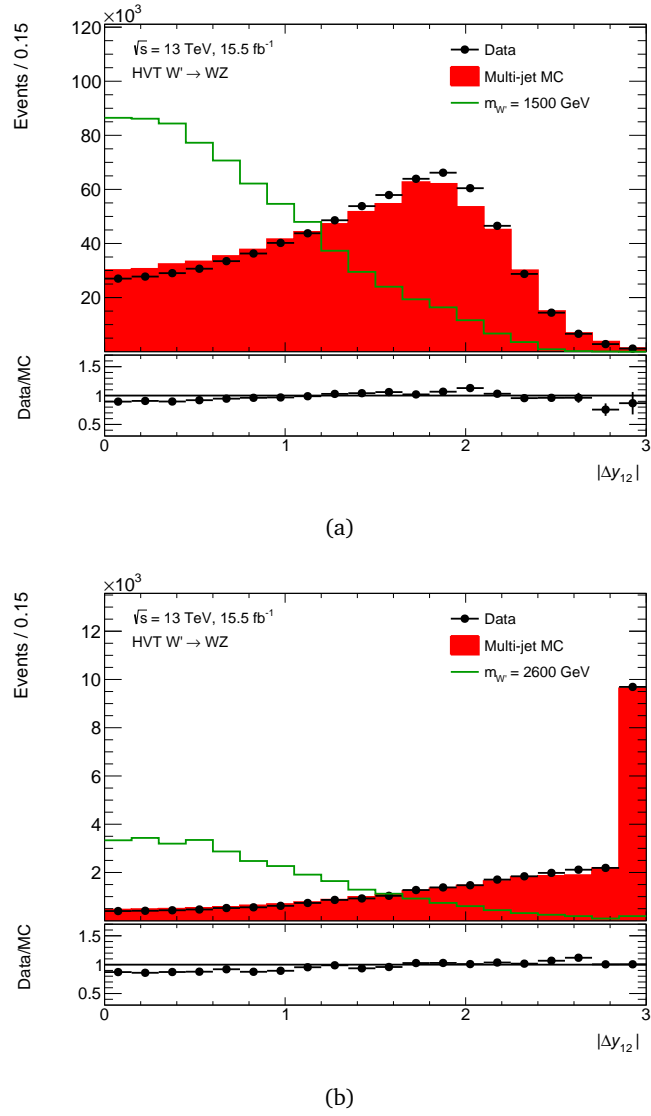
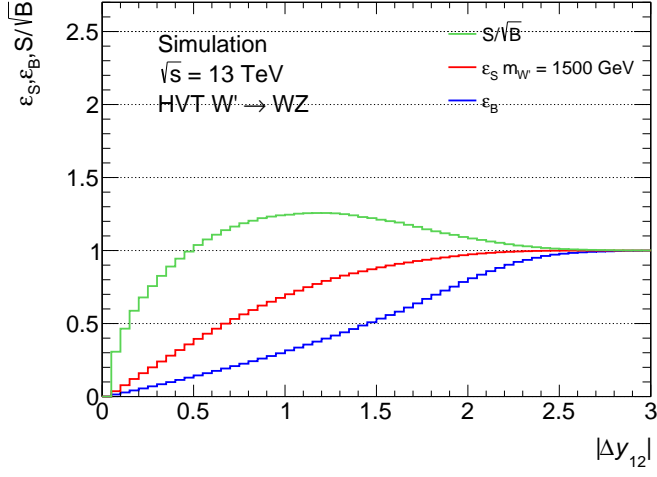
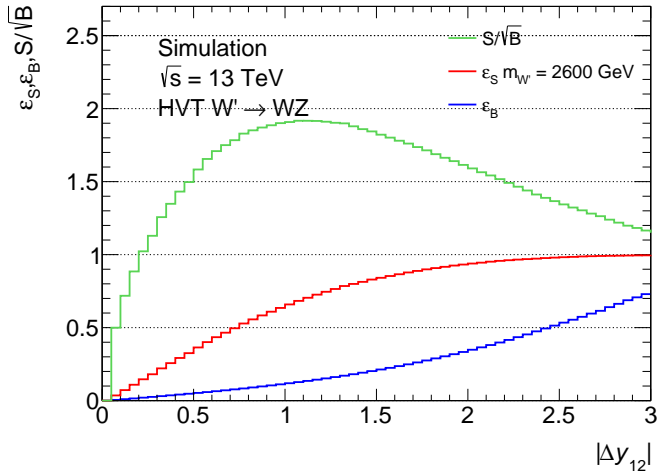


Figure 51: Rapidity separation between the two leading trimmed anti- k_t $R = 1.0$ jets in QCD MC and W' MC. Events in the histograms have been selected after passing trigger selection, narrow m_{JJ} windows, $|\eta| < 2.0$ and leading jet $p_T > 450$ GeV. Each subfigure displays a different dijet mass range corresponding to the relevant phase space for the benchmark signal indicated - around (a) 1500 GeV and (b) 2600 GeV.

to the relevant phase space for the benchmark signal indicated. The ratio of signal over the square root of background (SSB) was calculated for the full range of possible selection criteria, comparing a selection of different mass signal W' samples with the dominant QCD background. The optimal cut was taken as the one which provided a large SSB ratio and signal efficiency over the full range of signal masses considered. The inputs to this optimization can be seen in Figure 52. The cut value is chosen as $\Delta y_{12} < 1.2$.



(a)



(b)

Figure 52: Optimization of the rapidity separation selection between the two leading trimmed anti- k_t $R = 1.0$ jets. Events in the histograms have been selected after passing trigger selection, narrow m_{JJ} windows, $|\eta| < 2.0$, leading jet $p_T > 450$ GeV. Each subfigure displays a different dijet mass range corresponding to the relevant phase space for the benchmark signal indicated - around (a) 1500 GeV and (b) 2600 GeV. The SSB (green) for a range of selection criteria are shown for a sub-set of W' signal masses. In red and in blue are shown respectively the signal and background efficiency for different value of rapidity separation cut.

11.3.3 p_T Asymmetry

Only two highly energetic jets are expected as the final state for the considered signal models. These two jets should form a balanced system, so there p_T should be nearly identical. This balance can be quantified in form of the p_T asymmetry defined as

$$A = \frac{p_{T1} - p_{T2}}{p_{T1} + p_{T2}}, \quad (13)$$

where p_{T1} and p_{T2} are the p_T of the leading and sub-leading jets. Without any radiation in the final or initial states and the lack of detector or reconstruction effects which result in a jet p_T resolution different from zero, A would be zero. This is true for both the considered signals and the dijet background. This cut is therefore applied to remove any event where either of the jets is badly reconstructed, rather than to suppress the background. Figure 53 shows the distribution of the p_T asymmetry in data and signal and background MC events.

The selection requirement placed on this variable was optimized using the modeling in MC samples, applying $|\Delta y_{12}| < 1.2$ and the same phase space and baseline selection used for the optimization of the rapidity separation cut. The SSB was calculated for the full range of possible selection criteria, comparing a selection of different mass signal W' samples to the dominant QCD background. The final cut value $A < 0.15$ was chosen to still be on the plateau of the selection efficiency for the signal. The inputs to this optimization can be seen in Figure 54.

11.3.4 Boosted Boson Tagging

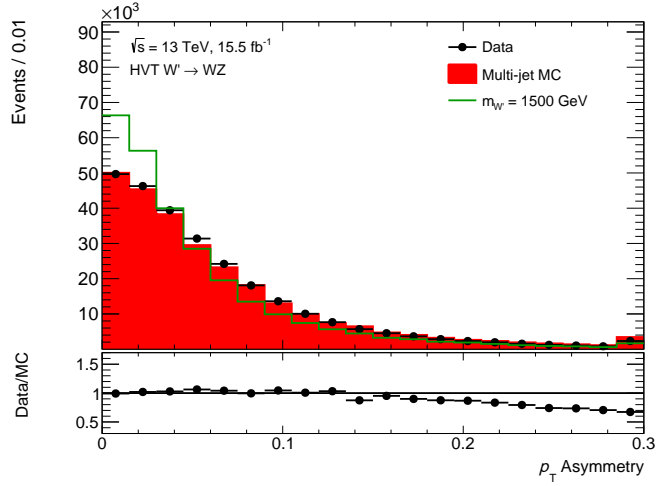
To enhance the separation between the signal boson jets and the QCD jets, several discriminating jet substructure variables have been studied in the past [94]. The largest separation between signal and background jets has been achieved by applying additional cuts on three discriminating variables:

Trimmed jet mass: the trimmed jet mass should be consistent with the boson mass for jets from hadronically decaying bosons while for jets from the background it should be small .

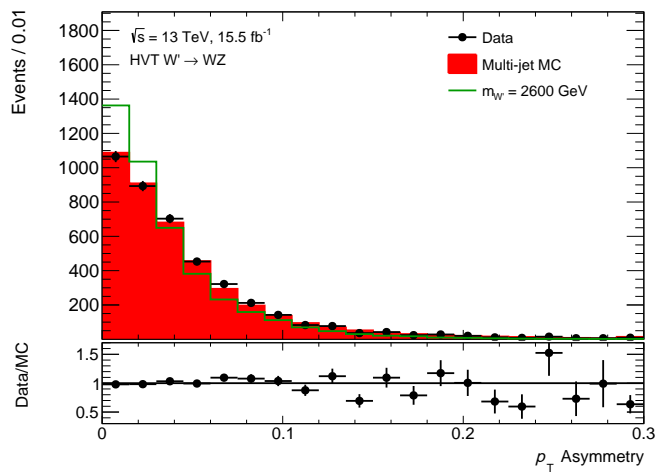
D_2 : boson jets are characterized by a two-prong structure, while QCD jets are mainly one-prong. This discriminant is a variation on the ratio of energy correlations which optimizes the separation between one-prong and two-prong decays, in analytical terms [94].

Number of tracks associated to the untrimmed jet, n_{trk} : background events containing hard gluons are likely to pass the D_2 cut. Using the fact that energetic gluon emissions, on average, produce jets with high charged particle multiplicities, this cut can remove them.

Figure 55 shows a diboson candidate event passing the full analysis selection. The two-prong structure one expects for these jets, and to which the D_2 selection is sensitive, can be observed for both jets.

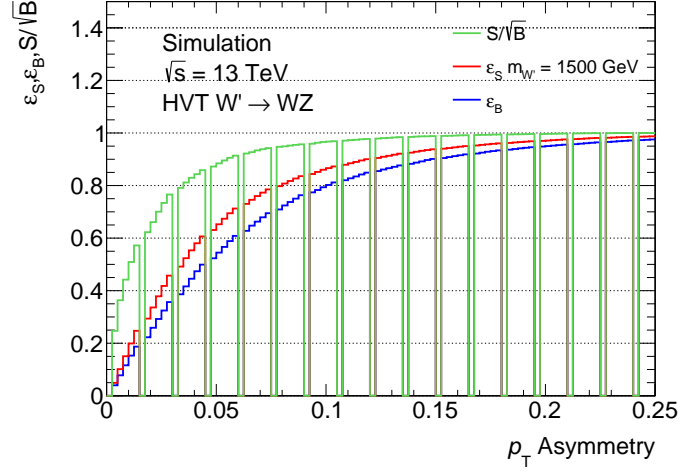


(a)

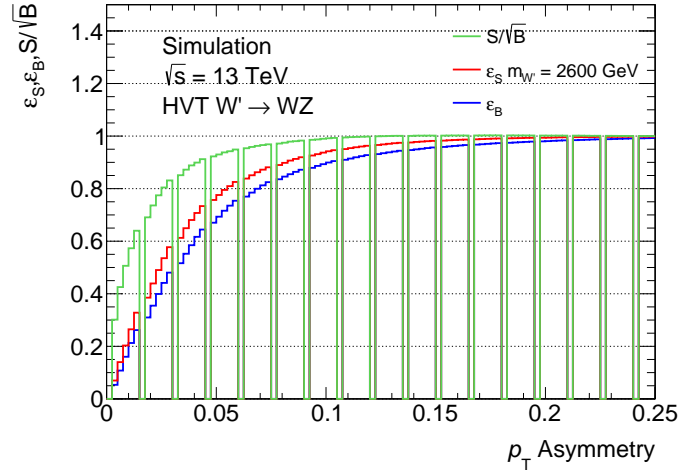


(b)

Figure 53: Transverse momentum asymmetry distribution between leading and sub-leading trimmed anti- k_t $R = 1.0$ jets in QCD MC and W' MC. Events in the histograms have been selected after passing trigger selection, narrow m_{JJ} windows, $|\eta| < 2.0$, leading jet $p_T > 450 \text{ GeV}$ and $|\Delta y| < 1.2$. Each subfigure displays a different dijet mass range corresponding to the relevant phase space for the benchmark signal indicated - around (a) 1500 GeV and (b) 2600 GeV.



(a)



(b)

Figure 54: Optimization of the transverse momentum asymmetry selection between leading and sub-leading trimmed anti- k_t $R = 1.0$ jets. The QCD and signal MC are normalized to unity. Events in the histograms have been selected after a cut of $|\eta| < 2.0$, a $|\Delta y| < 1.2$ requirement and the trigger plateau is modeled by a $p_T > 450$ GeV requirement on the input jets. Each subfigure displays a different dijet mass range corresponding to the relevant phase space for the benchmark signal indicated - around (a) 1500 GeV and (b) 2600 GeV. The SSB (green) for a range of selection criteria are shown for a sub-set of W' signal masses. The signal and background efficiency for different values of p_T balance are shown in red and blue.

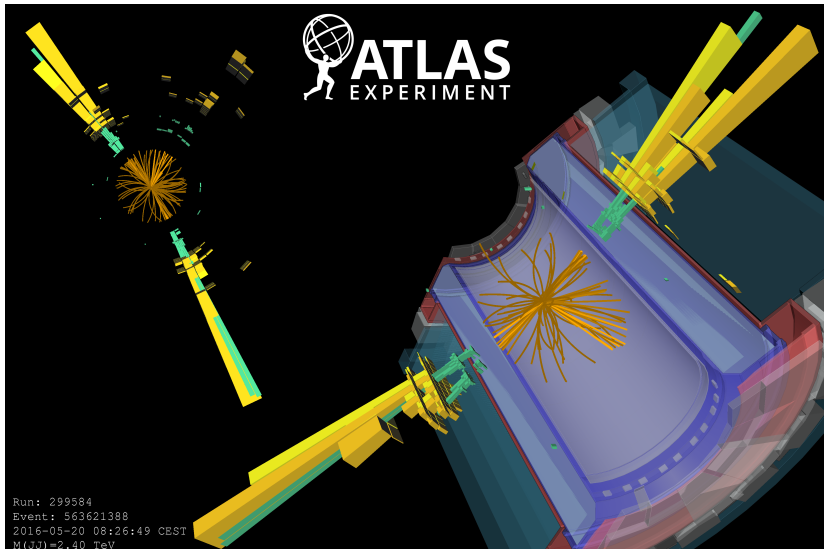


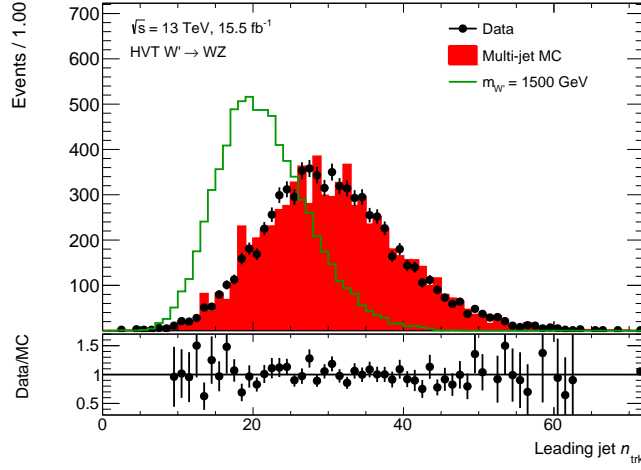
Figure 55: Event display of a diboson candidate event recorded by the ATLAS detector on 20th of May 2016. The dijet invariant mass is 2.4 TeV. The leading (sub-leading) jet transverse momenta is 1.26 TeV (1.15 TeV). The leading (sub-leading) jet invariant mass is 83.7 GeV (73.9 GeV). The $n_{\text{trk}}(D_2^{(\beta=1)})$ is 25 (1.62) for leading jet and 24 (1.34) for sub-leading jet.

The optimization and definition of jet mass and D_2 cuts are described in Reference [94]. Boosted boson tagging based on trimmed anti- k_t $R = 1.0$ jets with cuts on jet mass and D_2 is currently used in all ATLAS analyses which include hadronic bosons in the final state. A working point with a constant 50 % boson selection efficiency has been chosen for this analysis. The selection on the number of tracks associated with the untrimmed jet increase the QCD rejection power, while preserving high signal efficiency, and it has been designed and optimized specifically for this analysis.

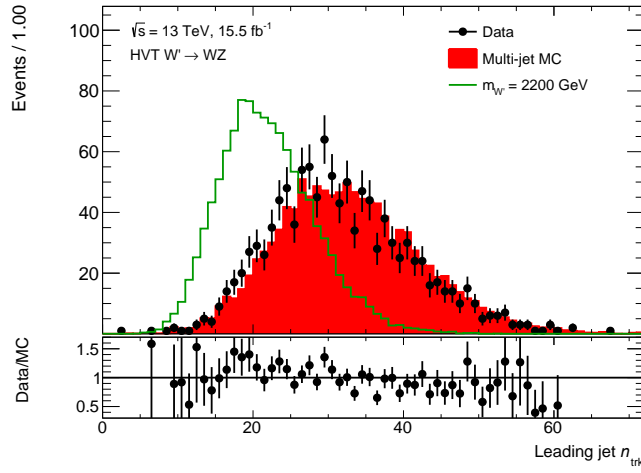
11.3.4.1 Track Multiplicity

Both mass and D_2 cuts can be passed by background jets containing radiation from a hard gluon, because they are likely to exhibit a two prong structure as expected from the signal. With increasing energy, the number of charged hadrons increases for both gluon and quark induced jets [95]. Even so, on average, gluon-induced jets produce a much higher charged particle multiplicity than quark-induced jets of the same energy. The relevant scale for QCD dijet background is the momentum of the jet, while for decays of boosted bosons it is the boson mass. Since the former is much lower, one can use this to discriminate between the two processes. By cutting on the multiplicity of tracks associated to the trimmed jet, n_{trk} (proportional to the charged hadron multiplicity), one can increase the background rejection while retaining most of the signal efficiency.

Tracks fulfilling the minimum ID quality requirements and matched to the event primary vertex, are associated to jets using the ghost association procedure. Figures 56 and 57 show the distribution of the number of tracks associated with large-radius jets before trimming, for HVT W' signals, dijet MC and data passing the same selections



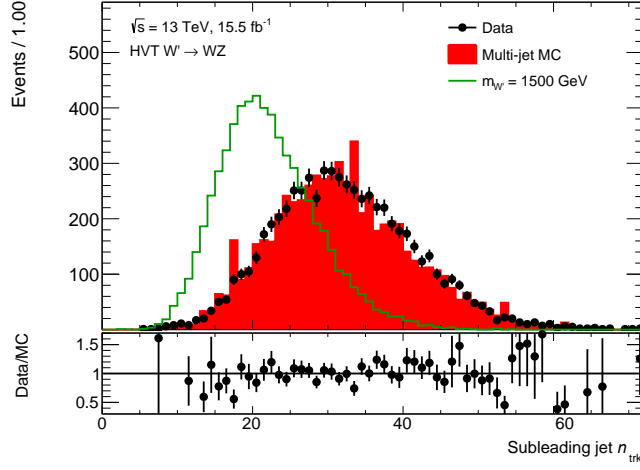
(a)



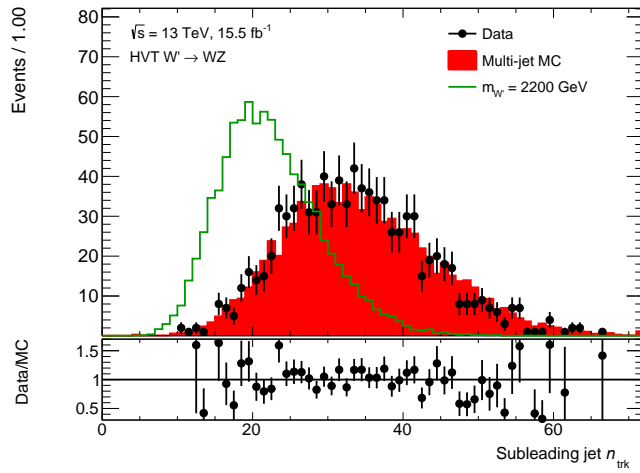
(b)

Figure 56: Transverse trimmed anti- k_t $R = 1.0$ jets in QCD MC and W' MC. n_{trk} for the leading jet. The QCD and signal MC are normalized to data. Events in the histograms have been selected after passing trigger selection, $|\eta| < 2.0$, leading jet $p_T > 450$ GeV, $|\Delta y| < 1.2$, $A < 0.15$ as well as partial boson tagging. Two different dijet mass range corresponding to the relevant phase space for the benchmark signal indicated are shown - around (a) 1500 GeV and (b) 2200 GeV.

as for the optimization described in the following. The selection requirement placed on this variable is optimized using the modeling in MC samples, requiring that all the events have passed the baseline selections as well as containing two large-radius jets successfully tagged as a boson by the D_2 and jet mass requirements. The optimal cut, $n_{\text{trk}} < 30$, was taken as the one which provided a large SSB ratio and signal efficiency over the full range of signal masses considered, as seen in Figure 58. Using n_{trk} to identify weak boson jets improves the expected sensitivity by approximately 20–30%.

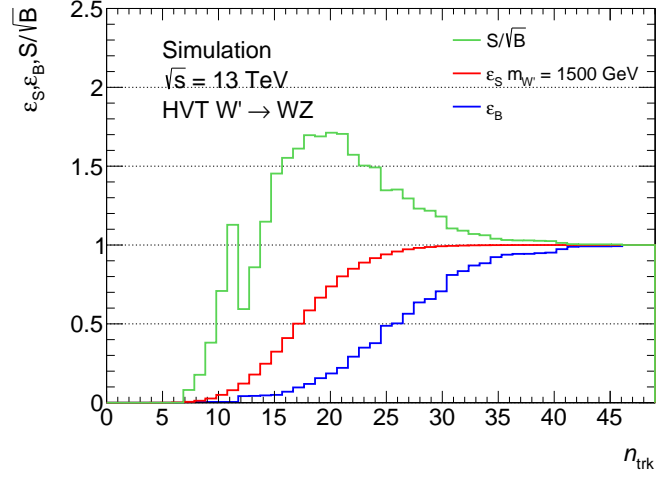


(a)

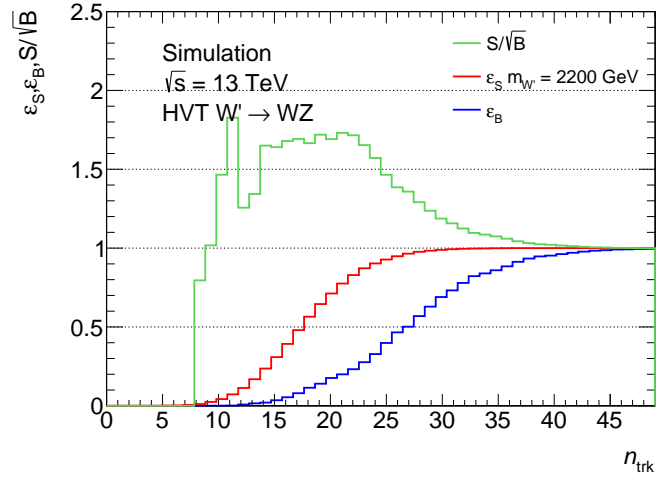


(b)

Figure 57: Transverse trimmed anti- k_t $R = 1.0$ jets in QCD MC and W' MC. n_{trk} for the subleading jet. The QCD and signal MC are normalized to data. Events in the histograms have been selected after passing trigger selection, $|\eta| < 2.0$, leading jet $p_T > 450$ GeV, $|\Delta y| < 1.2$, $A < 0.15$ as well as partial boson tagging. Two different dijet mass range corresponding to the relevant phase space for the benchmark signal indicated are shown - around (a) 1500 GeV and (b) 2200 GeV.



(a)



(b)

Figure 58: Optimization of the n_{trk} selection. Events in the histograms have been selected after passing trigger selection, narrow m_{JJ} windows, $|\eta| < 2.0$, leading jet $p_T > 450 \text{ GeV}$, $|\Delta y| < 1.2$ and $A < 0.15$ as well as partial boson tagging. The optimization plots are showed for (a) 1.5 and (b) 2.2 TeV W' signal samples, corresponding to the relevant phase space for the benchmark signal indicated. The SSB is in green, while in red and in blue are shown respectively the signal and background efficiency for different value of n_{trk} cut.

The pile-up dependence of n_{trk} has been studied and found to be negligible. A data sample of $V + \text{jets}$ events is used to estimate the relative efficiency and background rejection of the n_{trk} cut, as described in Section 11.4.3.

Figure 59 shows the selection efficiency for the HVT and bulk G_{RS} signals as a function of the resonance mass. For the WW and WZ decay in the HVT model, and the $G_{RS} \rightarrow WW$ decay in the bulk RS model, the acceptance times selection efficiency is around 0.12. The $G_{RS} \rightarrow ZZ$ decay in the bulk RS model has a lower acceptance times selection efficiency around 0.09 to 0.1.

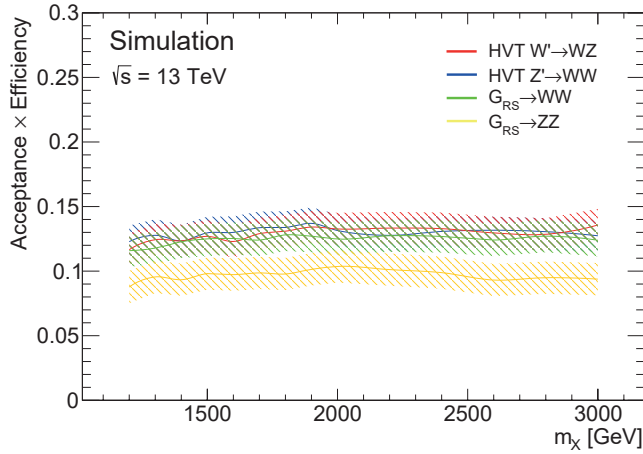


Figure 59: Selection efficiency for HVT model $Z' \rightarrow WW$, $G_{RS} \rightarrow WW$, HVT model $W' \rightarrow WZ$ and $G_{RS} \rightarrow ZZ$ benchmark signals after applying either the full WW , WZ or ZZ selections.

11.4 CONTROL REGIONS

Various data CR are used to evaluate the efficiency of selections made in the analysis or the effectiveness and flexibility of the background modeling procedure. A brief description of each follows here.

11.4.1 Mass Sideband Regions

Alternative mass window selections to the boson tagger are used to test the effectiveness of the background modeling function without unblinding the signal region. The following sidebands are considered:

- A low mass sideband region: Both leading jets are required to have $50 < m_J < 65$.
- A high mass sideband region: Both leading jets are required to have $110 < m_J < 140$. However, this mass window contains the signal region of analyses using Higgs in the event. To avoid the possibly unblinding of the signal region of e.g. vector-associated Higgs production a veto on b -tagged large- R jets is imposed. A

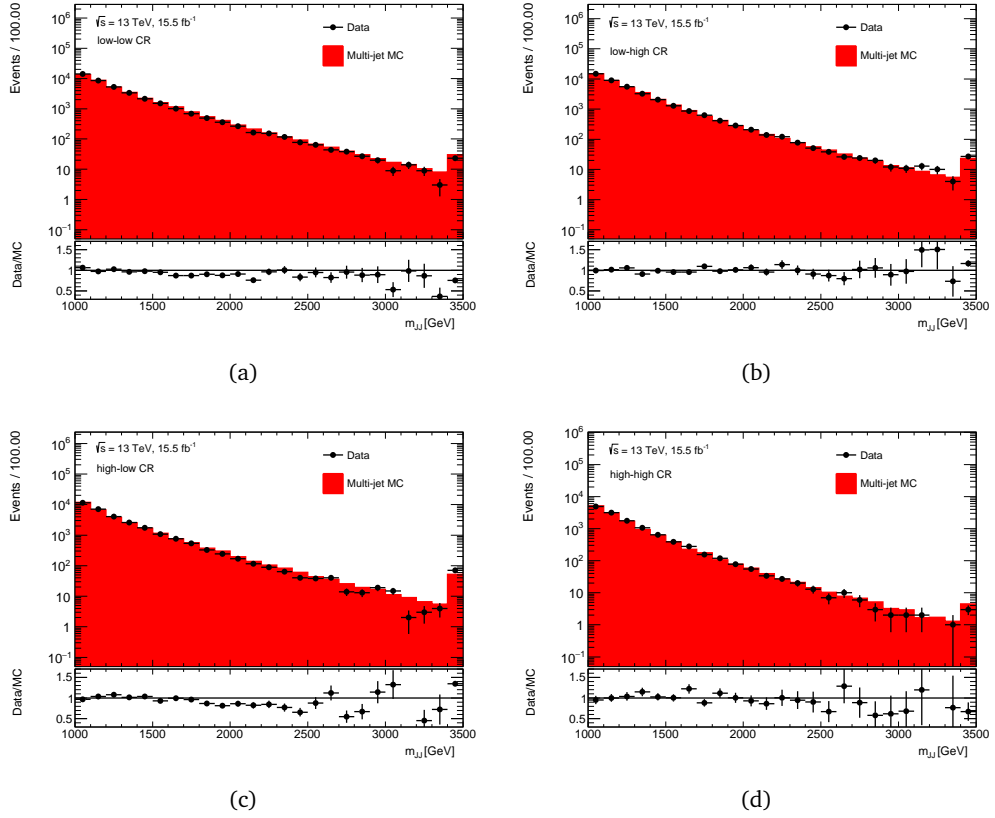


Figure 60: Invariant dijet mass distributions in data and MC simulation for the (a) low-low and (b) low-high (c) high-low and (d) high-high sideband CR.

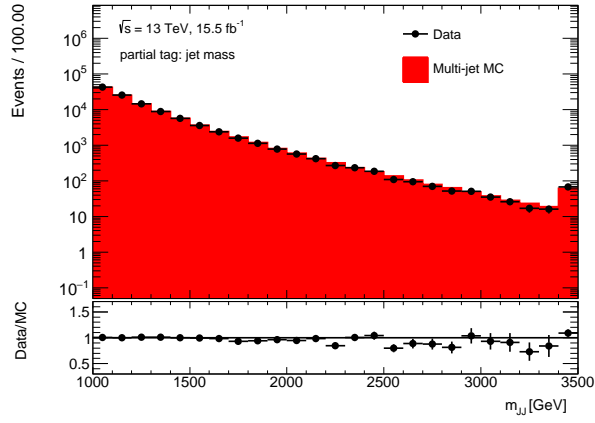
large- R jet is b -tagged if more than one of the ghost-associated $R = 0.2$ subjects is b -tagged.

- Mixed mass sideband regions: Using combinations of low/high mass window cuts on the leading and sub-leading jets to form additional sideband regions.

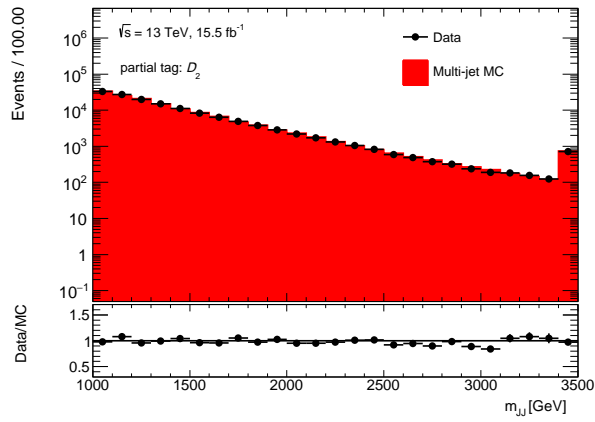
The invariant dijet mass spectrum for all four sideband CR in data and MC are shown in Figure 60. Agreement within 10% can be observed for $m_{JJ} < 1.5$ TeV where statistical uncertainties do not dominate.

11.4.2 Partial-tag Control Regions

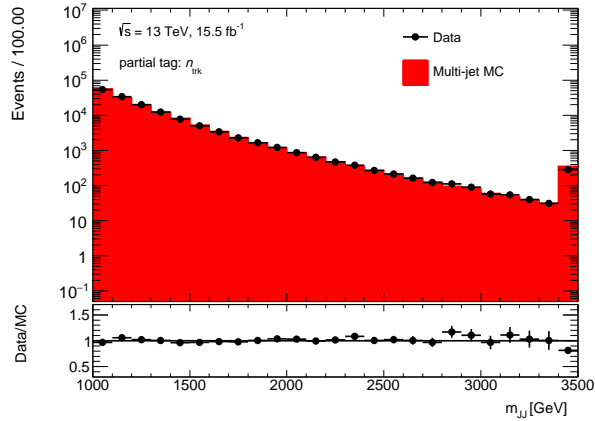
The performance of the boson tagging requirements and their impact on the invariant dijet mass spectrum is important to understand if the jet mass, D_2 or n_{trk} requirements are sculpting the background. The m_{JJ} distribution after applying either a selection on the jet mass window, the energy correlation variable D_2 or the n_{trk} are shown in Fig. 61. No sculpting of the distribution in either MC or data can be observed. Even though large statistical fluctuations can be observed above approximately 1.5 TeV, the low m_{JJ} spectra in data is well reproduced by MC.



(a)



(b)



(c)

Figure 61: Invariant dijet mass distributions in data and MC simulation after requiring (a) the leading and sub-leading jet to be within the mass window of the boson tagger, (b) after applying the D_2 criteria derived for a 50% working point and (c) after applying the n_{trk} selection.

11.4.3 V +jets CR

A sample enriched in vector boson plus jets is obtained starting from the pre-selection of two jets in an $|\eta| < 2.0$ region. Further, it is requested that the leading jet has a p_T larger than 550 GeV and successfully is tagged by the D_2 selection as either a W or a Z . The resulting events have a small peak in the mass distribution which can be used to fit the rate of $W + Z$ signal, even in bins of the number of charged tracks. Using the data/MC ratio of the fitted rate of W/Z bosons as a function of n_{trk} the quality of the description of the n_{trk} variable in MC simulation can be assessed.

The m_J distribution in the CR for $n_{\text{trk}} < 30$ is shown in Figure 62 (a) - black dots represent data and red squares denote simulation. The fitted m_J distribution, composed of the multijet background and the W and Z peaks, is plotted as a solid black line, and the dashed red line shows solely the background component. Both mass and width of the fitted $W + Z$ peak in data are well modeled by the MC simulation. Figure 62 (b) shows the fitted fraction of W/Z jets for data and simulation as a function of n_{trk} . Two distributions are shown for the simulated n_{trk} , one without modifications and one where the distribution is scaled by 1.06 to best match the distribution observed in data. This scale difference is used as a systematic uncertainty on the n_{trk} modeling.

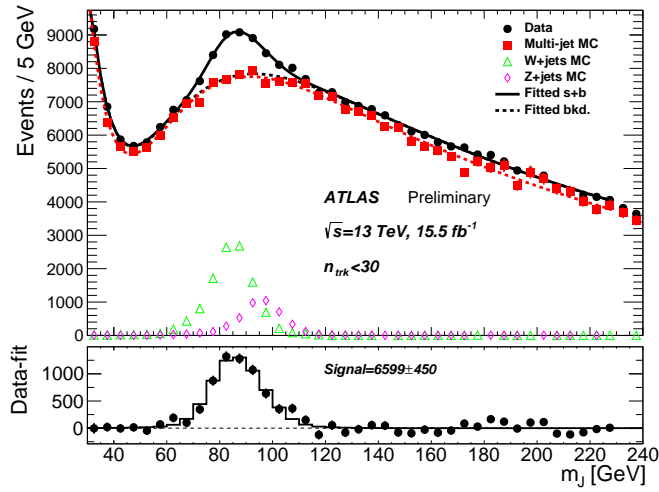
11.5 BACKGROUND PARAMETRIZATION

The search for diboson resonances is performed by looking for narrow peaks above the smoothly falling m_{JJ} distribution expected in the SM. This smoothly falling background is overwhelmingly composed of SM QCD dijet events. Other processes, which also fall smoothly as a function of m_{JJ} , like SM dibosons, $W/Z + jets$ and $t\bar{t}$, have small (below few percent) to negligible contributions to the background. The background to the search is estimated empirically from the observed m_{JJ} spectrum in the signal region. The background estimation procedure is based on a binned maximum-likelihood fit of the observed m_{JJ} spectrum to a parametric form. This is given by

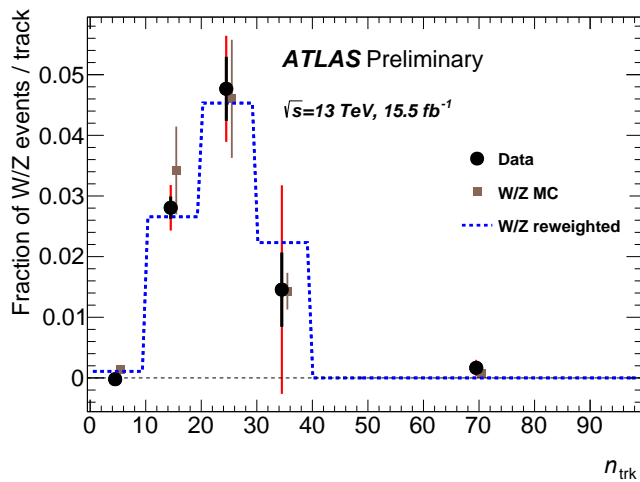
$$\frac{dn}{dx} = p_1(1-x)^{p_2+\xi p_3} x^{p_3} \quad (14)$$

where $x = m_{JJ}/\sqrt{s}$, p_1 is a normalization factor, p_2 and p_3 are dimensionless shape parameters, and ξ is a constant chosen to minimize the correlation between p_2 and p_3 in the fit. The fit is performed on a histogram of the observed m_{JJ} distribution in data with a constant bin size of 100 GeV. The fit range is $1.0 < m_{JJ} < 3.5$ TeV, where the lower bound is dictated by the point where the trigger is fully efficient for boson-tagged jets. The upper bound is set because the D_2 parametrization is available for jets with p_T only up to 2 TeV and therefore the signal selection efficiency drops after 3.5 TeV affecting the fit.

The modeling of the parametric shape in Equation 14 is tested in simulation and the background enriched CRs in data defined in Section 11.4. Figure 63 shows the fit results performed in the high and mixed mass CRs in data and Table 3 list the results of the fits.

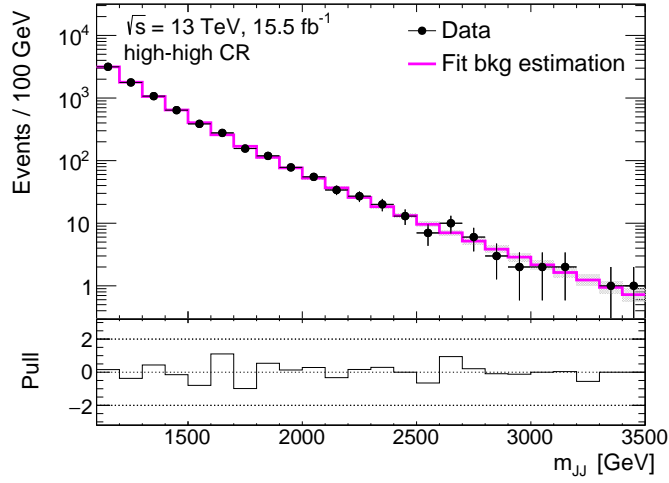


(a)

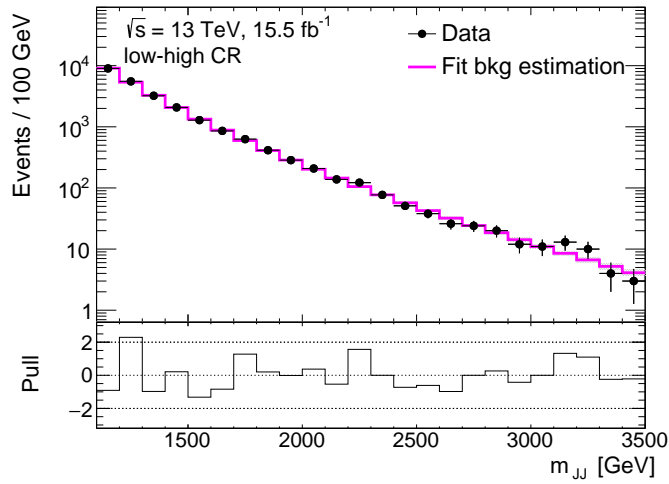


(b)

Figure 62: (a) Comparison of the m_j distribution between data and dijet simulation for jets with $p_T^{\text{jet}} > 550$ GeV and passing the D_2 boson requirement. The expected shape of the boson peak from W/Z +jets simulation is also shown. On the bottom, the difference between data and the fitted background is shown. (b) Comparison of relative fraction of W/Z -jets as a function of n_{trk} . Simulation is shown with and without a reweighting based on the fitted scale difference to data. Statistical errors are indicated by black error bars for data. The red error bars include systematic uncertainties of the method.



(a)



(b)

Figure 63: Comparison between the fitted m_{JJ} shape (statistical uncertainty shown as gray error band) and the m_{JJ} data spectra in CRs. In (a) events are selected requiring to be in the high-high sideband mass CR and in (b) to be in the low-high sideband mass CR. The bottom plot in the figures show the pull, defined as the z-value as described in Reference [96].

Table 3: Goodness-of-fit for maximum-likelihood fits of the background model to the dijet mass distribution in high, low and mix mass CR.

Sample	χ^2/n_{DOF}	p -value
Data in low-low CR	19/22	0.63
Data in high-high CR	7.0/21	1.00
Data in low-high CR	20.8/22	0.54

11.6 SYSTEMATIC UNCERTAINTIES

The uncertainties effecting the background modeling are taken directly from the errors on the fit parameters of the background estimation procedure described in Section 11.5. The systematic uncertainties on the expected signal yield and shapes arise from detector effects and MC modeling. These are evaluated using the signal MC samples over the search region $1.0 < m_X < 3.5$ TeV. Systematic uncertainties on signal shape and normalization are assessed and expressed in terms of nuisance parameters in the statistical analysis as shown in Section 11.7.2. Uncertainties due to the large-radius jet calibrations affect the large-radius jet p_T , mass and D_2 . It is assumed that p_T and mass scale are fully correlated, while the scale of D_2 is uncorrelated with the former two.

11.6.1 Jet Energy and Mass Scale

Uncertainties on the JES are an important effect in the search for resonant structures in the presence of a rapidly falling background spectrum. This uncertainty shifts the expected signal mass spectrum, particularly the peak of the resonance, affecting the significance of an excess if observed. Uncertainty in the JMS affects the observed jet mass, which in turn affects the boosted tag selection efficiency and the dijet mass shape.

The JES and JMS systematic uncertainties on the trimmed large-radius jets are evaluated using the methods described in Section 10.4. The size of the total JES and JMS uncertainties vary with jet p_T and are around 5% and 3% for the full mass range.

11.6.2 Jet Energy and Mass Resolution

Uncertainties in the measurement of the jet energy resolution (JER) and JMR would lead to a mis-measurement of the width of any observed signal and affect the signal selection efficiency. An uncertainty in the measurement of the JMR smears out the observed jet mass distribution. The JER and JMR uncertainties are evaluated by applying an additional relative Gaussian smearing on the input jets energy and mass, degrading the nominal resolution by 20%. This is performed in four bins of jet p_T , 250 – 500 GeV, 500 – 1000 GeV, 1.0 – 1.5 TeV and ≥ 1.5 TeV to account for the dependence of jet p_T .

11.6.3 D_2 Scale and Resolution

Any uncertainty on the value of the boson tagging discriminant D_2 used here would affect the selection efficiency of the analysis. Any variation observed will be taken as a systematic uncertainty on the value of the cut, evaluated by shifting the cut value by the uncertainty. The systematic uncertainty on the trimmed large-radius jets used in this analysis has been evaluated using the methods described in Section 10.4. The size of the uncertainty varies with jet p_T and is around 6% for the full mass range.

Uncertainty in the D_2 resolution acts to smear out the D_2 distribution and thus alters the efficiency of the final analysis cut. This is evaluated as an additional relative Gaussian smearing of the input jets D_2 , degrading the nominal resolution by 10%. This

is performed in four bins of jet p_T , 250 – 500 GeV, 500 – 1000 GeV and ≥ 1.0 TeV as the nominal D_2 resolution varies with jet p_T . The response of the D_2 cut is not strictly Gaussian and thus the RMS of the observed distribution is taken as a conservative approximation to the width.

11.6.4 Track-multiplicity Efficiency

Uncertainties on the number of tracks associated with the untrimmed jet can affect the signal selection efficiency. The modeling of this variable is discussed in Section 11.4.3, and an uncertainty of 6% is estimated.

11.6.5 Luminosity Scale

The preliminary uncertainty on the integrated luminosity of both the 2015 and 2016 data sets is 3.0%. It is derived from a preliminary calibration of the luminosity scale using x-y beam separation scans performed in August 2015 and May 2016. A detailed description of this method is given in Reference [89] and [97].

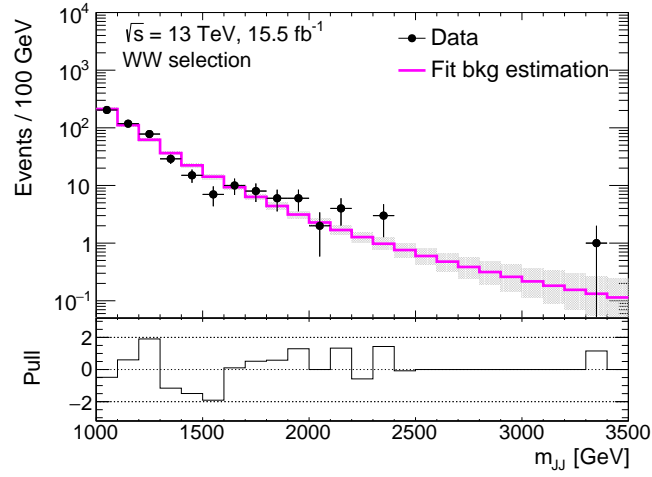
11.7 RESULTS

11.7.1 Background Only Fit Results in Signal Regions

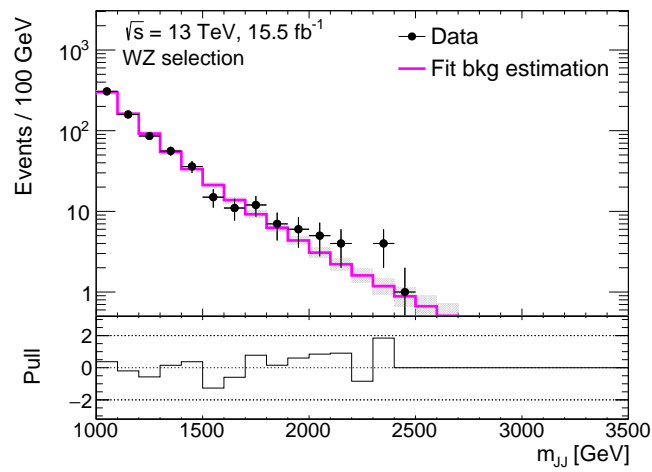
A background-only binned maximum likelihood fit is first performed on the observed dijet invariant mass distribution in data, with the background modeling function described in Section 11.5. Figure 64 shows the dijet invariant mass distribution observed in the WZ , WW and ZZ signal region in data, compared to the fitted background shape. The uncertainties of the fitted parameters are propagated to the dijet mass distribution and are shown as shaded-bands. The lower panels in the figure show the significances, defined as the signed z -value of the difference between the observed data and the expectation [96]. The fitted values of the parameters are summarized in Table 4. No significant excess is observed in data.

Table 4: Fitted parameters of the dijet mass distribution and number of observed events for each signal region.

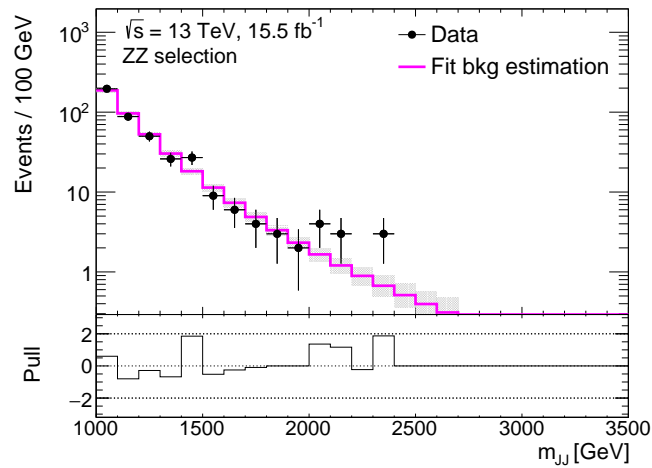
Parameter	WW	WZ	ZZ
ξ	7.54	7.79	7.72
p_2	51.0 ± 2.0	53.3 ± 1.8	54.6 ± 2.3
p_3	7.8 ± 1.4	6.6 ± 1.2	7.9 ± 1.6
Observed events	491	709	421



(a)



(b)



(c)

Figure 64: The observed distributions in data in the (a) WW , (b) WZ and (c) ZZ signal regions. The fitted background is also shown, where the shaded-bands are its uncertainty.

11.7.2 Statistical Analysis

The data is interpreted with a frequentist analysis by calculating the signal strength, μ for each of the benchmark models. μ scales with the number of signal events predicted by the analysis, and for the signal plus background hypothesis equals unity. In contrast, μ is zero for the background only hypothesis. A test statistic, $\lambda(\mu)$, based on the profile likelihood ratio [98] is used to test the two benchmark models. A maximum likelihood fit of the signal plus background hypothesis to the data extracts the value of μ . If any excess is observed over the background only hypothesis, it is quantified in terms of local p_0 . It corresponds to the probability of the background only hypothesis to produce an excess at least as large as the one observed. The largest p_0 in this search has a local significance of 2.1 standard deviations for a HVT W' and a RS graviton decaying to WW at a resonance mass of 1.2 TeV as shown in Figure 65. Such a deviation is consistent with the expected background fluctuations.

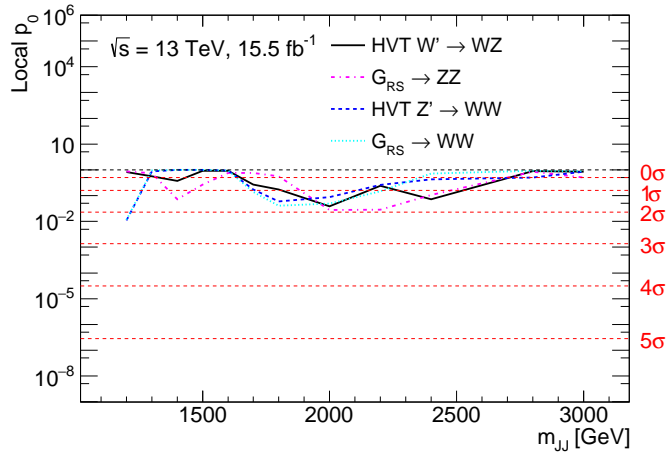


Figure 65: Observed p_0 -values for the HVT $Z' \rightarrow WW$, and $W' \rightarrow WZ$, and bulk RS graviton $G_{RS} \rightarrow WW$ and $G_{RS} \rightarrow ZZ$ signal models. Very similar p_0 -values are expected for both WW signals, since they both produce similar signal shapes and the used data distribution is identical.

Limits on the production cross section times branching ratio of each considered signal model are set as a function of the resonance mass. For the WZ selections, the HVT W' is used as benchmark and for the ZZ selection, the bulk G_{RS} is used. Both Z' and G_{RS} are used as benchmark for the WW selection. Figure 66 (a) and Figure 66 (b), show the observed 95% CL upper limits on the cross section times branching ratio on the HVT $W' \rightarrow WZ$ and $Z' \rightarrow WW$ hypotheses as function of the W'/Z' mass. New resonances of the HVT model are excluded for masses between 1.2-2.0 TeV for the WZ channel, and between 1.2-1.7 TeV for the WW channel with 95% CL.

Figures 66 (c) and Figure 66 (d) show the observed 95% CL upper limits on the cross section times branching ratio for the bulk $G_{RS} \rightarrow ZZ$ and WW respectively. No exclusion can be made for this model, since the cross section times branching ratio for excited graviton production is below the sensitivity of this analysis.

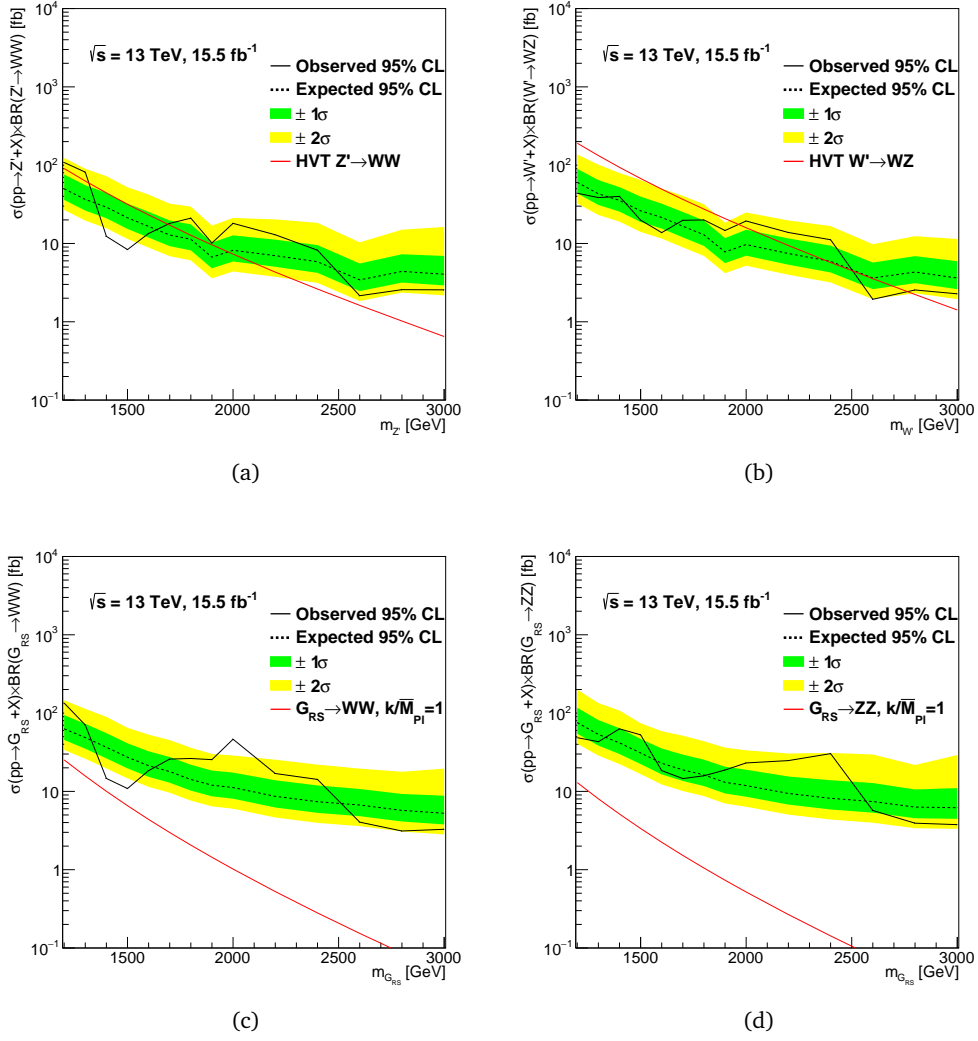


Figure 66: Observed and expected 95% CL limits on the cross-section times branching ratio for (a) HVT $Z' \rightarrow WW$, (b) HVT $W' \rightarrow WZ$, (c) bulk RS graviton $G_{RS} \rightarrow WW$ and (d) bulk RS graviton $G_{RS} \rightarrow ZZ$ channels to diboson final states.

CONCLUSION

The Large Hadron Collider entered a new energy regime at Run 2 with proton–proton collisions at $\sqrt{s} = 13$ TeV. Events with multi-TeV jets showering in the detectors, or tau-leptons and b -hadrons surviving passage through multiple active layers of material, are now common place. These objects are also signatures for new physics, including massive particles that decay to highly boosted bosons, whose own subsequent decay products are often reconstructed into one large-radius jet. One of the strongest discriminants between these jets and the multijet background is their mass.

In the core of highly energetic hadronic jets, the average separation of charged particles is comparable to the size of individual inner detector elements. As a result, their charge deposits in the pixel and SCT detector start to overlap and can be reconstructed as a single merged cluster. This can create confusion within the algorithms reconstructing charged particle trajectories (tracks). Without careful consideration, the track reconstruction efficiency in these dense environments will be limited.

An overview of the offline track reconstruction in ATLAS is given, and the work leading to a vastly improved setup in terms of performance in dense environments for Run 2 is presented. Key developments in the ambiguity solver, in combination with a novel use of a neural network to identify merged pixel clusters, are presented. The improved performance is demonstrated for highly collimated tracks from decays of single particles, as well as in the more physical environment of hadronic Z' decays in the presence of event pile-up. Up to 10% more pixel clusters are associated to tracks in the core of high p_T jets, which results in a much more robust track reconstruction efficiency. This improvement becomes most apparent for charged particles with a high production radius (>30 mm), where 17% efficiency is recovered, as well as in the core of high p_T b - and light-jets, where 10% and 14% efficiency is recovered. The higher quality and efficiency of reconstructed tracks directly boosts the performance of several derived physics objects, which is demonstrated with the example of flavor tagging. For flavor tagging a 7–13% improvement in b -jet efficiency is achieved for a fixed light-jet rejection for jets with $p_T > 100$ GeV, using an IP3D tagger which has not been re-optimized.

Extending these Monte Carlo based studies, two methods are introduced to probe the track reconstruction performance in data. First, a study of the properties of pixel clusters for collimated track pairs allows for a comparison of the identification efficiency of merged pixel clusters in data and simulation. For separations between the pair of tracks below the dimension of a single pixel, the efficiency for identifying the cluster as merged and assigning it correctly to both tracks is above 80% for the IBL and above 90% for the B-layer. The results are consistent between data and simulation, with small residual discrepancies. Using data alone, the second method is able to quantify a residual inefficiency of the track reconstruction in the core of jets as a function of the transverse momentum of the jet using the energy loss in silicon. It varies from $0.061 \pm 0.006(\text{stat.}) \pm 0.014(\text{syst.})$ to $0.093 \pm 0.017(\text{stat.}) \pm 0.021(\text{syst.})$ between a transverse jet momentum of 200 to 400 GeV and 1400 to 1600 GeV, respectively.

With this improved track reconstruction performance, and vastly smaller uncertainties through the data-driven measurement of the track reconstruction inefficiency, ways to reconstruct the masses of jets with higher precision become possible. Three different options exist to build the mass of the jet purely from calorimeter information, from tracks of charged particles associated to the jet, or by combining all available information into a combined jet mass. A simulation based calibration procedure for the jet mass scale is inevitable, and it is demonstrated that such a technique can provide closure. Combining the strengths of both the calorimeter and tracker into the combined mass provides the most performant reconstructed jet mass currently available, reducing both the resolution of the reconstructed mass of the jet and its uncertainty.

Employing these novel reconstruction methods, a search for resonances with masses in the range $1.2 < m < 3.5$ TeV in the hadronically decaying WZ , WW , or ZZ final state, is performed in 15.5 fb^{-1} of $\sqrt{s} = 13$ TeV proton-proton collision data. No significant deviations from the background expectations are observed. An additional charged or neutral heavy vector boson, as predicted by the Heavy Vector Triplet phenomenological Lagrangian (assuming $g_V = 1$), decaying through $W' \rightarrow WZ$ (or $Z' \rightarrow WW$), is excluded in the mass range 1.2–2.0 (1.2–1.7) TeV at the 95% confidence level.

BIBLIOGRAPHY

- [1] A. Einstein. Die Grundlage der allgemeinen Relativitätstheorie. *Ann. Phys.*, 354:769–822, 1916.
- [2] C. Patrignani and Particle Data Group. Review of particle physics. *Chin. Phys. C*, 40(10):100001, 2016.
- [3] M. Gell-Mann. A schematic model of baryons and mesons. *Phys. Lett.*, 8:214–215, 1964.
- [4] S. L. Glashow. Partial symmetries of weak interactions. *Nucl. Phys.*, 22:579–588, 1961.
- [5] S. Weinberg. A model of leptons. *Phys. Rev. Lett.*, 19:1264–1266, 1967.
- [6] A. Salam. Gauge unification of fundamental forces. *Rev. Mod. Phys.*, 52:525–538, Jul 1980.
- [7] F. Englert and R. Brout. Broken symmetry and the mass of gauge vector mesons. *Phys. Rev. Lett.*, 13:321–323, 1964.
- [8] P. W. Higgs. Broken symmetries and the masses of gauge bosons. *Phys. Rev. Lett.*, 13:508–509, 1964.
- [9] UA1 Collaboration. Experimental observation of isolated large transverse energy electrons with associated missing energy at $\sqrt{s} = 540$ GeV. *Phys. Lett.*, B122:103–116, 1983.
- [10] UA1 Collaboration. Experimental observation of lepton pairs of invariant mass around $95 \text{ GeV}/c^2$ at the CERN SPS collider. *Phys. Lett.*, B126:398–410, 1983.
- [11] ATLAS Collaboration. Observation of a new particle in the search for the Standard Model Higgs boson with the ATLAS detector at the LHC. *Phys. Lett. B*, 716:1–29, 2012.
- [12] CMS Collaboration. Observation of a new boson at a mass of 125 GeV with the CMS experiment at the LHC. *Phys. Lett. B*, 716:30–61, 2012.
- [13] ATLAS Collaboration. The ATLAS experiment at the CERN Large Hadron Collider. *JINST*, 3(08):S08003, 2008.
- [14] L. Evans and P. Bryant. LHC machine. *JINST*, 3(08):S08001, 2008.
- [15] K. Sliwa. ATLAS overview and main results. In *Proceedings, International School on High Energy Physics : Workshop on High Energy Physics in the near Future. (LISHEP 2013): Rio de Janeiro, Brazil, March 17-24, 2013*, 2013.
- [16] ATLAS Collaboration. *ATLAS Inner Detector: Technical Design Report*. 1997.

- [17] ATLAS Collaboration. ATLAS pixel detector electronics and sensors. *JINST*, 3(07):P07007, 2008.
- [18] R. W. L. Jones and D. Barberis. The evolution of the ATLAS computing model. *J. Phys. Conf. Ser.*, 219(7):072037, 2010.
- [19] ATLAS Collaboration. *ATLAS computing: Technical Design Report*. 2005.
- [20] ATLAS Collaboration. Performance of the ATLAS silicon pattern recognition algorithm in data and simulation at $\sqrt{s} = 7$ TeV. (ATLAS-CONF-2010-072), 2010.
- [21] RA. Rosenfeld and J. Faltz. Sequential operations in digital picture processing. *J. ACM*, 13(4):471–494, 1966.
- [22] R. Frühwirth. Application of Kalman filtering to track and vertex fitting. *Nucl. Instrum. Meth.*, A262:444–450, 1987.
- [23] ATLAS Collaboration. Muon reconstruction performance of the ATLAS detector in proton–proton collision data at $\sqrt{s} = 13$ TeV. *Eur. Phys. J.*, C76(5):292, 2016.
- [24] D. Wicke. A new algorithm for solving tracking ambiguities. (LC-TOOL-1999-007-TESLA):219–228, 1999.
- [25] ATLAS Collaboration. A neural network clustering algorithm for the ATLAS silicon pixel detector. *JINST*, 9:P09009, 2014.
- [26] R. Jansky. Truth seeded reconstruction for fast simulation in the ATLAS experiment. (CERN-THESIS-2013-194), 2013.
- [27] ATLAS Collaboration. The optimization of ATLAS track reconstruction in dense environments. (ATL-PHYS-PUB-2015-006), 2015.
- [28] T. Sjostrand, S. Ask, J. R. Christiansen, R. Corke, N. Desai, et al. An introduction to PYTHIA 8.2. 2014.
- [29] ATLAS Collaboration. Summary of ATLAS Pythia 8 tunes. (ATL-PHYS-PUB-2012-003), 2012.
- [30] A.D. Martin, W.J. Stirling, R.S. Thorne, and G. Watt. Parton distributions for the LHC. *Eur.Phys.J.*, C63:189–285, 2009.
- [31] ATLAS Collaboration. Topological cell clustering in the ATLAS calorimeters and its performance in LHC Run 1. (CERN-PH-EP-2015-304), 2016.
- [32] M. Cacciari, G. P. Salam, and G. Soyez. The anti- k_T jet clustering algorithm. *JHEP*, 04:063, 2008.
- [33] J. M. Butterworth, A. R. Davison, M. Rubin, and G. P. Salam. Jet substructure as a new higgs-search channel at the large hadron collider. *Phys. Rev. Lett.*, 100:242001, Jun 2008.
- [34] M. Cacciari, G. P. Salam, and G. Soyez. Fastjet user manual. *Eur. Phys. J.*, C72:1896, 2012.

- [35] ATLAS Collaboration. Jet energy measurement and its systematic uncertainty in proton-proton collisions at $\sqrt{s} = 7$ TeV with the ATLAS detector. *Eur. Phys. J.*, C75:17, 2015.
- [36] D. Krohn, J. Thaler, and LT Wang. Jet Trimming. *JHEP*, 1002:084, 2010.
- [37] ATLAS. Jet energy measurement with the ATLAS detector in proton-proton collisions at $\sqrt{s} = 7$ TeV. *Eur. Phys. J. C*, 73:2304, 2013.
- [38] ATLAS Collaboration. Performance of jet substructure techniques for large- R jets in proton-proton collisions at $\sqrt{s} = 7$ TeV using the ATLAS detector. *JHEP*, 1309:076, 2013.
- [39] M. Cacciari and G. P. Salam. Pileup subtraction using jet areas. *Phys. Lett.*, B659:119–126, 2008.
- [40] ATLAS Collaboration. Calibration of b -tagging using dileptonic top pair events in a combinatorial likelihood approach with the ATLAS experiment. (ATLAS-CONF-2014-004), 2014.
- [41] ATLAS Collaboration. Commissioning of the ATLAS high-performance b -tagging algorithms in the 7 TeV collision data. (ATLAS-CONF-2011-102), 2011.
- [42] G. Apollinari, I. Bejar Alonso, O. Brüning, M. Lamont, and L. Rossi. *High-Luminosity Large Hadron Collider (HL-LHC): Preliminary Design Report*. 2015.
- [43] ATLAS Collaboration. ATLAS Phase-II Upgrade Scoping Document. *CERN-LHCC-2015-020. LHCC-G-166*, 2015.
- [44] ATLAS Collaboration. Expected Performance of the ATLAS Inner Tracker at the High-Luminosity LHC. (ATL-PHYS-PUB-2016-025), 2016.
- [45] R. D. Ball et al. Parton distributions for the LHC Run II. *JHEP*, 1504:040, 2015.
- [46] GEANT4 Collaboration. GEANT4—A Simulation toolkit. *Nucl.Instrum.Meth.*, A506:250–303, 2003.
- [47] ATLAS Collaboration. Measurement of performance of the pixel neural network clustering algorithm of the ATLAS experiment at $\sqrt{s} = 13$ TeV. (ATL-PHYS-PUB-2015-044), 2015.
- [48] ATLAS Collaboration. ATLAS jet energy scale uncertainties using tracks in proton proton collisions at $\sqrt{s} = 7$ TeV. (ATLAS-CONF-2011-067), 2011.
- [49] T. Gleisberg, S. Höche, F. Krauss, M. Schönherr, S. Schumann, et al. Event generation with SHERPA 1.1. *JHEP*, 0902:007, 2009.
- [50] M. Bahr et al. Herwig++ physics and manual. *Eur. Phys. J.*, C58:639–707, 2008.
- [51] ATLAS Collaboration. Jet mass reconstruction with the ATLAS detector in early Run 2 data. (ATLAS-CONF-2016-035), 2016.
- [52] CMS Collaboration. Particle-Flow Event Reconstruction in CMS and Performance for Jets, Taus, and MET. (CMS-PAS-PFT-09-001), 2009.

- [53] M. Son, C. Spethmann, and B. Tweedie. Diboson-jets and the search for resonant Zh production. *JHEP*, 08:160, 2012.
- [54] A. Katz, M. Son, and B. Tweedie. Jet substructure and the search for neutral spin-one resonances in electroweak boson channels. *JHEP*, 03:011, 2011.
- [55] S. Schaetzel and M. Spannowsky. Tagging highly boosted top quarks. *Phys. Rev.*, D89(1):014007, 2014.
- [56] A. J. Larkoski, F. Maltoni, and M. Selvaggi. Tracking down hyper-boosted top quarks. *JHEP*, 06:032, 2015.
- [57] S. Bressler, T. Flacke, Y. Kats, S. J. Lee, and G. Perez. Hadronic calorimeter shower size: Challenges and opportunities for jet substructure in the super-boosted regime. *Phys. Lett.*, B756:137–141, 2016.
- [58] ATLAS Collaboration. A study of the material in the ATLAS inner detector using secondary hadronic interactions. *JINST*, 7:P01013, 2012.
- [59] ATLAS Collaboration. Early inner detector tracking performance in the 2015 data at $\sqrt{s} = 13$ TeV. (ATL-PHYS-PUB-2015-051), 2015.
- [60] ATLAS Collaboration. Alignment of the ATLAS inner detector and its performance in 2012. (ATLAS-CONF-2014-047), 2014.
- [61] G. Altarelli, B. Mele, and M. Ruiz-Altaba. Searching for new heavy vector bosons in $p\bar{p}$ colliders. *Z. Phys. C*, 45:109, 1989.
- [62] E. Eichten, I. Hinchliffe, K. D. Lane, and C. Quigg. Super collider physics. *Rev. Mod. Phys.*, 56:579–707, 1984.
- [63] C. Quigg. Gauge theories of the strong, weak, and electromagnetic interactions. *Princeton University Press*, page 227, 2013.
- [64] J. C. Pati and A. Salam. Lepton Number as the Fourth Color. *Phys. Rev. D*, 10:275–289, 1974. [Erratum: *Phys. Rev. D* 11,703(1975)].
- [65] H. Georgi and S. L. Glashow. Unity of all elementary particle forces. *Phys. Rev. Lett.*, 32:438–441, 1974.
- [66] H. Georgi. The state of the art - gauge theories. *AIP Conf. Proc.*, 23:575–582, 1975.
- [67] H. Fritzsch and P. Minkowski. Unified interactions of leptons and hadrons. *Annals Phys.*, 93:193–266, 1975.
- [68] L. Randall and R. Sundrum. A Large mass hierarchy from a small extra dimension. *Phys. Rev. Lett.*, 83:3370–3373, 1999.
- [69] T. Han, J. D. Lykken, and R.J. Zhang. On Kaluza-Klein states from large extra dimensions. *Phys. Rev. D*, 59:105006, 1999.
- [70] K. Agashe, H. Davoudiasl, G. Perez, and A. Soni. Warped gravitons at the LHC and beyond. *Phys. Rev. D*, 76:036006, 2007.

- [71] O. Antipin, D. Atwood, and A. Soni. Search for RS gravitons via $W_L W_L$ decays. *Phys. Lett. B*, 666:155–161, 2008.
- [72] O. Antipin and A. Soni. Towards establishing the spin of warped gravitons. *JHEP*, 0810:018, 2008.
- [73] G. C. Branco, P. M. Ferreira, L. Lavoura, M. N. Rebelo, M. Sher, and J. P. Silva. Theory and phenomenology of two-Higgs-doublet models. *Phys. Rept.*, 516:1–102, 2012.
- [74] M. Perelstein. Little higgs models and their phenomenology. *Prog. Part. Nucl. Phys.*, 58(1):247 – 291, 2007.
- [75] F. Sannino. Technicolor and beyond: Unification in theory space. *J. Phys. Conf. Ser.*, 259(1):012003, 2010.
- [76] E. Eichten and K. Lane. Low-scale technicolor at the Tevatron and LHC. *Phys. Lett. B*, 669:235–238, 2008.
- [77] S. Catterall, L. Del Debbio, J. Giedt, and L. Keegan. MCRG minimal walking technicolor. *Phys. Rev. D*, 85:094501, 2012.
- [78] J.R. Andersen, O. Antipin, G. Azuelos, L. Del Debbio, E. Del Nobile, et al. Discovering technicolor. *Eur. Phys. J. Plus*, 126:81, 2011.
- [79] D. Barducci, A. Belyaev, S. Moretti, S. De Curtis, and G. M. Pruna. LHC physics of extra gauge bosons in the 4D Composite Higgs Model. *EPJ Web Conf.*, 60:20049, 2013.
- [80] D. Pappadopulo, A. Thamm, R. Torre, and A. Wulzer. Heavy vector triplets: bridging theory and data. *JHEP*, 2014(9), 2014.
- [81] ATLAS Collaboration. Search for high-mass diboson resonances with boson-tagged jets in proton-proton collisions at $\sqrt{s} = 8$ TeV with the ATLAS detector. (CERN-PH-EP-2015-115), 2015.
- [82] CMS Collaboration. Search for massive resonances in dijet systems containing jets tagged as W or Z boson decays in pp collisions at $\sqrt{s} = 8$ TeV. *JHEP*, 1408:173, 2014.
- [83] CMS Collaboration. Search for massive resonances decaying into pairs of boosted bosons in semi-leptonic final states at $\sqrt{s} = 8$ TeV. *JHEP*, 1408:174, 2014.
- [84] ATLAS Collaboration. Search for resonant diboson production in the $\ell' \ell' q \bar{q}$ final state in pp collisions at $\sqrt{s} = 8$ TeV with the ATLAS detector. *Eur. Phys. J. C*, 75:69–90, 2015.
- [85] ATLAS Collaboration. Search for production of WW/WZ resonances decaying to a lepton, neutrino and jets in pp collisions at $\sqrt{s} = 8$ TeV with the ATLAS detector. *Eur. Phys. J.*, C75(5):209, 2015. [Erratum: *Eur. Phys. J.*C75,370(2015)].
- [86] ATLAS Collaboration. Searches for heavy diboson resonances in pp collisions at $\sqrt{s} = 13$ TeV with the ATLAS detector. *JHEP*, 09:173, 2016.

- [87] CMS Collaboration. Search for massive resonances decaying into pairs of boosted bosons in semi-leptonic final states at $\sqrt{s} = 8$ TeV. *JHEP*, 08:174, 2014.
- [88] ATLAS Collaboration. Search for resonances with boson-tagged jets in 15.5 fb^{-1} of pp collisions at $\sqrt{s} = 13$ TeV collected with the ATLAS detector. (ATLAS-CONF-2016-055), 2016.
- [89] ATLAS Collaboration. Improved luminosity determination in pp collisions at $\sqrt{s} = 7$ TeV using the ATLAS detector at the LHC. *Eur. Phys. J. C*, 73(8):2518, 2013.
- [90] J. Alwall, R. Frederix, S. Frixione, V. Hirschi, F. Maltoni, O. Mattelaer, H. S. Shao, T. Stelzer, P. Torrielli, and M. Zaro. The automated computation of tree-level and next-to-leading order differential cross sections, and their matching to parton shower simulations. *JHEP*, 07:079, 2014.
- [91] L. Randall and R. Sundrum. An alternative to compactification. *Phys. Rev. Lett.*, 83:4690–4693, 1999.
- [92] ATLAS Collaboration. Electron efficiency measurements with the ATLAS detector using the 2012 LHC proton-proton collision data. (ATLAS-CONF-2014-032), 2014.
- [93] ATLAS Collaboration. Selection of jets produced in 13 TeV proton-proton collisions with the ATLAS detector. (ATLAS-CONF-2015-029), 2015.
- [94] ATLAS Collaboration. Identification of boosted, hadronically-decaying W and Z bosons in $\sqrt{s} = 13$ TeV Monte Carlo Simulations for ATLAS. (ATL-PHYS-PUB-2015-033), 2015.
- [95] B.R. Webber. Average multiplicities in jets. *Phys.Lett.*, B143:501, 1984.
- [96] G. Choudalakis and D. Casadei. Plotting the differences between data and expectation. *Eur. Phys. J. Plus*, 127(2):25, 2012.
- [97] ATLAS Collaboration. Luminosity determination in pp collisions at $\sqrt{s} = 7$ TeV using the ATLAS detector at the LHC. *Eur. Phys. J.*, C71:1630, 2011.
- [98] G. Cowan, K. Cranmer, E. Gross, and O. Vitells. Asymptotic formulae for likelihood-based tests of new physics. *Eur.Phys.J.C*, 71:1554, 2011.

EIDESSTATTLICHE ERKLÄRUNG

Ich erkläre hiermit an Eides statt durch meine eigenhändige Unterschrift, dass ich die vorliegende Arbeit selbständig verfasst und keine anderen als die angegebenen Quellen und Hilfsmittel verwendet habe. Alle Stellen, die wörtlich oder inhaltlich den angegebenen Quellen entnommen wurden, sind als solche kenntlich gemacht.

Die vorliegende Arbeit wurde bisher in gleicher oder ähnlicher Form noch nicht als Magister-/Master-/Diplomarbeit/Dissertation eingereicht.

Innsbruck, November 2016

Roland Jansky